Scuola di Dottorato in Ingegneria Civile e Architettura

Dottorato in Ingegneria Strutturale e Geotecnica

A computational approach based on high-performance beam finite element for predictive response in monitoring existing bridges

Daniela Fusco

XXXVI Ciclo - A.A. 2023/2024

Dipartimento di Ingegneria Strutturale e Geotecnica

SAPIENZA
UNIVERSITÀ DI ROMA

SAPIENZA
UNIVERSITÀ DI ROMA

Faculty of Civil and Industrial Engineering

Department of Structural and Geotechnical Engineering

PhD Thesis in Structural Engineering

A computational approach based on high-performance beam finite element for predictive response in monitoring existing bridges

PhD Candidate:

Daniela Fusco

Advisor:

Prof. Daniela Addessi

Co-Advisor:

Prof. Vicenzo Gattulli

Rome, February 2024

Abstract

In recent years, the structural safety of existing bridges has become an increasingly relevant topic due to the age and extent of the Italian infrastructure assets. Several technologies, such as the application of machine learning techniques, have been developed to automate inspections and monitoring processes of existing bridges. One promising approach is the use of simulated data from numerical models to train data-driven algorithms for detecting structural damage. To improve the effectiveness of the algorithm training, it is necessary to create an extensive dataset including various damage scenarios. This procedure entails performing numerous nonlinear analyses, thereby highlighting the importance of adopting an efficient numerical model to reduce the computational effort.

This work proposes a high-performance computational approach to predict the nonlinear response of reinforced concrete and prestressed concrete bridges. Specifically, this work adopts an advanced fiber beam element based on a damage-plasticity model, which offers superior computational efficiency, compared to 2D and 3D finite element models. The proposed damage-plastic model introduces two different damage variables for tensile and compressive behaviour to consider the re-closure of tensile cracks when moving from tension to compression states. To accurately assess the frequency variation due to the cracking of structural components, this research proposes a modification of the damage-plastic model which accounts for the partial closure of cracks. Both constitutive models are implemented in *OpenSees* software framework. Computational aspects and solution algorithms are extensively detailed in this thesis.

Several applications are presented in this work to demonstrate the effectiveness of the proposed computational approach in simulating the nonlinear static and dynamic responses of concrete bridge structures. The advanced fiber beam element is validated by comparing numerical results with experimental measurements from tests conducted on reinforced concrete and prestressed concrete beams. Additionally, an application at the structural level of the proposed numerical method is discussed simulating a full-scale test of an existing prestressed reinforced concrete bridge.

The application of the model within the new promising developments in Structural Health Monitoring (SHM) is explored. Especially, this research proposes an approach for training Artificial Neural Networks (ANNs) to detect structural damage using simulated data derived from numerical results. An unsupervised method has

been employed to train a neural network. The prediction error of such network model is investigated as a suitable measure for the definition of a damage indicator. Finally, regarding the new advancements in vision-based techniques, this thesis also explores the integration of the proposed fiber beam element into the process of creating synthetic environment, that is virtual dataset generated to train algorithms of visual recognition systems. In conclusion, the integration of the advanced fiber beam model with an accurate constitutive law and machine-learning techniques shows promising potential for future innovations in the monitoring of existing bridges.

Acknowledgements

Vorrei esprimere la mia più sincera gratitudine alla Prof.ssa Daniela Addessi, la cui guida e supporto sono stati fondamentali per il mio percorso di ricerca. La sua profonda conoscenza della materia e la capacità di stimolare il pensiero critico hanno arricchito notevolmente la mia esperienza accademica. Le sono profondamente grata per il suo incoraggiamento costante e per aver creduto sempre nelle mie capacità.

Ringrazio sinceramente il Prof. Vincenzo Gattulli per il suo prezioso supporto e orientamento nel corso della mia ricerca. La sua competenza e il suo impegno per l'innovazione hanno costantemente ispirato il mio lavoro, incentivandomi ad affrontare nuove sfide scientifiche. Inoltre, un ringraziamento speciale a Cecilia Rinaldi per i suoi preziosi consigli e per l'attenzione dedicata al mio lavoro. La sua esperienza e sostegno sono stati indispensabili nel guidarmi attraverso questo percorso.

Infine, voglio esprimere la mia più profonda e sentita gratitudine nei confronti dei miei genitori, della famiglia e dei miei più cari amici. Sono stati il mio punto di riferimento costante, dandomi sempre un supporto incondizionato e un incoraggiamento incessante. Li ringrazio dal profondo del cuore di aver sempre creduto in me e di avermi dato la forza per affrontare i momenti più difficili. Questo traguardo non sarebbe stato possibile senza il loro amore.

Contents

List of Figures

List of Tables

1 Introduction

1.1 Motivations

The structural safety of existing infrastructures has become increasingly relevant topic in the public debate in recent years. Due to the age and extent of the infrastructure assets, as well as the significant costs associated with maintaining and repairing them, there is an urgent need to develop more effective and reliable monitoring and safety evaluation methods. For example, in the United States there are more than 617,000 bridges and a recent publication estimates that 42% of them are over 50 years old, with approximately 7.5% of them exhibiting structural deficiencies. From an economic perspective, the US backlog for bridge repairs is estimated at $125 billion [1]. This scenario could be qualitatively extended to Italy, considering that most bridges were constructed post-World War II and are nearing the end of their service life. Moreover, Italy has a denser bridge network, with the number of bridges per square kilometre approximately six times greater than in the United States [2], [3]. Given these considerations, the structural health of bridges is essential not only for safety but also for its significant social and economic implications. In this context, the maintenance and monitoring of bridges emerge as effective solutions for preserving structural integrity of infrastructure and reducing the risk of collapse and the economic losses.

Responding to this need, in recent years the scientific community has increasingly focused on developing and refining reliable methods for Structural Health Monitoring (SHM). Especially, this field aims to develop systems and methodologies for monitoring the health status of structures in real-time. By continuously or periodically assessing the structural condition, an effective SHM system can detect early signs of damage or deterioration and provide essential information for timely maintenance and repairs [4], [5], [6], [7]. Currently, the standard approach utilized to assess the structural conditions is the visual inspection, however, it tends to be time-consuming and susceptible to human error. To overcome these limitations, several new approaches and techniques have been developed to detect, locate, and quantify damage, as well as to evaluate structural conditions of existing bridges. Especially, the increase of computational power and the development of advanced technologies have led to a growing interest in the automatization of the evaluation processes, driving scientific and technological innovations in this direction.

Recent advancements in Structural Health Monitoring (SHM) have emphasized the use of vibration-based techniques for their efficiency in detecting damage and evaluating the structural integrity of bridges [8], [9]. These techniques rely on assessing variations of structural dynamic characteristics, derived from in-situ vibration measurements, that indicate potential damage or structural weaknesses. Especially, the damage of structural components causes the modification of vibration modal parameters, such as natural frequencies, mode shapes and modal damping. In literature, various vibration-based methods have been proposed, including techniques based on natural frequency variations, methods that utilize mode shapes, curvature mode shapes, and approaches that combine both mode shapes and frequencies [8], [10]. Furthermore, damage-sensitive features can be extracted from both time series analysis [11] and dynamic response in the frequency domain [12]. Vibration-based techniques are usually classified into model-based and data-driven methods; the former are based on structural identification and model updating procedures to calibrate physical models according to experimental measurements [13], while the data-driven methods are based on statistical models trained on past data [14]. The latter approach utilizes algorithms to identify patterns from the measured data, recognizing the presence of damage without the need for a detailed physical model of the structure. In this context, the researchers are currently exploring the application of Artificial Intelligence (AI) for more accurate and automatized damage detection and identification. Particularly, the application of machine learning techniques has become increasingly popular, with Artificial Neural Networks (ANNs) being particularly prevalent for their ability to efficiently identify and assess changes in structural systems [15]. The ANNs are extensively applied in several studies in literature [16], [17], [18], [19]. In particular, the adoption of Nonlinear AutoRegressive (NAR) networks is particularly effective for multi-step ahead prediction, providing more accurate results than other types of neural networks [20]. The model-based approach provides a physical representation of the behaviour of structures, enabling predictive analyses and more accurate assessments of structural health, particularly effective with degradation models integrated into FEM models. However, a drawback is its limited applicability for real-time monitoring due to the significant computational effort required for the model updating process. Conversely, the data-driven approach excels in detecting changes which indicate structural damage, but it lacks in providing a physical interpretation of the structural variations and in predicting structural behaviour. To enhance the reliability of machine learning algorithms, recent advancements include the use of FEM models to generate

simulated data with different damage scenarios. This data is then used to train artificial neural networks, improving their accuracy and predictive capabilities.

Another area of research in SHM focuses on automated visual inspection, adopting one of the most advanced technologies: the Unmanned Aerial Vehicles (UAVs). Specifically, several research aims to integrate in UAVs autonomous capabilities for detecting and quantifying structural damages [21], [22], [23], [24], [25]. To develop a fully automated vision-based assessment process, it is necessary to train the visual recognition algorithms, but the availability of a training dataset of real images with various types of bridges and damage scenarios is limited. A new and promising approach to expand training datasets involves the use of synthetic environments including several simulated damage scenarios. Therefore, also for new advancements in vision-based approach, the adoption of a mechanical model into the training procedure is essential to improve the accuracy of machine learning algorithms.

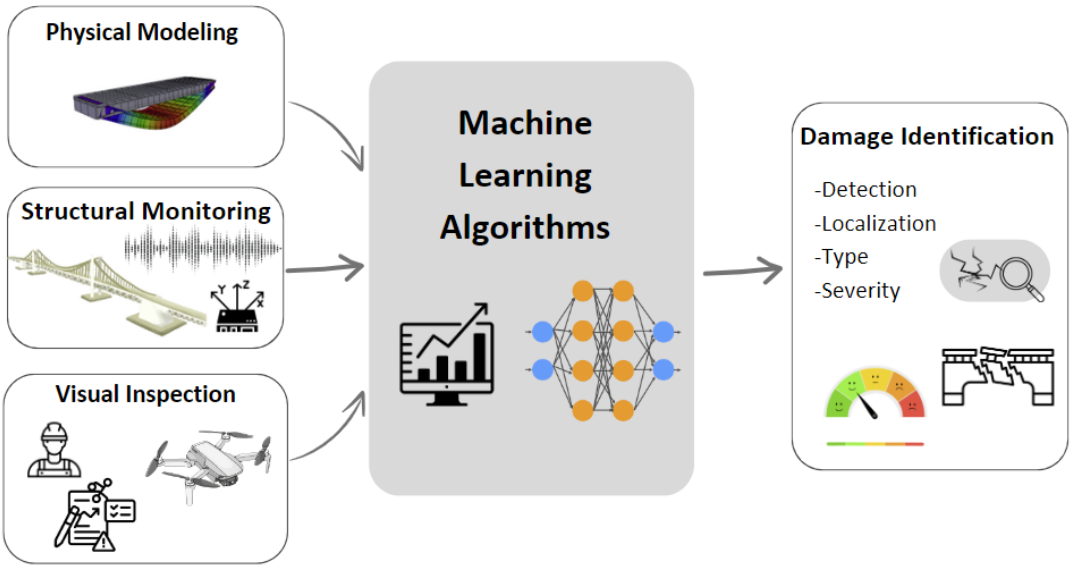

Figure 1: A new holistic approach in SHM to comprise physical modelling, structural monitoring, and information from visual inspections.

Upon consideration of the discussed topics, contrary to the initial perception that new technologies are diverging from conventional assessment methodologies based on structural mechanics, it becomes evident that the academic community is gaining a new understanding. Specifically, to enhance the reliability of machine learning algorithms, it is essential to integrate their training with numerical models capable of simulating the mechanics of the structural problem. In this regard, Figueiredo

[14] discusses a possible future advancement in SHM based on the adoption of a holistic approach, as shown in Figure 1. This approach should integrate the data derived from physical models, structural monitoring and from visual inspections, improving the learning process of AI algorithms to detect structural damages.

Training machine learning-based algorithms require the generation of a wide range of simulated data for different damage scenarios. The simulated dataset derives from the numerical results obtained through several static and/or dynamic nonlinear analyses, which demand a significant computational effort. For this reason, it is crucial adopting a FEM model that is computationally efficient as illustrated in Figure 2. Additionally, it is necessary that the FEM model accurately simulates the material nonlinearity, such as damage and degradation, to predict the structural behaviour under different damage scenarios.

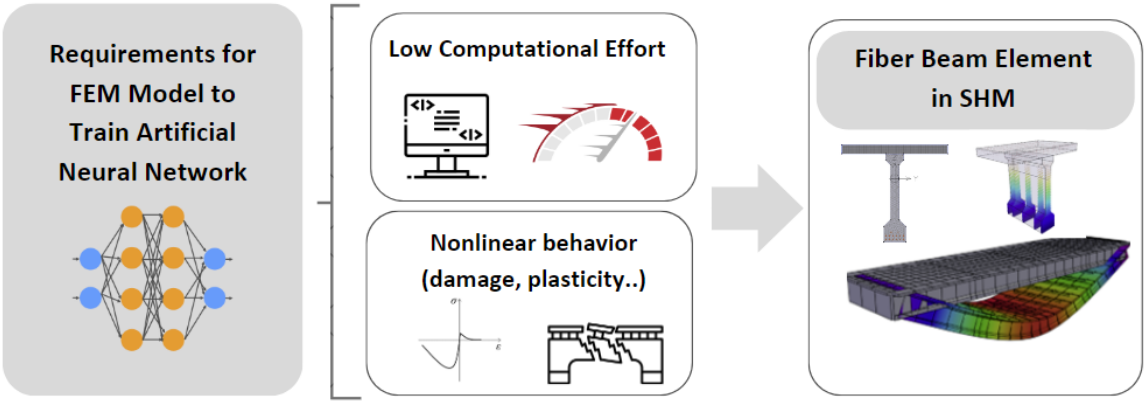

Figure 2: Requirements for FEM model to train ANNs.

Several modelling approaches have been developed to analyse the behaviour of real structures and a crucial decision involves selecting the appropriate numerical method. In common practice, it is often necessary to choose whether to use more complex models like 2D or 3D elements that can accurately represent nonlinear material behaviour but are computationally expensive; or simpler models such as beam elements, where the behaviour is generally assumed to be linear elastic. The adoption of elastic beam elements is effective in identifying damage, which is modelled through stiffness reduction of the damaged zone. However, this method is not suitable for the prediction of future structural performance [26]. In this regard, fiber beam finite elements provide a good compromise by allowing for the modelling of nonlinear material constitutive law while significantly reducing the number of elements and thus the computational effort, compared to models using 2D or 3D

elements. Although fiber beam finite elements have been widely applied in the field of seismic engineering, there are few applications in modelling bridge decks within the context of structural health monitoring.

Different formulations for fiber beam element models have been proposed in literature. The displacement-based (DB) formulation is the most adopted in commercial software. This approach assumes compatible displacement and strain fields along the element and the equilibrium is satisfied in a weak form [27]. The force-based (FB) formulation, which strictly satisfies the equilibrium, is more suitable for describing beam elements in case of material nonlinearity [28], [29]. Specifically, the FB formulation is more computationally efficient compared to the DB approach because it requires fewer elements to accurately represent nonlinear behaviour. Several constitutive laws have been developed for both concrete and steel. Specifically, for concrete, one of the most advanced models is the damage-plastic models which describe the macroscopic effect of the micromechanical process through homogenized parameters [30], [31]. Damage is related to the propagation of microcracks through the material, while plasticity is due to the intergranular displacements. The formulation proposed in [32], [33] also considers two different damage parameters in tension and compression to account for the unilateral effect of the re-closure of cracks. While these models have already been extensively adopted to model the nonlinear behaviour of concrete in several applications, further investigation is needed to verify their applicability in the field of structural monitoring. One of the most widely used FEM software in the academic community is *OpenSees*, which is an open-source software framework. Currently, the described damage-plastic constitutive model is not available in *OpenSees*. Regarding the frequency variation due to structural damage in the case of static loading and unloading cycles, the dynamic response is significantly influenced by several mechanical phenomena such as concrete tensile damage and the partial closure of cracks induced by the presence of concrete aggregate [34], [35], [36]. While this phenomenon can be neglected in nonlinear static applications, it becomes crucial for accurately assessing the frequency of a cracked beam in the unloading phase. Therefore, integrating this phenomenon into the damage-plastic model is necessary to accurately capture frequency variations in vibration-based monitoring.

1.2 Research objectives

The objective of this research is to propose a more efficient structural modelling approach that can accurately represent the nonlinear behaviour of reinforced and prestressed concrete bridges in the field of Structural Health Monitoring. The main objectives can be summarized as follows:

- Propose a nonlinear modelling approach for Structural Health Monitoring (SHM) which adopts high-performance fiber beam elements.
- Implement in *OpenSees* a three-dimensional damage-plastic constitutive model to accurately represent the material nonlinearities of concrete.
- Propose an improved version of the classic damage-plastic model for concrete that accounts for the partial closure of cracks. This feature is crucial to accurately assess frequency variations due to damage of structural components.
- Demonstrate the reliability and potential of the proposed modelling approach in the field of SHM. This includes the validation of the model through applications at both the element level and the structural level, comparing numerical results with experimental data.
- Propose a procedure for training of Artificial Neural Networks (ANNs) using simulated data derived from numerical analyses.
- Develop a tool that allows the use of the fiber beam model for the generation of synthetic environments, which are adopted for the training of damage recognition algorithms in vision-based techniques.

These objectives are defined to improve the training of machine learning algorithms in the field of Structural Health Monitoring by providing a computationally efficient modelling approach for prestressed concrete and reinforced concrete bridges.

1.3 Organization of the thesis

The thesis is organized as follows:

- Chapter 2 presents a detailed overview of the proposed modelling approach, including a comparison of beam formulations and an introduction of the fiber beam elements. This chapter also describes the classical damage-plastic model and the modified version which accounts for the partial closure of cracks. The discussion extends to the localization issues and regularization techniques for fiber beam elements. Additionally, the chapter introduces some computational aspects and the solution algorithms. It concludes providing an overview of *OpenSees* software framework, where the constitutive models have been implemented in this research work.

- Chapter 3 discusses the methods for modelling of prestressed concrete beams in nonlinear analysis. It presents an application to compare the prestressed concrete fiber element model with the models available in MIDAS software. Finally, a validation of the model is illustrated comparing numerical and experimental results.

- Chapter 4 presents an overview of vibration-based methods in SHM and an introduction of dynamic analysis for fiber beam elements. It presents an application of the proposed modified damage-plastic model, comparing the numerical and experimental results.

- Chapter 5 introduces the machine learning technique applied for SHM and it proposes an approach for training a neural networks algorithm to detect structural damage using the proposed fiber beam element model. Finally, the chapter presents the training results of two numerical applications.

- Chapter 6 introduces the new technologies and advancements of artificial intelligence in vision-based techniques. Subsequently, it focuses on integrating the proposed beam model into the synthetic environment creation process, followed by a comparison of DB and FB approaches in practical application. The chapter concludes with a discussion of future developments in

integrating the mechanical model with synthetic environments for training algorithms of unmanned aerial vehicles.

- Chapter 7 presents an application at the structural level of the proposed numerical approach simulating the nonlinear response and variation of frequency of a full-scale test of an existing prestressed reinforced concrete bridge.

- Chapter 8 summarizes the main contributions and provides overall concluding remarks.

2 Finite Element Formulation

2.1 General

Several modelling methods and approaches have been developed to represent the nonlinear behaviour of structures. In common practice, both researchers and professional engineers often face the choice of adopting either more complex models like 2D or 3D finite elements, which can accurately represent the nonlinear behaviour of materials but are computationally demanding, or simpler models such as beam elements, where the behaviour is typically assumed elastic. In this regard, the fiber beam finite element provides a good compromise. Indeed, this element allows to model the nonlinear behaviour of materials with less computational effort compared to 2D and 3D elements. Fiber beam finite elements have been extensively used in the field of Seismic Engineering to model structural components, such as beams or piers, subjected to seismic loads. The objective of this study is to propose a modelling strategy that balances computational efficiency of the beam formulation with the accuracy of damage-plastic material model. This approach is developed to enhance the structural assessment and prediction of existing bridges, particularly within the realm of Structural Health Monitoring.

This chapter outlines the proposed modelling approach in detail. Specifically, Section 2.2 provides an overview of beam formulations, comparing the displacement-based and force-based approaches. The fiber beam element is presented in Section 2.3, while Section 2.4 describes the constitutive laws implemented in *OpenSees* software framework. This work adopts a damage-plastic model to represent the nonlinear behaviour of materials and proposes a modified version to consider the partial closure of cracks. In case of strain-softening behaviour, the localization of damage and/or strain within a confined area may occur, leading to the loss of objectivity of analysis. In Section 2.5, this numerical issue is described in detail, and several regularization techniques are discussed. Some computational aspects, including static condensation and solution algorithms, are described in detail in Section 2.6. Finally, Section 2.7 introduces the *OpenSees* software framework and the modelling strategy adopted in this research.

2.2 Beam Element Formulation

Several approaches have been proposed in literature for finite element beam models. The most common approach is the displacement-based (DB) formulation, or stiffness method, which assumes compatible displacement and strain fields along the element [27]. The equilibrium is satisfied in a weak form, leading to significant drawbacks, particularly in case of nonlinear analyses. Specifically, it requires a fine discretization in presence of nonlinear constitutive behaviour, which increases the computational effort of numerical analysis. To overcome the limitations of the DB approach, various methods have been proposed in literature. For instance, the Smart Displacement Based (SDB) beam element, introduced in [37], [38], utilizes adaptive displacement shape functions dependent on the diffusion of plastic deformations to enhance result accuracy. Additionally, an advanced version of DB element that strictly satisfies the axial equilibrium is proposed in [39] to accurately model the tension shift effects of reinforcement concrete columns and walls. In contrast to the DB formulation, the force-based (FB) exactly interpolates the stress fields along the element and the equilibrium is satisfied in a strong form. The FB approach is more suitable for describing beam elements in case of material nonlinearity, as extensively demonstrated in literature [28], [29], [40], [41], [42], [43], [44], [45]. Initially, this paragraph introduces the quantities that characterize the element formulation, followed by a brief description of the DB and FB approaches.

The element formulation discussed in this section is based on Timoshenko beam theory. However, it can be applied to the case of Euler-Bernoulli beams as in [30]. The assumptions of element formulation include small displacements and the hypothesis of rigid plane cross-sections. As illustrated in Figure 3, the local basic reference system comprises the *x*-axis, which is directed along the beam element axis, and the *y* and *z*-axes, which represent the principal axes of the cross-section. Eliminating the rigid body modes, the basic displacements of a beam element are expressed as follows:

$$\varepsilon^e = [u_j \quad \theta_{zi} \quad \theta_{zj} \quad \theta_{xj} \quad \theta_{yi} \quad \theta_{yj}]^T \tag{1}$$

where u_j is the translation along *x* of node *j*, while θ_{zi}, θ_{zj}, θ_{yi} and θ_{yj} are rotations of nodes *i* and *j* around the *z*- and *y*-axes. θ_{xj} is the rotation around *x*-axes of node *j*. Similarly, the vector of the element basic forces is defined as:

$$\boldsymbol{\sigma}^e = [N_j \quad M_{zi} \quad M_{zj} \quad M_{xj} \quad M_{yi} \quad M_{yj}]^T \tag{2}$$

being N_j, the axial force parallel to x-axes, and M_{zi} , M_{zj}, M_{yi} and M_{yj} the moments at nodes *i* and *j* around *z*- and *y*-axes. M_{xj} is the torsional moment around *x*-axes.

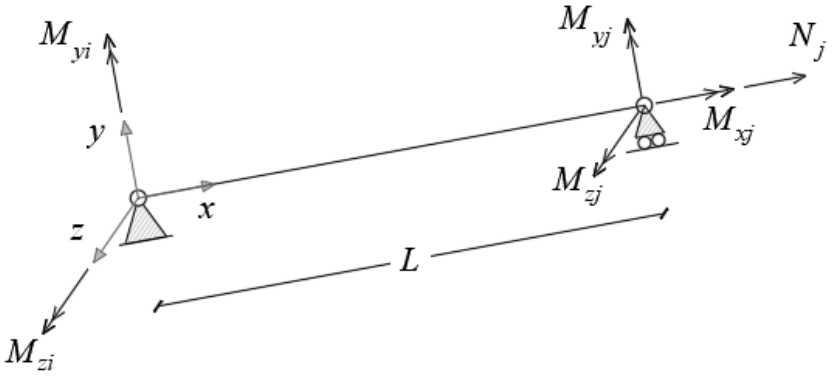

Figure 3: Local reference system and element basic forces.

Assuming rigid plane cross-sections, the generalized displacement vector at each section located at *x* is defined as:

$$\mathbf{u}_s(x) = [u(x) \quad \theta_z(x) \quad v(x) \quad \theta_x(x) \quad \theta_y(x) \quad w(x)]^T \tag{3}$$

where $u(x)$, $v(x)$ and $w(x)$ are the translation along the local axes; and the respective rotations are represented by $\theta_x(x)$, $\theta_y(x)$ and $\theta_z(x)$. The generalized section deformation vector $\boldsymbol{\varepsilon}_s(x)$ is equal to:

$$\boldsymbol{\varepsilon}_s(x) = [\varepsilon_G(x) \quad \chi_z(x) \quad \gamma_y(x) \quad \chi_x(x) \quad \chi_y(x) \quad \gamma_z(x)]^T \tag{4}$$

being $\varepsilon_G(x)$ the axial deformation, $\chi_y(x)$ and $\chi_z(x)$ the flexural curvatures and $\gamma_y(x)$, $\gamma_z(x)$ the shear deformations. Finally, the component $\chi_x(x)$ is the torsional curvature. The relation between the generalized section displacement vector and deformation vector is expressed as follows:

$$\boldsymbol{\varepsilon}_s(x) = \mathbf{D}(x)\ \mathbf{u}_s(x) \tag{5}$$

where $\mathbf{D}(x)$, in case of Timoshenko beam, is the compatibility operator defined as:

$$\mathbf{D}(x) = \begin{bmatrix} \partial\diamond/\partial x & 0 & 0 & 0 & 0 & 0 \\ 0 & \partial\diamond/\partial x & 0 & 0 & 0 & 0 \\ 0 & -1 & \partial\diamond/\partial x & 0 & 0 & 0 \\ 0 & 0 & 0 & \partial\diamond/\partial x & 0 & 0 \\ 0 & 0 & 0 & 0 & \partial\diamond/\partial x & 0 \\ 0 & 0 & 0 & 0 & 1 & \partial\diamond/\partial x \end{bmatrix} \tag{6}$$

The generalized section stresses measure the stress state at a specific section located at x. In particular, this results as:

$$\boldsymbol{\sigma}_s(x) = [N(x) \quad M_z(x) \quad T_y(x) \quad M_x(x) \quad M_y(x) \quad T_z(x)]^T \tag{7}$$

where $N(x)$ is the axial stress, $M_z(x)$ and $M_y(x)$ the bending moments, $M_x(x)$ the torsional moment and $T_y(x)$ and $T_z(x)$ the shear forces. The section constitutive law, which relates the generalized stress to the generalized deformation, is presented in its incremental form as:

$$\dot{\boldsymbol{\sigma}}_s(x) = \mathbf{k}_s(x)\dot{\boldsymbol{\varepsilon}}_s(x) \tag{8}$$

where $\mathbf{k}_s(x)$ is the tangent section stiffness matrix. The constitutive relation in its inverse form results as:

$$\dot{\boldsymbol{\varepsilon}}_s(x) = \mathbf{f}_s(x)\dot{\boldsymbol{\sigma}}_s(x) \tag{9}$$

where $\mathbf{f}_s(x) = \mathbf{k}_s{}^{-\mathbf{1}}(x)$. The displacement-based (DB) formulation assumes compatible displacement and strain fields. In particular, the displacements along the elements are approximated through the interpolation polynomials. The generalized section deformation vector is assumed equal to:

$$\boldsymbol{\varepsilon}_s(x) = \boldsymbol{\alpha}_s(x)\, \boldsymbol{\varepsilon}^e \tag{10}$$

being $\boldsymbol{\alpha}_s(x) = \mathbf{D}(x)\, \mathbf{N}(x)$, where $\mathbf{N}(x)$ is the interpolation functions matrix. Using the virtual work equivalence, the element stiffness matrix is derived as:

$$\mathbf{K}^e = \int_0^L \boldsymbol{\alpha}_s^T(x) \mathbf{k}_s(x) \boldsymbol{\alpha}_s(x)\, dx \tag{11}$$

In the DB approach, the equilibrium is satisfied in a weak form, as it is enforced through the virtual work equivalence. Instead, the compatibility relation is satisfied in strong form.

Differently from the DB approach, the force-based (FB) approach exactly interpolates the section stress fields along the element, as follows:

$$\boldsymbol{\sigma}_s(x) = \mathbf{b}_s(x) \boldsymbol{\sigma}^e \tag{12}$$

where $\mathbf{b}_s(x)$ is the equilibrium matrix, containing the force interpolation functions. In particular, it is defined as:

$$\mathbf{b}_s(x) = \begin{bmatrix} 1 & 0 & 0 & 0 & 0 & 0 \\ 0 & \dfrac{x}{L} - 1 & \dfrac{x}{L} & 0 & 0 & 0 \\ 0 & -\dfrac{1}{L} & -\dfrac{1}{L} & 0 & 0 & 0 \\ 0 & 0 & 0 & 1 & 0 & 0 \\ 0 & 0 & 0 & 0 & \dfrac{x}{L} - 1 & \dfrac{x}{L} \\ 0 & 0 & 0 & 0 & \dfrac{1}{L} & \dfrac{1}{L} \end{bmatrix} \tag{13}$$

The element flexibility matrix is obtained through the application of the virtual work equivalence, as follows:

$$\mathbf{F}^e = \int_0^L \mathbf{b}_s{}^T(x) \mathbf{f}_s(x) \mathbf{b}_s(x)\, dx \tag{14}$$

In the FB beam formulation, equilibrium is satisfied in a strong form, whereas compatibility is expressed in weak form:

$$\boldsymbol{\varepsilon}^e = \int_0^L \mathbf{b}_s(x)\boldsymbol{\varepsilon}_s(x)\,dx \tag{15}$$

As previously mentioned, the force-based (FB) formulation is more efficient in describing beam elements response in presence of material nonlinear constitutive behaviour. Indeed, for DB elements, the curvature distribution along the element length is not accurately represented in case of inelastic behaviour [44]. Several studies demonstrated that the FB beam element is computationally more efficient because it requires fewer meshes to accurately represent the nonlinear response of beams [29], [46], [47]. In Section 2.6, the solution algorithms for both the FB and DB approaches are presented.

Besides FB and DB approaches, other more complex formulations can be found in existing literature. Spacone et al. [42] proposed a two-field mixed formulation, which is based on the principle of the stationary of the Hellinger-Reissner functional. This method adopts independent interpolation functions to approximate the strain and force fields. A three-field formulation, based on the Hu–Washizu principle, is discussed in [48]. In this case, displacement, stress and strain fields are independently interpolated. Additional formulations and a comparison between DB, FB, and mixed approaches are presented in [44].

2.3 Fiber Section Discretization

Beam elements are characterized by a discrete number of Gauss points, which varies based on the adopted integration rule (for further details refer to Section 2.5). In the context of fiber beam element models, the cross-sections, located at corresponding integration points, are subdivided into fibers. The section stiffness and generalized section stress are evaluated by the integration of the fiber response, which is governed by the constitutive law of the materials. The subdivision in fibers allows for a more accurate representation of the stress and strain distribution across the section. Additionally, in case of reinforced concrete beams, it allows to adopt different nonlinear constitutive laws for concrete and steel.

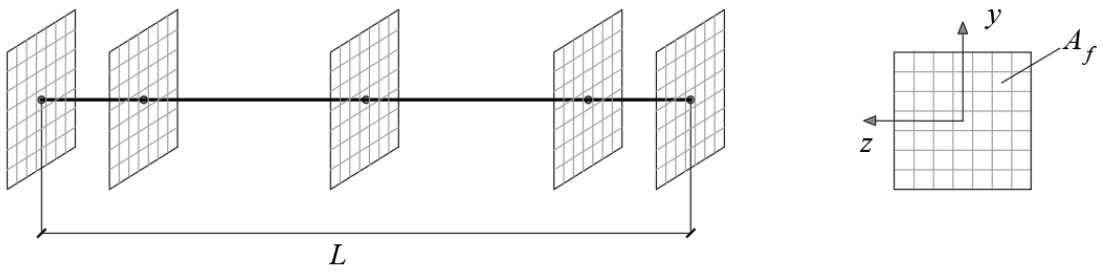

Figure 4: Fiber beam element - Section Discretization

Considering plane cross-sections, the fiber stress and strain vectors are defined as follows:

$$\begin{aligned} \boldsymbol{\varepsilon}_f(x,y,z) &= [\varepsilon_1(x,y,z), \gamma_{12}(x,y,z), \gamma_{13}(x,y,z)]^T, \\ \boldsymbol{\sigma}_f(x,y,z) &= [\sigma_1(x,y,z), \tau_{12}(x,y,z), \tau_{13}(x,y,z)]^T \end{aligned} \tag{16}$$

being ε_1 and σ_1 the axial strain and stress along x-axes; γ_{12}, γ_{13}, τ_{12} and τ_{13} are the shear strain and stress in x-y and x-z planes. The relation between fiber stress and strain vectors is given by the material constitutive law, which is expressed as:

$$\boldsymbol{\sigma}_f(x,y,z) = \mathbf{k}_f(x,y,z)\ \boldsymbol{\varepsilon}_f(x,y,z) \tag{17}$$

Further details on the constitutive law adopted for concrete and steel are provided in Section 2.4.

The fiber beam elements are based on the plane section hypothesis. Under this assumption, the fiber strain vector at point (*y*,*z*) of cross section is related to the generalized section deformation vector $\boldsymbol{\varepsilon}_s(x)$ through a geometric transformation matrix as follows:

$$\boldsymbol{\varepsilon}_f(x,y,z) = [\varepsilon_1(x,y,z), \gamma_{12}(x,y,z), \gamma_{13}(x,y,z)]^T = \mathbf{l}_s(y,z)\boldsymbol{\varepsilon}_s(x) \tag{18}$$

where $\mathbf{l}_s(y,z)$ is the following kinematic operator:

$$\mathbf{l}_s(y,z) = \begin{bmatrix} 1 & -y & 0 & 0 & z & 0 \\ 0 & 0 & 1 & -z & 0 & 0 \\ 0 & 0 & 0 & y & 0 & 1 \end{bmatrix} \tag{19}$$

By applying the virtual work equivalence, the generalized section stress vector and the tangent section stiffness matrix are obtained with the following equations:

$$\boldsymbol{\sigma}_s(x) = \int_{A_f} \mathbf{l}_s^T(y,z)\boldsymbol{\sigma}_f(x,y,z)dA_f \tag{20}$$

$$\mathbf{k}_s(x) = \int_{A_f} \mathbf{l}_s^T(y,z)\mathbf{k}_f(x,y,z)\mathbf{l}_s(y,z)dA_f \tag{21}$$

From a numerical point of view, previous integrals can be solved subdividing the cross-section into *n* fibers and adopting the midpoint integration rule [41]. With an increase of number of fibers, there is a corresponding improvement of the accuracy of integral calculations. However, this also leads to an increase of the computational effort. Further details about the influence of the number of cross-section integration points on the element response can be found in [45]. Additionally, more advanced models which integrate the effect of bond-slip into the fiber beam element are proposed in [49], [50]. Figure 5 shows the different levels of analysis from the global to the material level. To integrate a three-dimensional constitutive law in the fiber beam element, static condensation is necessary, which is discussed in Section 2.6.

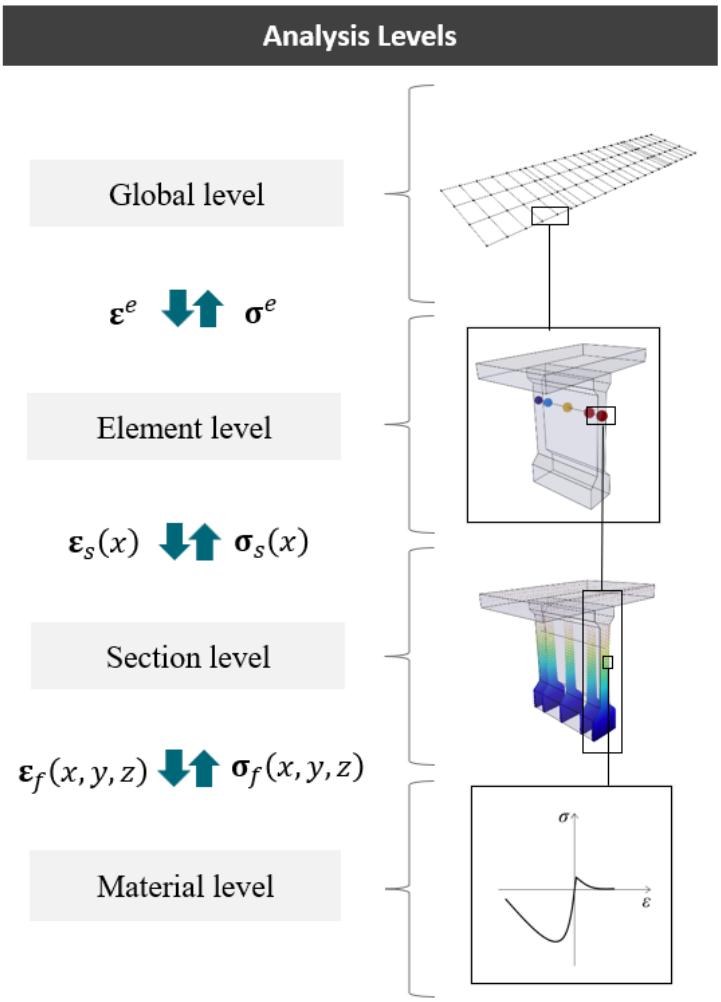

Figure 5: Scheme of the levels of analysis.

2.4 Material constitutive model

The following chapter introduces the constitutive laws utilized in this study to simulate the nonlinear behaviour of concrete and steel. The two materials behave differently at both the micro and macro mechanical levels. The main characteristics of each are briefly described in this section.

Steel is a ductile material characterized by a symmetric behaviour in tension and compression. When subjected to loading, steel behaves elastically until it reaches its yield point, where plastic deformation begins. After the yield point, the material usually exhibits a hardening behaviour in the nonlinear response. The unloading branch maintains the same slope as the initial elastic branch, and once the load is removed, the material deformation is equal to the residual plastic strain. The constitutive law can be effectively described by mechanical models based on plasticity. In Figure 6, a typical stress-strain curve of steel and an example of a steel specimen after the tensile failure are illustrated.

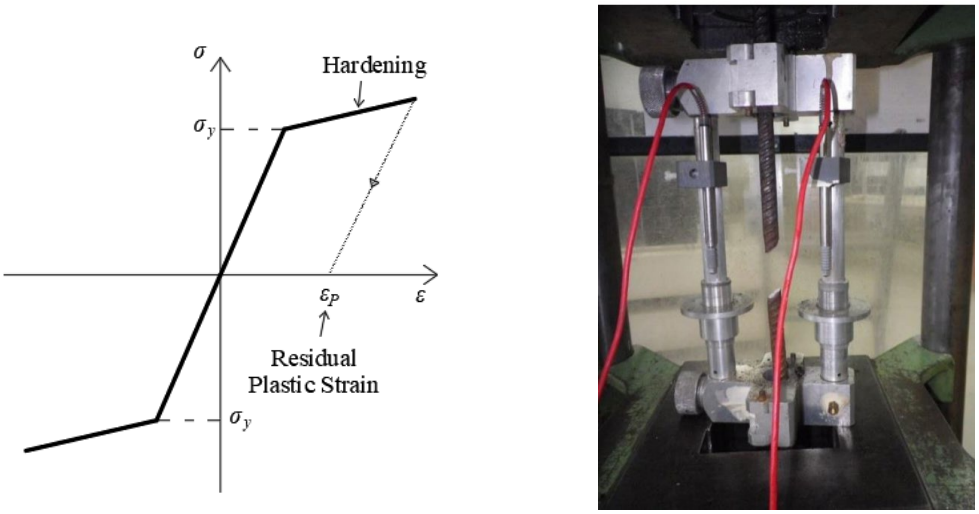

(a) *(b)*

Figure 6: Typical constitutive law of steel (a) and the tensile failure of a steel specimen [51]*(b)*

Differently from steel, concrete is a heterogeneous material with a non-symmetric behaviour in compression and tension. Figure 7 shows a simplified constitutive model for concrete and a typical compression failure. As the applied load increases, cracks develop and propagate through the material, resulting in a predominantly brittle mode of failure. After reaching the maximum strength, the mechanical response exhibits the softening response, characterized by a reduction of stiffness and

capacity. The micromechanical process is characterized by damage and plasticity phenomena. Damage is due to the propagations of microcracks through the material, while plasticity is related to the intergranular displacements and the inelastic deformations which occur during the loading process. Several mechanical models have been developed to represent the behaviour of brittle materials. The most common formulations for materials with softening behaviour are based on continuum damage mechanics, which describe the macroscopic effect of the material cracking through homogenized parameters. Damage-plastic models are more advanced formulations, which consider both damage and plasticity related to the intergranular displacements [30].

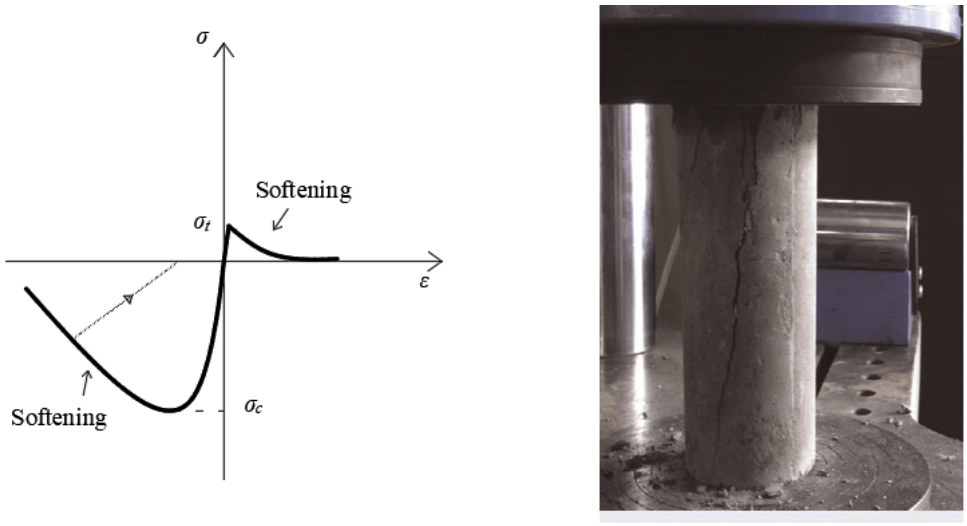

(a) *(b)*

Figure 7: Typical constitutive law of concrete (a) and an example of compression failure of a concrete specimen [52]*(b)*

Sections 2.4.1 and 2.4.2 describe the plasticity and damage models adopted in this work. Subsequently, in Section 2.4.3 the three-dimensional damage-plastic model implemented in *OpenSees* will be introduced and discussed. Finally, Section 2.4.4 proposes an improvement of the damage-plastic model by introducing the concept of partial closure of cracks. In the subsequent paragraphs, the deformation and stress vectors of the three-dimensional material are denoted as:

$$\boldsymbol{\varepsilon} = \{\varepsilon_1, \varepsilon_2, \varepsilon_3, \gamma_{12}, \gamma_{13}, \gamma_{23}\}^T, \quad \boldsymbol{\sigma} = \{\sigma_1, \sigma_2, \sigma_3, \tau_{12}, \tau_{13}, \tau_{23}\}^T \tag{22}$$

2.4.1 Plasticity model

Two different three-dimensional plasticity models are described in this section: the Von Mises (J2) [53] and Drucker-Prager models with isotropic and kinematic hardening [54], [55]. In both cases, the stress-strain relation is defined as:

$$\boldsymbol{\sigma} = \mathbf{C}\,\boldsymbol{\varepsilon}^{e} \;= \mathbf{C}(\boldsymbol{\varepsilon} - \boldsymbol{\varepsilon}^{p}) \tag{23}$$

where $\boldsymbol{\varepsilon}^{e}$ is the elastic strain vector, evaluated as the difference between the total strain, $\boldsymbol{\varepsilon}$, and the plastic strain vector, $\boldsymbol{\varepsilon}^{p}$. The matrix $\mathbf{C}$ is the elastic isotropic stiffness matrix, depending on the Poisson ratio ν and Young modulus E.

In case of **Von Mises model**, the plastic limit function is defined as:

$$f(\boldsymbol{\eta}, \alpha) = |\boldsymbol{\eta}| - \sqrt{\frac{2}{3}}(\sigma_y + H_i \alpha) \tag{24}$$

where σ_y is the yield stress, H_i is the isotropic hardening modulus, while α is the isotropic hardening variable. The vector $\boldsymbol{\eta}$ depends on the deviatoric part of the stress vector $\mathbf{P}\boldsymbol{\sigma}$, where $\mathbf{P}$ is the deviatoric operator, and the kinematic back stress $\boldsymbol{\zeta}$, as follows:

$$\boldsymbol{\eta} = \mathbf{P}\boldsymbol{\sigma} - \boldsymbol{\zeta} \tag{25}$$

The evolution laws of the plastic variables, in case of associative flow rule, are defined by the following equations.

$$\dot{\boldsymbol{\varepsilon}}^{p} = \dot{\lambda}\frac{\partial f}{\partial \boldsymbol{\sigma}} = \dot{\lambda}\,\mathbf{n}, \qquad \dot{\boldsymbol{\zeta}} = \frac{2}{3} H_k \dot{\boldsymbol{\varepsilon}}^{p}, \quad \dot{\alpha} = \sqrt{\frac{2}{3}}\dot{\lambda} \tag{26}$$

The term $\dot{\lambda}$ is the plastic multiplier and H_k is the kinematic hardening, while the normal to the yield surface is equal to $\mathbf{n} = \boldsymbol{\eta}/|\boldsymbol{\eta}|$. The Kuhn-Tucker and consistency conditions govern the plasticity evolution, and are expressed as:

$$\dot{\lambda} \geq 0, \quad f(\boldsymbol{\eta}, \alpha) \leq 0, \quad \dot{\lambda} f(\boldsymbol{\eta}, \alpha) = 0, \quad \dot{\lambda} \dot{f}(\boldsymbol{\eta}, \alpha) = 0 \tag{27}$$

The incremental form of the constitutive law respect to the pseudo-time variable is defined as:

$$\dot{\boldsymbol{\sigma}} = \mathbf{C}^{ep} \dot{\boldsymbol{\varepsilon}} \tag{28}$$

being $\mathbf{C}^{ep}$ the elasto-plastic tangent stiffness matrix. In case of **Von Mises plasticity,** the latter is evaluated as [30]:

$$\mathbf{C}^{ep} = \mathbf{C} - \frac{4G^2 \dot{\lambda}}{|\boldsymbol{\eta}|} \left(\mathbf{I} - \frac{\mathbf{1}\mathbf{1}^T}{3} - \mathbf{n}\mathbf{n}^T \right) - \frac{4G^2 \mathbf{n}\mathbf{n}^T}{2G + 2/3(H_i + H_k)} \tag{29}$$

where K and G are the bulk and shear moduli. $\mathbf{I}$ is the identity matrix vector, while the vector $\mathbf{1}$ is equal to $\mathbf{1} = \{1\ 1\ 1\ 0\ 0\ 0\}^T$.

The **Drucker-Prager plasticity formulation** is based on the Von Mises model and introduces an additional component depending on the volumetric part of the stress tensor, equal to $I_1 = \mathbf{1}^T \boldsymbol{\sigma}$. In this case the yield function with linear isotropic and kinematic hardening is defined as follows:

$$f(\boldsymbol{\eta}, \alpha) = |\boldsymbol{\eta}| - \sqrt{\frac{2}{3}} (\sigma_y + H_i \alpha) + \mu I_1 \tag{30}$$

being μ the frictional coefficient. The elasto-plastic stiffness for **Drucker-Prager plasticity** is calculated through the following formula [33]:

$$\begin{aligned} \mathbf{C}^{ep} = \mathbf{C} - \frac{4G^2 \dot{\lambda}}{|\boldsymbol{\eta}|} \left(\mathbf{I} - \frac{\mathbf{1}\mathbf{1}^T}{3} - \mathbf{n}\mathbf{n}^T \right) \\ - \frac{4G^2 \mathbf{n}\mathbf{n}^T - \ 6GK\mu \mathbf{n}\mathbf{1}^T}{2G + 2/3(H_i + H_k)} \end{aligned} \tag{31}$$

The material constitutive parameters, such as the yield strength σ_y and the frictional coefficient μ, can be defined in terms of the tensile and compressive strength, σ_t and σ_c, through the formulation proposed in [56]:

$$\sigma_y = \frac{2\sigma_c\sigma_t}{\sigma_c + \sigma_t}, \quad \mu = \sqrt{\frac{2}{3}}\left(\frac{\sigma_c - \sigma_t}{\sigma_c + \sigma_t}\right) \tag{32}$$

Figure 8 (a) and (b) illustrate the yield functions in case of Von Mises and Drucker-Prager plasticity, respectively. In the principal stress space, the former is a cylinder parallel to the octahedral axis, while the latter is represented by a cone. In case of Von Mises plasticity, the yield function is symmetric, whereas Drucker-Prager plasticity exhibits a non-symmetric behaviour under tension and compression. These characteristics are better highlighted in Figure 9, (a) and (b), which illustrates the two yield functions in the principal stress plane with $\sigma_3 = 0$. The Von Mises function intersects each axis at σ_y, while the Drucker-Prager function intersects σ_t in tension and σ_c in compression. Moreover, the Drucker-Prager plasticity degenerates into Von Mises model when the material parameters are $\sigma_y = \sigma_t = \sigma_c$.

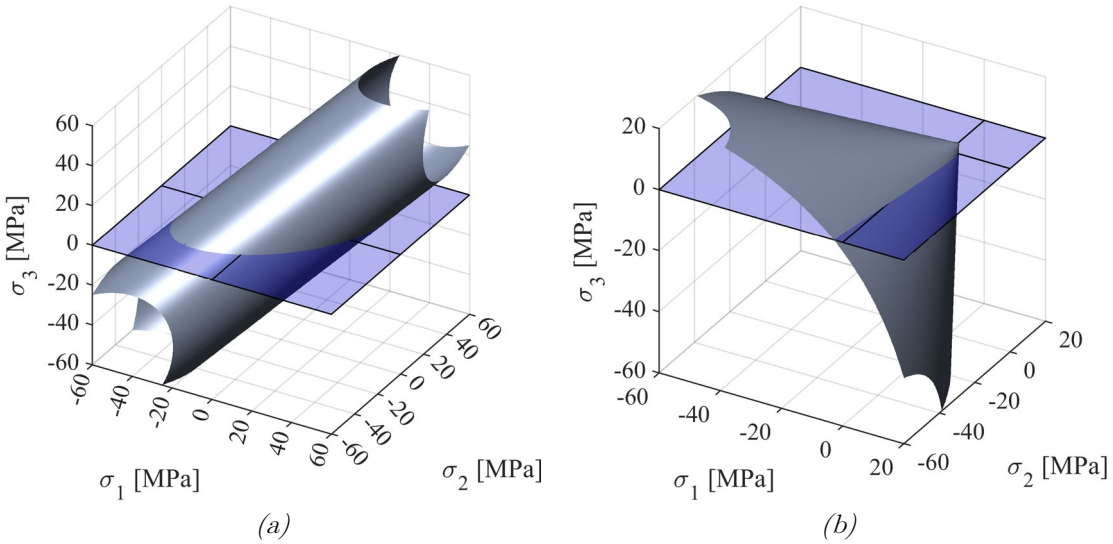

Figure 8: Yield functions in principal stress space: Von Mises (a) and Drucker-Prager (b) plasticity.

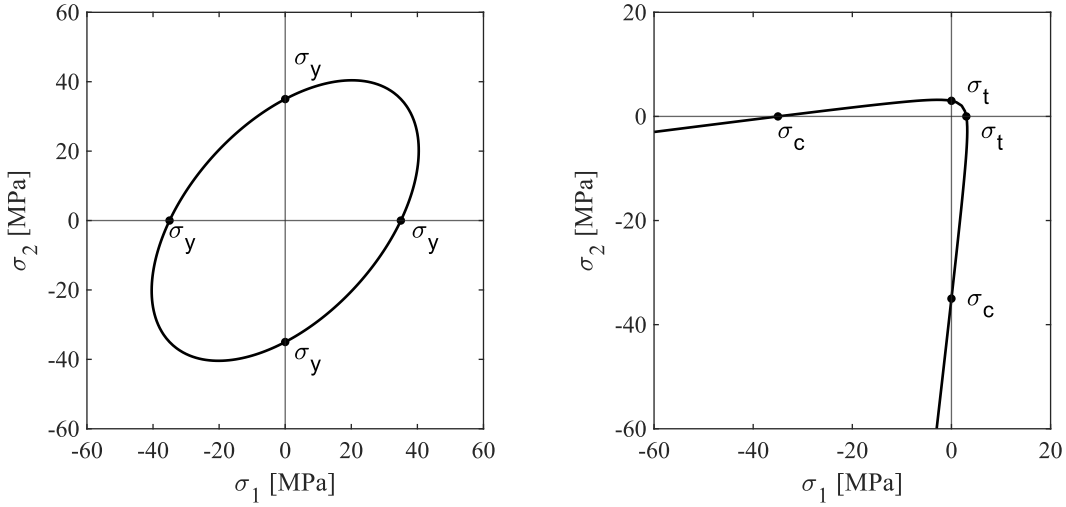

(a) *(b)*

Figure 9: Yield functions in principal stress plane: Von Mises (a) and Drucker-Prager (b) plasticity.

In Figure 10, the cyclic uniaxial behaviour is illustrated for both the Von Mises and Drucker Prager plasticity models, where the material parameters are detailed in Table 1. Two different values of kinematic hardening were adopted. As H_k increases, the slope of the post-yield branch grows. Specifically, Drucker Prager plasticity shows distinct slopes between tension and compression in the post-peak branch.

	E	ν	σ_y	σ_c	σ_t	H_i	H_k
	[MPa]	[-]	[MPa]	[MPa]	[MPa]	[MPa]	[MPa]
Von Mises	30000	0.2	35	-	-	0.006 E	0.01 E 0.02 E
Drucker-Prager	30000	0.2	-	35	3	0.006 E	0.01 E 0.02 E

Table 1: Von Mises and Drucker-Prager plasticity: material parameters in Figure 10

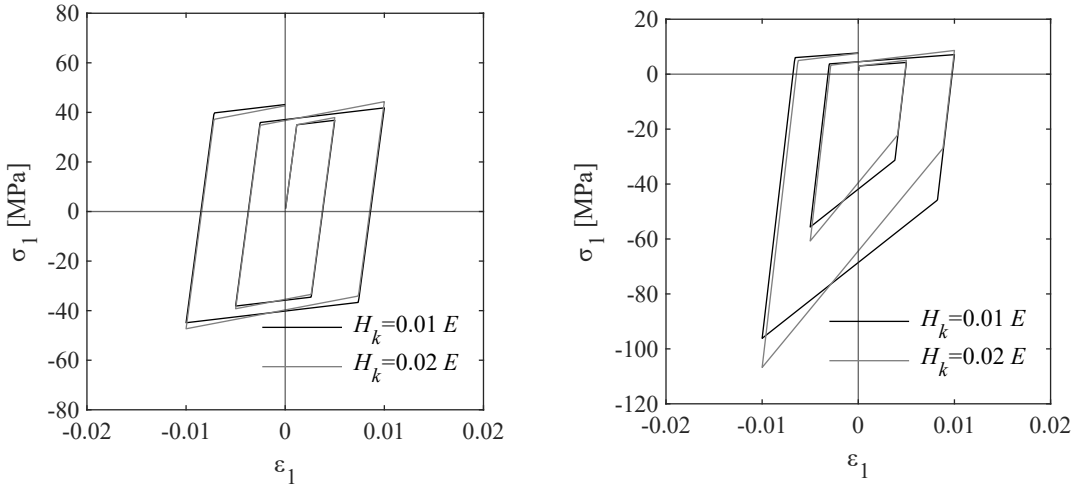

Figure 10: Uniaxial stress-strain law: Von Mises (a) and Drucker-Prager (b) plasticity model.

In common practice, the Von Mises model is used to represent the symmetric behaviour of steel, while the Drucker Prager model is suitable for materials such as concrete with different behaviour in tension and compression. Another approach involves integrating the Von Mises plasticity model with a damage model, controlling tension response solely through damage and compression with a combined model. In this work, an advanced approach is adopted, combining a damage model with Drucker-Prager plasticity. This coupled model provides a more accurate representation of the mechanical response of materials that exhibit asymmetric plastic behaviour in tensile and compression.

2.4.2 Damage model

Continuum Damage Mechanics provides an approach to representing the behaviour of brittle materials and the propagation of microcracks within them in the context of continuum mechanics. A common approach is the use of isotropic damage models which introduces homogenized parameters to describe the macroscopic effect of the material cracking. The internal damage variable D varies between the values 1 and 0, where $D = 1$ represents a completely damaged state, and $D = 0$ denotes undamaged material. The principle of this approach involves defining a relation between the stresses $\boldsymbol{\sigma}$ of the damaged material and the effective stresses $\overline{\boldsymbol{\sigma}}$ of an undamaged fictitious material, called *virgin material*. In the following section, two equivalence principles are briefly introduced: the strain and energy equivalence principles.

The strain principle establishes an equivalence in terms of deformation between the damaged and undamaged material. In this case, the effective stress is expressed as follows:

$$\overline{\boldsymbol{\sigma}} = \mathbf{C}\boldsymbol{\varepsilon} = \frac{\boldsymbol{\sigma}}{(1-D)} \tag{33}$$

being $\mathbf{C}$ the elastic constitutive matrix of the undamaged material. Consequently, the constitutive relation between the stress of the damaged material and the total strain $\boldsymbol{\varepsilon}$ is given by:

$$\boldsymbol{\sigma} = (1-D)\overline{\boldsymbol{\sigma}} = (1-D)\mathbf{C}\boldsymbol{\varepsilon} \tag{34}$$

The energy equivalence principle establishes that the elastic energy stored in a damaged material is equal to the elastic energy of an equivalent undamaged material. Consequently, the effective stress $\overline{\boldsymbol{\sigma}}$ is related to $\boldsymbol{\sigma}$ through the following equation:

$$\overline{\boldsymbol{\sigma}} = \mathbf{C}\boldsymbol{\varepsilon} = \frac{\boldsymbol{\sigma}}{(1-D)^2} \tag{35}$$

In this case, the constitutive law of the damaged material can be expressed as:

$$\boldsymbol{\sigma} = (1-D)^2\overline{\boldsymbol{\sigma}} \ = (1-D)^2\mathbf{C}\boldsymbol{\varepsilon} \tag{36}$$

Several damage models were proposed in literature [57], [58], [59], [60]. This work adopts the damage model proposed in Di Re [33] and Gatta [32], which is an enhancement of that proposed in Addessi [61]. Specifically, this model accounts for the unilateral effect related to the re-closure in compression of tensile cracks. It introduces a damage associated variable D given by the combination of damage variables for tension, D_t, and compression, D_c, as defined in the following expression:

$$D = \alpha_t D_t + \alpha_c D_c \tag{37}$$

where α_t and α_c are weight factors defined as follows:

$$\alpha_t = \frac{\eta_t^2}{\eta_t^2 + \eta_c^2}, \qquad \alpha_c = 1 - \alpha_t \tag{38}$$

The variables η_t and η_c are defined as:

$$\eta_t = \frac{Y_t^e}{Y_{0t} + (a_t Y_t^e + b_t)D}, \quad \eta_c = \frac{Y_c^e}{Y_{0c} + (a_t Y_c^e + b_c)D} \tag{39}$$

being Y_{0c} and Y_{0t} the damage activation thresholds.

The evolution of damage is governed by the associated variables, Y_t and Y_c, which are related to total tensile and compressive strain. In particular, the definition of the associated variables is given by:

$$Y_t = \sqrt{\sum_{i=1}^{3} \langle e_i \rangle_+^2}, \qquad Y_c = \sqrt{\sum_{i=1}^{3} \langle e_i \rangle_-^2 - \kappa \sum_{j \neq i=1}^{3} \langle e_i \rangle_- \langle e_j \rangle_-} \tag{40}$$

being κ a material parameter that determines the shape of the limit function in compression. The variable e_i depends on the principal total strains $\hat{\varepsilon}_j$ according to the following equation:

$$e_i = (1 - 2\nu)\hat{\varepsilon}_i + \nu \sum_{j=1}^{3} \hat{\varepsilon}_j \tag{41}$$

Similarly, Y_t^e and Y_c^e are defined as follows:

$$Y_t^e = \sqrt{\sum_{i=1}^{3} \langle e_i^e \rangle_+^2}, \qquad Y_c^e = \sqrt{\sum_{i=1}^{3} \langle e_i^e \rangle_-^2 - \kappa \sum_{j \neq i=1}^{3} \langle e_i^e \rangle_- \langle e_j^e \rangle_-} \tag{42}$$

where e_i^e is related to the principal elastic strains $\hat{\varepsilon}_j^e$.

$$e_i^e = (1 - 2\nu)\hat{\varepsilon}_i^e + \nu \sum_{j=1}^{3} \hat{\varepsilon}_j^e \tag{43}$$

The progression of the two damage variables is controlled by the damage limit functions for tension and compression, defined as:

$$\begin{aligned} g_t(Y_t, D_t) &= (Y_t - Y_{0t}) - D_t(a_t Y_t + b_t) \\ g_c(Y_c, D_c) &= (Y_c - Y_{0c}) - D_c(a_c Y_c + b_c) \end{aligned} \tag{44}$$

where b_c and b_t influence the rate of damage growth in tension and compression and govern the maximum strength of the material. The parameters a_c and a_t control the slope of the material response curves in the post-peak softening regime.

The damage limit functions are governed by the classical Kuhn-Tucker and consistency conditions:

$$\begin{aligned} &g_t \leq 0, \quad \dot{D}_t \geq 0, \quad \dot{D}_t g_t = 0, \quad \dot{D}_t \dot{g_t} = 0 \\ &g_c \leq 0, \quad \dot{D}_c \geq 0, \quad \dot{D}_c g_c = 0, \quad \dot{D}_c \dot{g_c} = 0 \end{aligned} \tag{45}$$

The unilateral effect due to the re-closure in compression of tensile cracks implies that the damage in tension does not affect, partially or totally, the evolution of the damage in compression. Conversely, the cumulated damage in the compressive state leads to reduction of strength and stiffness also in the tensile behaviour. To introduce this effect in the constitutive model, it is imposed that:

$$D_t \geq D_c \tag{46}$$

An example of uniaxial constitutive response for a cyclic load is illustrated in Figure 11. The mechanical parameters adopted for the damage model are listed in Table 2.

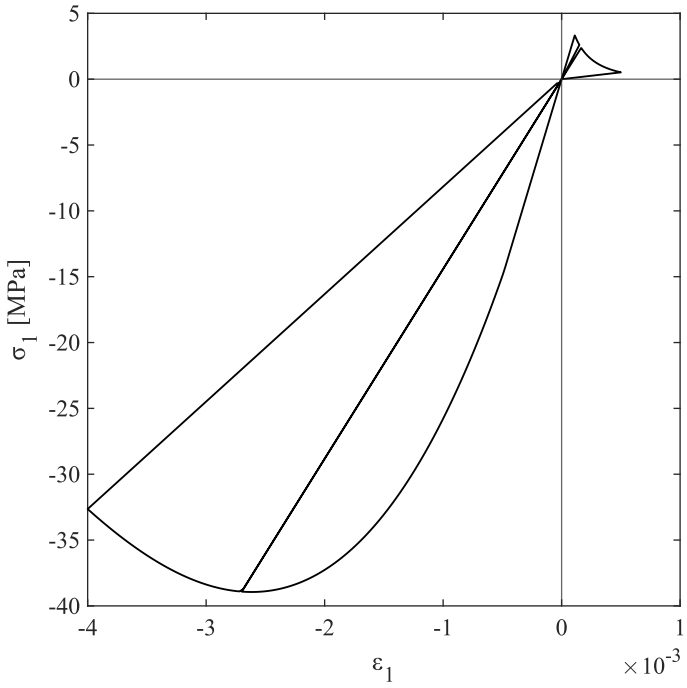

Figure 11: Damage model: Uniaxial stress-strain law.

E	ν	Y_{0c}	a_c	b_c	Y_{0t}	a_t	b_t	κ
[MPa]	[-]	[-]	[-]	[-]	[-]	[-]	[-]	[-]
30000	0.2	3.5e-04	0.1	5e-03	8e-05	0.9	2e-05	0

Table 2: Damage model: material parameters.

Figure 12 shows the imposed strain history and the evolution of damage for the previous example. The damage variable D equals D_t under tensile loading conditions. Conversely, when the strains are negative, D coincides with the compressive damage variable D_c. This behaviour is regulated by the weight functions α_t and α_c, which assume values between 0 and 1, depending on the deformation state. The unilateral re-closure effect of tensile crack is evident in the graph illustrating the damage variation. Specifically, it is observed that, during the compressive loading conditions, D_t assumes the value of D_c when the latter exceeds it. Conversely, the compressive damage D_c remains constant during tensile loading. This implies that the tensile cracking does not influence the compressive strength and stiffness. This work also introduces a damage model which accounts for the reduction of compressive stiffness during the crack closure. Further details are provided in Section 2.4.4.

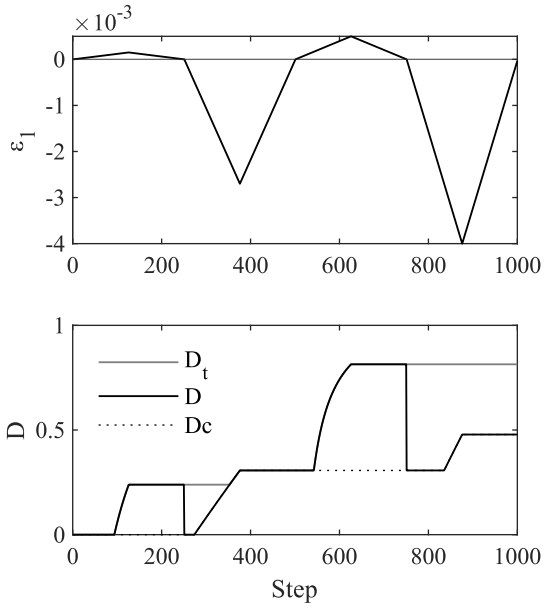

Figure 12: Damage model: strain history and damage evolution.

The damage strain thresholds Y_{0c} and Y_{0t} define the strain elastic limit in compression and tension. To calibrate this parameter, the formulation adopted by Di Re [30] is suggested:

$$Y_{0c} = (1 - \nu - 2\nu^2)\,\sigma_c/E\,, \qquad Y_{0t} < (1 - \nu - 2\nu^2)\,\sigma_t/E \tag{47}$$

where σ_c and σ_{t} are the tensile and compressive strength, respectively. As previously mentioned, the parameters a_c and a_t regulate the softening behaviour, whereas b_c and b_t influence both the peak strength and the rate of damage evolution. Figure 13 provides an example of the influence of these parameters on the material response. In particular, the stress-strain curve and the evolution of damage varying the tensile damage parameters a_t, and b_t are illustrated. It can be observed that the parameter a_t only affects the softening branch, while b_t also influences the peak strength.

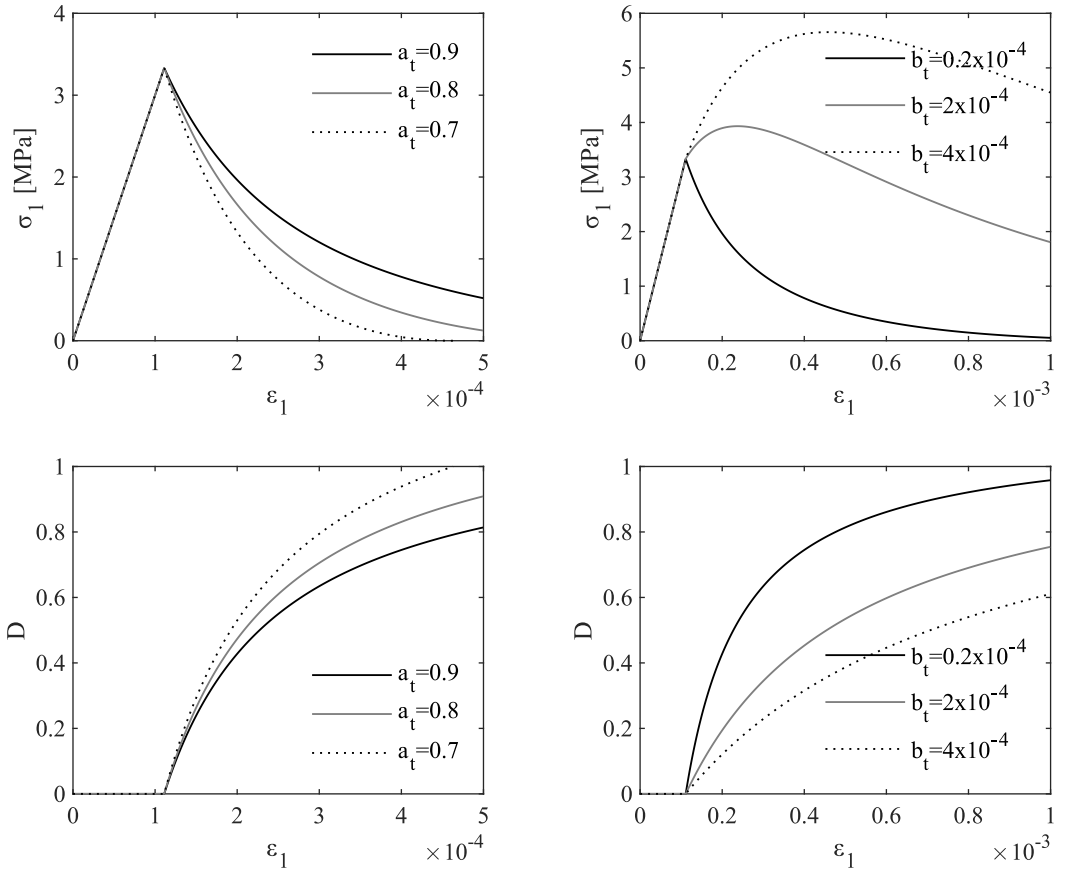

(a) *(b)*

Figure 13: Damage model: Uniaxial stress-strain law and damage evolution varying damage parameter a_t (a) and b_t (b).

2.4.3 Damage-Plastic model

This work adopts the 3D damage-plastic material model for concrete proposed in [18]. Especially, the model considers plasticity and damage mechanisms in compression and tension. It adopts the Drucker-Prager plasticity model described in Section 2.4.1 integrating it with the damage model discussed in Section 2.4.2.

Combining plasticity and damage model, the stress-strain relation becomes:

$$\boldsymbol{\sigma} = (1 - D)^2 \mathbf{C}(\boldsymbol{\varepsilon} - \boldsymbol{\varepsilon}^p) \tag{48}$$

The tangent stiffness matrix is defined as follows:

$$\mathbf{C}_{\mathrm{t}} = (1 - D)^2 \mathbf{C}^{ep} - 2(1 - D)\mathbf{C}\boldsymbol{\varepsilon}^e \frac{\partial D}{\partial \boldsymbol{\varepsilon}} \tag{49}$$

As a result, the incremental form of the equation (48) is expressed by the following relation:

$$\dot{\boldsymbol{\sigma}} = \mathbf{C}_{\boldsymbol{t}} \dot{\boldsymbol{\varepsilon}} \tag{50}$$

where $\dot{\boldsymbol{\sigma}}$ and $\dot{\boldsymbol{\varepsilon}}$ are the stress and strain rate vectors.

An example of the constitutive response under cyclic loading for the damage-plastic model is reported in Figure 14 and Figure 15. The mechanical parameters used are listed in Table 3. Unlike the damage model response shown in Figure 11, the residual plastic deformations in tensile and compression are considered, accurately representing the mechanical behaviour of the material.

E [MPa]	ν [-]	σ_c [MPa]	σ_t [MPa]	H_i [MPa]	H_k [MPa]	
30000	0.2	35	3.3	0.001 E	0.8 E	

Y_{0c} [-]	a_c [-]	b_c [-]	Y_{0t} [-]	a_t [-]	b_t [-]	β [-]
3.5e-04	0.1	5e-03	8e-05	0.9	2e-05	0

Table 3: Damage-plastic model: material parameters

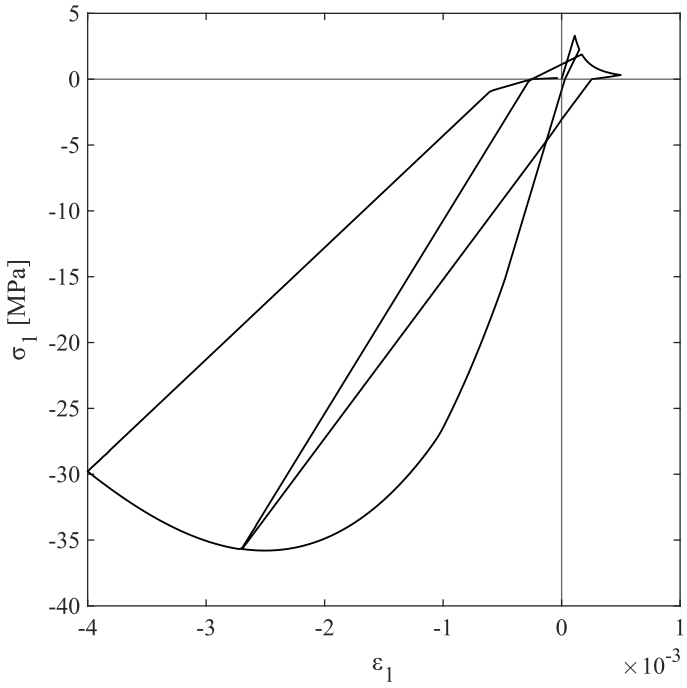

Figure 14: Damage-plastic model: uniaxial stress-strain law.

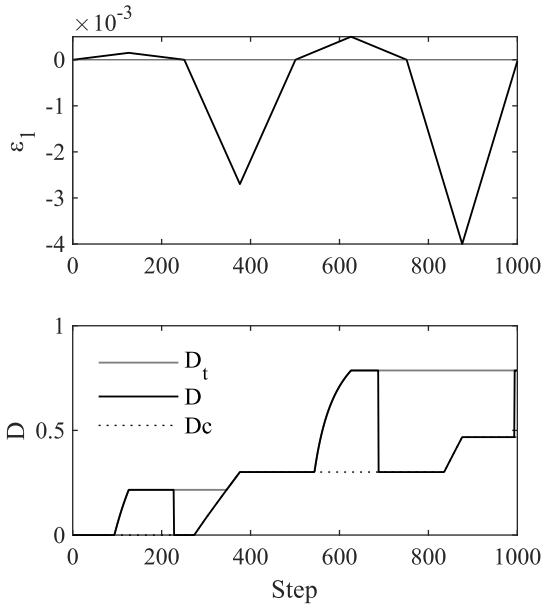

Figure 15: Damage-plastic model: strain history and damage evolution.

2.4.4 Modified Damage-Plastic model with partial closure of cracks

In case of static loading and unloading cycles, the dynamic response is influenced by several mechanical phenomena such as concrete tensile plasticity and the partial closure of cracks induced by the presence of concrete aggregate [36]. The previously described damage-plastic model does not consider the partial closure of cracks, and the recovery of stiffness occurs when transitioning from a state of tension to compression. Typically, this approximation is of minor concern, but it becomes significant when assessing frequency in the unloading phase. These aspects will be further explored in Chapter 4. This study proposes an enhancement of the 3D damage-plastic model to account for the partial closure of cracks in concrete. Especially, the proposed damage-plastic model considers the stiffness matrix reduced by a portion of the tensile damage βD_t during the compression phase, corresponding to $\alpha_c > 0$. The constitutive law of concrete is defined as in equation (48):

$$\boldsymbol{\sigma} = (1 - D)^2 \mathbf{C}(\boldsymbol{\varepsilon} - \boldsymbol{\varepsilon}^p) \tag{51}$$

Unlike the previous model, the damage variable is defined as follows:

$$D = \alpha_t D_t + \alpha_c D_c, \qquad with \;\; \beta D_t < D_c \leq 1 \tag{52}$$

where β is bounded, $0 \leq \beta \leq 1$, and represents the portion of tensile damage that remains in the compression state. Specifically, if β equals 0, the cracks are assumed completely closed, whereas if β equals 1, the cracks are considered fully open. Therefore, the partial closure of cracks is given by intermediate values of β. This model assumes that the compressive stiffness is reduced by the partial closure of cracks until the compressive damage D_c exceeds the value of βD_t. This assumption is a simplified approximation of the real mechanical behaviour. Indeed, as reported in the literature [36], [62], [63], [64], [65], the stiffness of the concrete should be restored as soon as the cracks close. In particular, the complete closure of cracks occurs at a certain level of compression, which approximately equals the tensile strength, if the concrete is undamaged in compression [62], [65]. As stated by Lee [60], there is an objective challenge in modelling the sudden recovery of stiffness near the final cyclic loading stage through the use of continuous models, such as the damage-plastic model. However, in applications of interest where beams are subjected to cyclic loading and unloading, the concrete in the cracked area does not reach compressive stresses sufficiently high for a complete restoration of stiffness.

Therefore, it could be worth for future work to improve the model for complete cyclic loads, to consider the compressive elastic restoration of concrete following the full closure of cracks. Additionally, in the models proposed in literature [36], [65], the transition zone from tension to compression is assumed to be elastic, and the stiffness slope varies depending on the plastic tensile strain and the value of crack closure stress. Differently, the proposed damage-plastic model considers the variation of stiffness in the transition zone as dependent on the tensile damage variable through the factor β.

Figure 16 shows the experimental results obtained in [66] and transformed from the stress-displacement plane to the stress-strain plane according to [65]. The experimental curve is compared to the numerical results adopting $\beta = 0$ and $\beta = 0.75$. The calibrated mechanical parameters are listed in Table 4.

E [MPa]	ν [-]	σ_t [MPa]	Y_{0t} [-]	H_i [MPa]	H_k [MPa]	a_t [-]	b_t [-]	β [-]
3.4e-04	0.2	5e-03	8e-05	0.4E	0.9E	0.92	2e-04	0 - 0.75

Table 4: Material parameters of numerical model in Figure 16

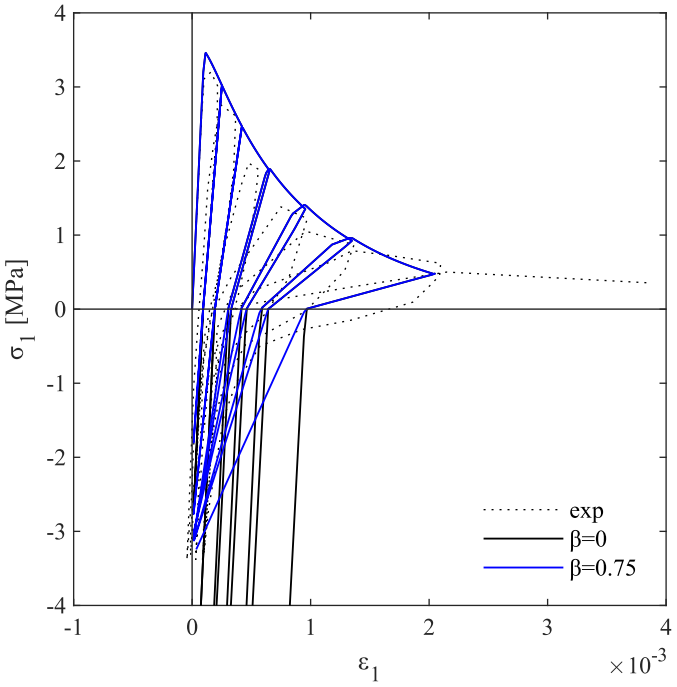

Figure 16: Modified damage-plastic model compared with the experimental results in [66].

It is observed that the model is capable of representing both the residual plastic deformations in tension and the partial closure of the cracks. Specifically, Figure 17 provides a zoomed-in view of the transition zone, which is the phase where the state changes from tension to compression, but the cracks are not yet fully closed. For β equal to 0, corresponding to the condition of the classical damage-plastic model, the compressive stiffness is equal to the initial elastic stiffness, assuming that cracks are suddenly closed. By adopting the proposed modified damage-plastic model, it is possible to approximate the behaviour in the transition phase more accurately. In particular, β was calibrated to obtain the average stiffness value resulting from the experimental test. As previously mentioned, the proposed formulation allows to consider the stiffness variation, so as the tensile damage increases, a lower stiffness is obtained. This characteristic is crucial for correctly calculating the frequency of vibration modes, which will be discussed in detail in Chapter 4.

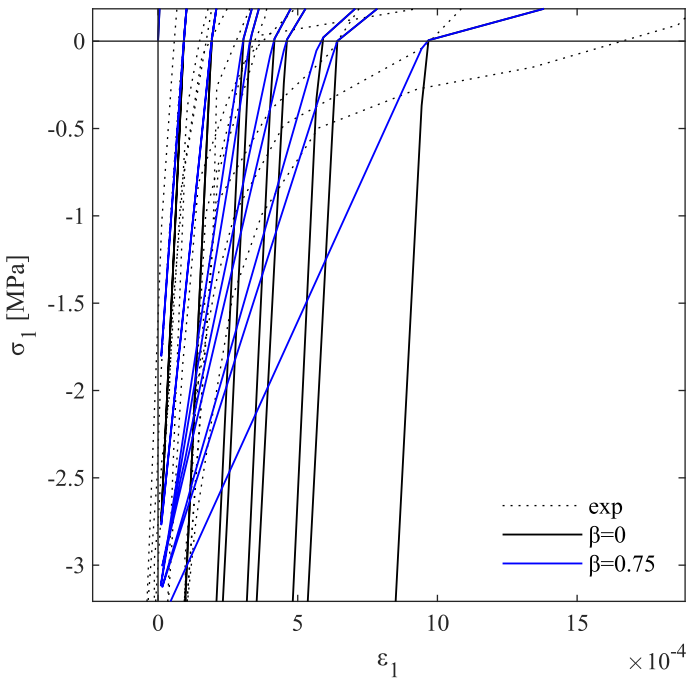

Figure 17: Transition zone - Zoom of Figure 16.

Figure 18 illustrates the strain history and damage evolution of the numerical results. During the compression phase, the total damage D is given by a portion of the tensile damage D_t according to the equation (52). Specifically, in this application D equals 75% of the tensile damage, as highlighted in the figure.

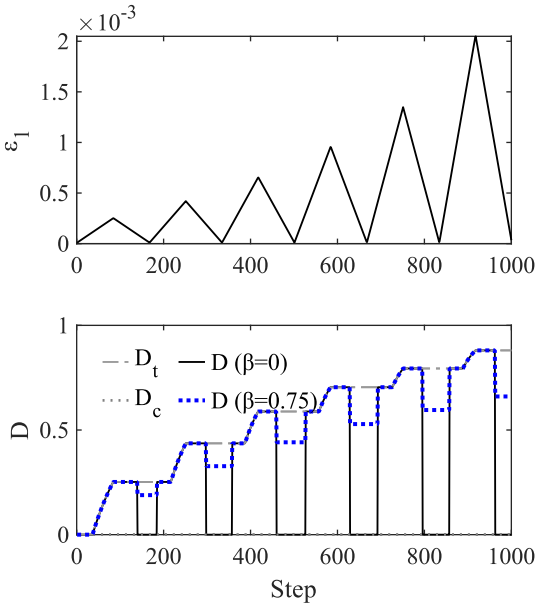

Figure 18: Modified damage-plastic model: strain history and damage evolution.

For the sake of completeness, this paragraph shows the comparison between the results of the model described in Section 2.4.3 and those obtained adopting the modified damage-plastic formulation with a $\beta = 0.5$. The material parameters are specified in Table 3. Figure 19 and Figure 20 illustrate the response under cyclic loading, while Figure 21 and Figure 22 show the behaviour during loading and unloading cycles.

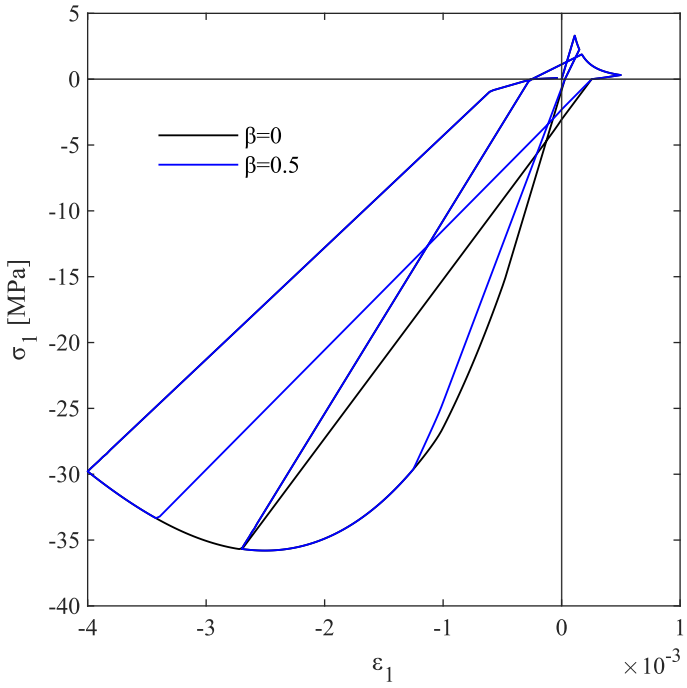

Figure 19: Damage-plastic model vs Modified damage-plastic model: cyclic loading.

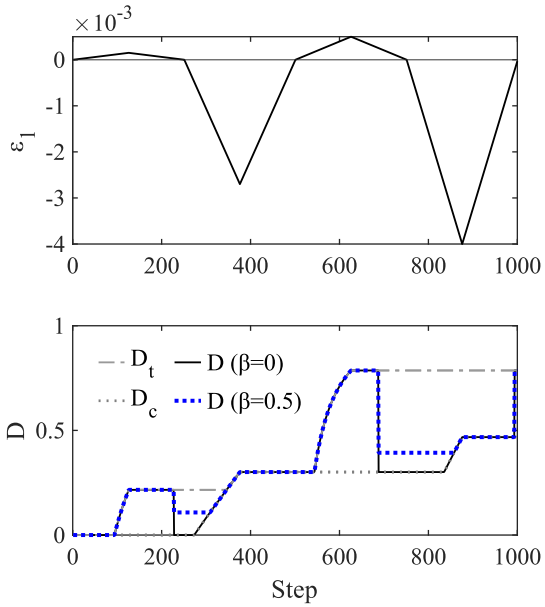

Figure 20: Damage-plastic model vs Modified damage-plastic model: strain history and damage evolution related to Figure 19.

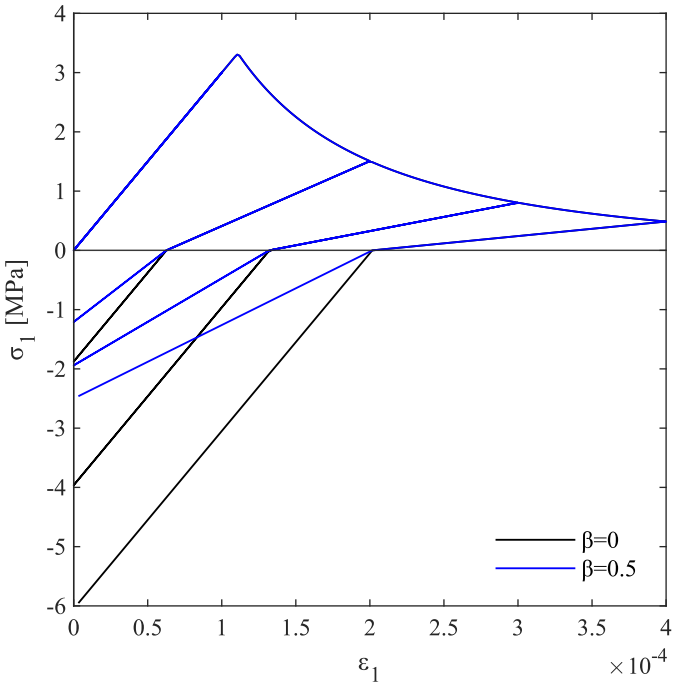

Figure 21: Damage-plastic model vs Modified damage-plastic model: loading and unloading cycle.

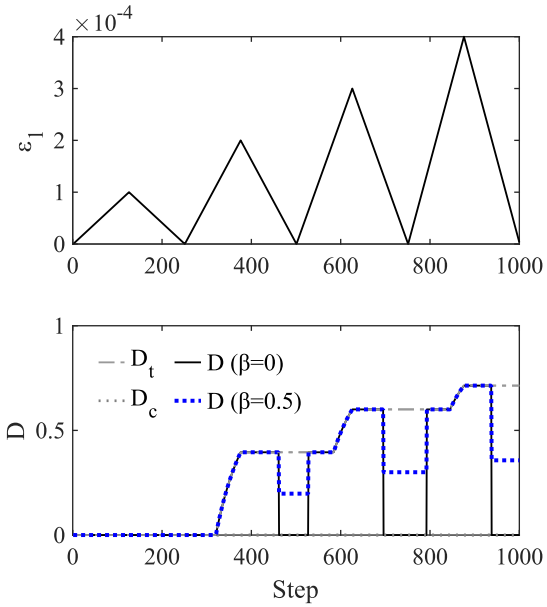

Figure 22: Damage-plastic model vs Modified damage-plastic model: strain history and damage evolution related to Figure 21.

2.5 Regularization Technique

The adoption of strain-softening constitutive laws, as in the case of brittle materials, leads to a pathological mesh dependence of the numerical solution, caused by the ill-posedness of the governing equations [67], [68]. As a result, the structural response may exhibit the localization of damage and/or strains within a limited region. However, the length of this zone is not correlated to the physical properties of the plastic hinge but solely depends on the numerical formulation adopted. Consequently, in the case of strain softening, the numerical structural response loses the objectivity of the solution because the numerical results depend on the choice of the characteristic length of the element. This numerical issue impacts both displacement-based (DB) and force-based (FB) beam element formulation. In a displacement-based approach, the localization of damage and strains takes place within a single element. This occurs as the section deformations are interpolated over the length of each element. Conversely, in the force-based (FB) approach, localization occurs at the integration point, hence the length of localization depends on the specific numerical integration rule adopted [29], [69].

For illustrative purposes, an example is presented to show the impact on the numerical results if the finite element procedure is not regularized. In particular, the experimental test conducted by Tanaka and Park [70] to evaluate the lateral capacity of a reinforced concrete bridge pier was modelled in *OpenSees*. The test characteristics and the mechanical parameters of the materials were adopted consistently with those used in [69]. A displacement-controlled analysis was performed on the bridge pier model. The numerical results are presented in Figure 23 and compared with the experimental results (EXP). A number of elements from 1 to 3 was considered, employing both displacement-based elements (DB) and force-based elements (FB).

The results in Figure 23 highlight the lack of objectivity in the analysis, as in both cases are significantly influenced by the number of elements used. With force-based elements, the characteristic length influences the behaviour in the post-peak phase, whereas the maximum capacity of the element remains independent on the beam discretization. In contrast, the lack of objectivity in displacement-based beam elements affects not only the softening phase but also the pre-peak stage, as extensively demonstrated in [29].

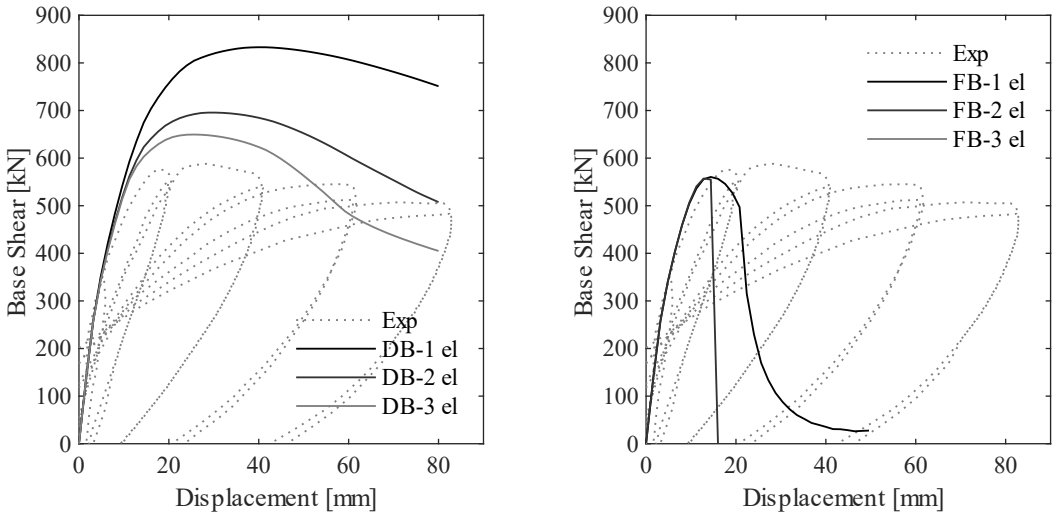

Figure 23: Base shear – displacement without regularization: DB (a) and FB (b) approach.

To overcome localization phenomena and solution non-objectivity, several methods have been proposed in literature. One of the main approaches used for regularization is based on nonlocal formulations [71], [72], [73], [74]. The basic concept of this method is that the damage on a material point is influenced by the mechanical state at the surrounding points. Nonlocal formulations can generally be divided into two main groups: integral formulations and gradient formulations, which can also be categorized as explicit or implicit [61], [75], [76]. Addessi and Ciampi [29] proposed an integral nonlocal formulation adapted for both FB and DB elements. Generally, the use of nonlocal formulation to avoid localization requires specific solving algorithms that can increase the computational effort of the analysis.

Several simplified methods have been developed for the regularization of FB elements [29], [68], [69], [77], [78], [79]. Two different approaches can be distinguished: one operates at the constitutive law level, and the other at the element level. Spacone and Coleman [77] proposed a regularization approach which modifies the material constitutive law of FB element to maintain constant the energy dissipation during the softening behaviour. The element is regularized in terms of force-displacement, but the localization of strains still depends on the adopted mesh size and a second regularization is required [69]. The regularization approach at element level is based on the adoption of an integration method along the element which enforces a priori the localization within a specified plastic hinge length [29], [69], [79]. This method enables achieving a globally objective structural response, while localizing strains within the nonlinear hinge of the element. The next paragraph

will provide a detailed description of several integration methodologies proposed in literature.

2.5.1. Integration methods for FB element formulation

In this section, the regularization methods for the FB element formulation are discussed. As previously mentioned, these methods are based on defining integration point weights, ensuring that the localization of strains occurs within the length of the nonlinear hinge. In force-based elements, the flexibility matrix, as for the compatible basic deformation, is calculated using a numerical integration rule, as follows:

$$\mathbf{F}^e = \int_0^L \mathbf{b}_s{}^T(x)\mathbf{f}_s(x)\mathbf{b}_s(x)\,dx \simeq \sum_{t=1}^{n_G} w_t \mathbf{b}_s{}^T(x_t)\mathbf{f}_s(x_t)\mathbf{b}_s(x_t) \tag{53}$$

where n_G is the number of integration points; x_t and w_t refer to the position and weight associated to each integration point of the element. In nonlinear beam elements, the most used integration rule is the Gauss–Lobatto (GL) quadrature formula, which locates integration points at the ends of the element. The highest order polynomial exactly integrated is $2n_G - 3$.

In case of softening behaviour, strains concentrate at the initial integration point close to the end node of the element. The characteristic length of the region, where localization takes place, is equal to $w_1\, L$, with L equal to the element length. As briefly mentioned in the previous section, the regularization technique involves setting the characteristic length equal to the nonlinear hinge length, which represents the physical zone of the beam where nonlinear mechanisms occur.

The methods assume that the softening behaviour is limited to the nonlinear hinge regions of length $L_{p,i}$ and $L_{p,j}$, located at the ends of the element, while the remaining portion of the element can exhibit an elastic or nonlinear behaviour. To effectively capture the softening behaviour within the hinge regions of the element, it is advantageous to utilize integration rules that meet these requirements [69], [78]:

1. The existence of an integration point at the end of the element where the moment is maximum.
2. The exact integration of quadratic polynomials to obtain the exact solutions for linear curvature distributions.

3. A single integration point in each nonlinear hinge region to integrate strains over the specified lengths $L_{p,i}$ and $L_{p,j}$.

A brief overview of different methodologies available in literature is presented:

a) Midpoint Integration:

In the midpoint integration approach, the positioning of the integration points at the centre of the hinges leads to an increase of the element flexural capacity. Furthermore, this method accurately integrates solely linear functions, yet it introduces errors when integrating quadratic polynomials. Consequently, although meeting criterion 3, it does not fulfil criteria 1 and 2.

b) Endpoint Hinge Integration

Moving the integration points to the element ends at 0 and L characterizes the endpoint integration method. This approach sacrifices accuracy, enabling the exact integration of constant functions. Consequently, it leads to a notable error in representing linear curvature distributions. Thus, the endpoint hinge integration method satisfies the criteria 1 and 3 but falls as for criterion 2.

c) Two-Point Gauss–Radau Integration

The two-point Gauss–Radau integration method considers, in each nonlinear hinge region, two Gauss points which provide the exact integration for linear curvature distributions. Although this method satisfies criteria 1 and 2, it does not fulfil criterion 3 because the characteristic length is equal to the integration weight at the element end ($L_{\mathrm{p}}/4$).

d) Regularized Hinge Integration

The element is divided in three distinct parts: two sub-regions at both ends and an interior region. The length of central region is equal to $L_{int} = L - 2L_e$, where L_e is the length of the end sub-regions. The central zone can employ any numerical integration scheme, whereas the end zones must satisfy the requirement 1. Addessi and Ciampi [29] proposed utilizing Gauss–Lobatto (GL) integration for the end region, while Scott and Fenves [69] suggests the adoption of the Gauss-Radau (GR) scheme. By imposing that the characteristic length L_c associated to the end integration points is equal to $w_1 L_e$, results that $L_e = L_c / w_1$. For example, if an

integration scheme with two GL points is adopted, the element length L_e is equal to $2L_c$ since $w_1 = 1/2$. Figure 24 and Figure 25 show an example of integration scheme, comparing the method proposed by Addessi and Ciampi (AD) with that proposed by Scott (SC).

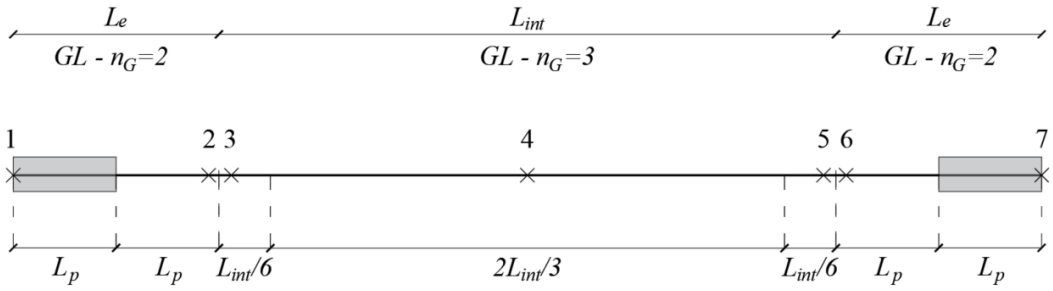

Figure 24: Example of AD integration scheme.

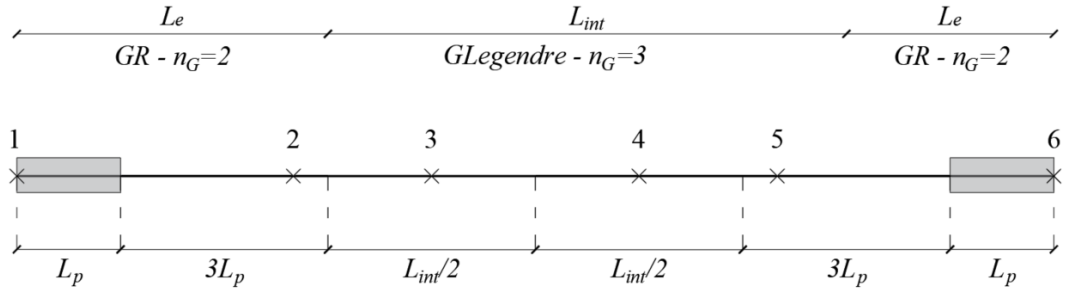

Figure 25: Example of SC integration scheme.

The regularized hinge method effectively overcomes the limitations of the approaches previously discussed. Indeed, this technique defines the characteristic length of the external element equal to the hinge length, thereby setting the length of the end element accordingly. In contrast, the previous methodologies enforce the element length to be equal to the hinge length, either by utilizing a single integration point in case of (a) or (b), or by reducing the characteristic length to a value smaller than the plastic hinge length.

One of the drawbacks of AD and SC methods is their inability to accurately reproduce strain-hardening behaviour. Scott and Hamutcuoglu [79] proposed an alternative approach (SH), adding two additional integration points positioned at small distances from the element end. This method improves the accuracy of the structural response in cases of strain-hardening behaviour, but it leads to an increase of computational effort of the numerical model.

The regularization techniques proposed by Addessi (AD), Scott (SC) and Hamutcuoglu (SH) were applied to the numerical model previously introduced. As suggested in [69], two different hinge lengths were considered, specifically 0.216L and 0.226L. In Figure 26, the numerical results are compared with the experimental cyclic test conducted by Tanaka and Park [70]. In contrast to the non-regularized FB element, shown in Figure 23 (b), the regularized FB element captures the softening behaviour during the post-peak phase. It can be observed that, with the same hinge length, the results are nearly consistent when adopting the AD or SC approaches. However, a more pronounced capacity reduction is observed in the softening branch with the SH method.

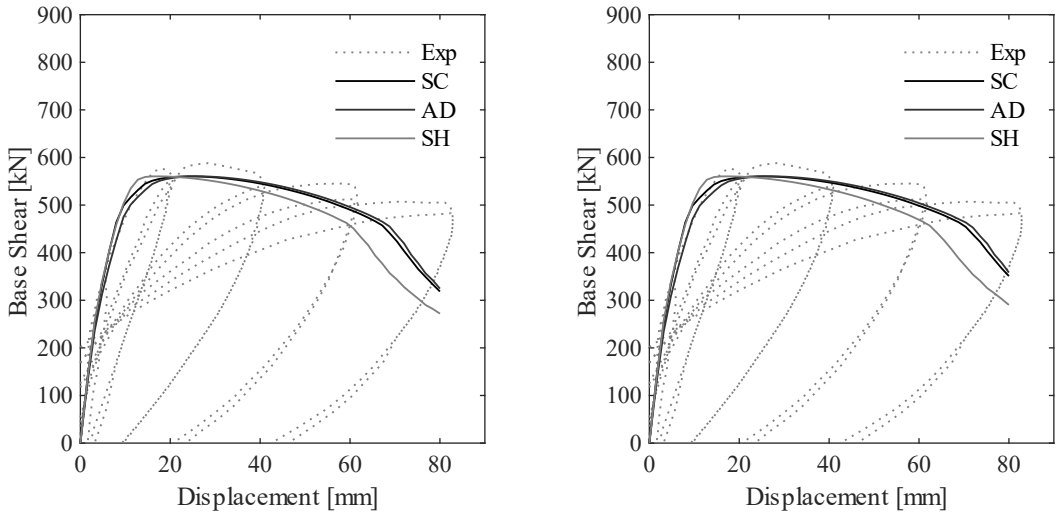

Figure 26: Base shear – displacement FB element with regularization: L_p=0.216L (a) and L_p=0.226L (b)

2.6 Computational Aspects

This section describes some computational aspects concerning the solution algorithm of the fiber beam element integrated with the 3D damage-plastic constitutive model discussed in Section 2.4. Additionally, the following section introduces the software *OpenSees*, illustrating the additions and modifications made to the source code.

To solve nonlinear analyses, existing FEM software commonly adopts the Newton-Raphson algorithm. The latter is a global iteration method, where each element computes the nodal forces and stiffness matrix for given nodal displacement increments. The element solution algorithm is based on a hierarchical approach, encompassing three computational nested procedures: Element State Determination, Section State Determination, and Material State Determination. In details:

- **Element State Determination**. At each iteration of the analysis, it computes the corresponding stiffness matrix and element basic forces.

$$\text{from } \boldsymbol{\varepsilon}_e^i \rightarrow \mathbf{E}_e^i \text{ and } \boldsymbol{\sigma}_e^i \tag{54}$$

- **Section State Determination**: This refers to evaluating the generalized section stiffness and forces at each integration point. It calculates the integrals over the cross-section of fiber response.

$$\text{from } \boldsymbol{\varepsilon}_s^i \rightarrow \boldsymbol{k}_s^i \text{ and } \boldsymbol{\sigma}_s^i \tag{55}$$

- **Material State Determination**: This step involves the evaluation of the material response at each fiber. A condensation procedure is adopted to introduce the 3D material constitutive model.

$$\text{from } \boldsymbol{\varepsilon}_f^i \rightarrow \mathbf{k}_f^i \text{ and } \boldsymbol{\sigma}_f^i \tag{56}$$

Element and Section State Determinations are detailed in Section 2.6.1, while Material State Determination in Section 2.6.3 and Section 2.6.4.

2.6.1 Element and Section State Determination

This section presents the solution algorithm of Element State Determination for FB and DB element formulation. The element iteration procedure within a global DB formulation, commonly used in existing FEM software, is more complex for the FB element [41]. A non-iterative solution algorithm was proposed by Neuenhofer and Filippou [46], which is an enhanced version of that presented by Ciampi and Carlesimo in [80]. In Table 5 and Table 6, the consistent numerical procedures for the DB and FB approaches are illustrated in detail. The matrices and vectors in tables refer to those defined in Section 2.2 and 2.3. In the solution algorithm for the DB approach, the section residual stress $\mathbf{r}^i_{\sigma_s}$ is derived directly from the section state determination, and the residual element stress $\mathbf{R}^i_{\sigma_e}$ is obtained by integrating $\mathbf{r}^i_{\sigma_s}(x)$ along the element. Unlike the DB method, for the FB approach, the section and element residual vectors, $\mathbf{r}^i_{\varepsilon_s}$ and $\mathbf{R}^i_{\varepsilon_e}$, are in terms of strains and basic displacements. As previously mentioned, introducing this procedure into the global Newton-Raphson algorithm is more complex due to the need of additional numerical steps for calculating the element stiffness matrix and the basic forces of the element. For further details, refer to literature [29], [46].

DB approach - Solution algorithm: Element State Determination

$$\Delta\boldsymbol{\varepsilon}^i_e = \boldsymbol{\varepsilon}^i_e \; - \; \boldsymbol{\varepsilon}^{i-1}_e$$

$$\boldsymbol{\varepsilon}^i_s = \boldsymbol{\alpha}_s \, \boldsymbol{\varepsilon}^i_e$$

$$\Delta\boldsymbol{\varepsilon}^i_s = \boldsymbol{\varepsilon}^i_s \; - \; \boldsymbol{\varepsilon}^{i-1}_s$$

Section State Determination: from $\boldsymbol{\varepsilon}^i_s$ → $\mathbf{k}^i_s$ and $\boldsymbol{\sigma}^i_s$

$$\mathbf{r}^i_{\sigma_s} = \boldsymbol{\sigma}^i_s \; - \; (\mathbf{k}^{i-1}_s \; \Delta\boldsymbol{\varepsilon}^i_s + \; \boldsymbol{\sigma}^{i-1}_s)$$

$$\mathbf{K}^i_e = \int_0^L \boldsymbol{\alpha}^T_s \; \mathbf{k}^i_s \; \boldsymbol{\alpha}_s \; dx$$

$$\mathbf{R}^i_{\sigma_e} = \int_0^L \boldsymbol{\alpha}^T_s \;\; \mathbf{r}^i_{\sigma_s} \; dx$$

$$\Delta\boldsymbol{\sigma}^i_e = \mathbf{K}^{i-1}_e \; \Delta\boldsymbol{\varepsilon}^i_e \; + \mathbf{R}^i_{\sigma_e}$$

$$\boldsymbol{\sigma}^i_e = \boldsymbol{\sigma}^{i-1}_e + \Delta\boldsymbol{\sigma}^i_e$$

Table 5: DB approach - Solution algorithm: Element State Determination

FB approach - Solution algorithm - Element State Determination

$$\Delta\boldsymbol{\varepsilon}_e^i = \boldsymbol{\varepsilon}_e^i \; - \; \boldsymbol{\varepsilon}_e^{i-1}$$

$$\Delta\boldsymbol{\sigma}_e^i = \mathbf{K}_e^{i-1} \; \Delta\boldsymbol{\varepsilon}_e^i$$

$$\Delta\boldsymbol{\sigma}_s^i = \mathbf{b}_s \; \Delta\boldsymbol{\sigma}_e^i \; + \mathbf{r}_{\sigma_s}^{i-1}$$

$$\Delta\boldsymbol{\varepsilon}_s^i(x) = \mathbf{f}_s^{i-1} \; \Delta\boldsymbol{\sigma}_s^i$$

$$\boldsymbol{\varepsilon}_s^i = \boldsymbol{\varepsilon}_s^{i-1} + \Delta\boldsymbol{\varepsilon}_s^i$$

Section State Determination: from $\boldsymbol{\varepsilon}_s^i$ → $\mathbf{k}_s^i$ and $\boldsymbol{\sigma}_s^i$

$$\mathbf{f}_s^i = (\mathbf{k}_s^i)^{-1}$$

$$\mathbf{r}_{\varepsilon_s}^i = \mathbf{f}_s^i \; (\boldsymbol{\sigma}_s^{i-1} + \Delta\boldsymbol{\sigma}_s^i - \boldsymbol{\sigma}_s^i)$$

$$\mathbf{F}_e^i = \int_0^L \mathbf{b}_s^T \; \mathbf{f}_s^i \; \mathbf{b}_s \; \; dx$$

$$\mathbf{K}_e^i = (\mathbf{F}_e^i)^{-1}$$

$$\mathbf{R}_{\varepsilon_e}^i = \int_0^L \mathbf{b}_s^T \; \mathbf{r}_{\varepsilon_s}^i \; dx$$

$$\boldsymbol{\sigma}_e^i = \boldsymbol{\sigma}_e^{i-1} \; + \; \Delta\boldsymbol{\sigma}_e^i \; - \mathbf{K}_e^i \; \mathbf{R}_{\varepsilon_e}^i$$

$$\mathbf{r}_{\sigma_s}^i = \mathbf{b}_s \; \boldsymbol{\sigma}_e^i \; - \; \boldsymbol{\sigma}_s^i$$

Table 6: FB approach - Solution algorithm - Element State Determination

The Section State Determination involves evaluating the response of the cross-section in terms of generalized section forces and stiffness. These are subsequently integrated along the length of the element in the Element State Determination. In fiber beam element, the generalized variables are obtained by integrating along the cross-section fiber stress and stiffness, as described in Section 2.3. Table 7 describes the Section State Determination procedure.

Solution algorithm - Section State Determination

$$\boldsymbol{\varepsilon}_f^i = \mathbf{l}_s \; \boldsymbol{\varepsilon}_s^i$$

Material State Determination: from $\boldsymbol{\varepsilon}_f^i \rightarrow \mathbf{k}_f^i$ and $\boldsymbol{\sigma}_f^i$

$$\boldsymbol{\sigma}_s^i = \int_{A_f} \mathbf{l}_s^T \; \boldsymbol{\sigma}_f^i \; dA_f$$

$$\mathbf{k}_s^i = \int_{A_f} \mathbf{l}_s^T \; \mathbf{k}_f^i \; \mathbf{l}_s dA_f$$

Table 7: Solution algorithm - Section State Determination

2.6.2 Static Condensation

A numerical condensation procedure is necessary to integrate the three-dimensional constitutive law, as the 3D damage-plastic, into the beam element formulation. Indeed, the latter is characterized by three strain and stress components, while the three-dimensional material model has six components, which can be decomposed into a principal vector, denoted with *m,* and a secondary vector, denoted with *c*, as follows:

$$\begin{aligned} \boldsymbol{\varepsilon}_f = \boldsymbol{\varepsilon}_m = \{\varepsilon_1, \gamma_{12}, \gamma_{13}\}^T, \quad \boldsymbol{\varepsilon}_c = \{\varepsilon_2, \varepsilon_3, \gamma_{23}\}^T \\ \boldsymbol{\sigma}_f = \boldsymbol{\sigma}_m = \{\sigma_1, \tau_{12}, \tau_{13}\}^T, \quad \boldsymbol{\sigma}_c = \{\sigma_2, \sigma_3, \tau_{23}\}^T \end{aligned} \tag{57}$$

The static condensation involves finding the strain vector $\boldsymbol{\varepsilon}_c$ such that $\boldsymbol{\sigma}_c = 0$ through a nonlinear iterative procedure. Considering the incremental form of the constitutive relation, given by $\dot{\boldsymbol{\sigma}} = \mathbf{C}_t \dot{\boldsymbol{\varepsilon}}$, the matrix tangent stiffness is decomposed as follows:

$$\begin{Bmatrix} \dot{\boldsymbol{\sigma}}_m \\ \dot{\boldsymbol{\sigma}}_c \end{Bmatrix} = \begin{bmatrix} \mathbf{C}_{t,mm} & \mathbf{C}_{t,mc} \\ \mathbf{C}_{t,cm} & \mathbf{C}_{t,cc} \end{bmatrix} \begin{Bmatrix} \dot{\boldsymbol{\varepsilon}}_m \\ \dot{\boldsymbol{\varepsilon}}_c \end{Bmatrix} \tag{58}$$

Imposing $\dot{\boldsymbol{\sigma}}_c = 0$, the condensed stiffness matrix is given by:

$$\hat{\mathbf{C}}_{t,m} = \mathbf{C}_{t,mm} - \mathbf{C}_{t,mc}(\mathbf{C}_{t,cc})^{-1}\mathbf{C}_{t,cm} \tag{59}$$

Consequently, the condensed constitutive relation is defined as:

$$\dot{\boldsymbol{\sigma}}_m = \hat{\mathbf{C}}_{t,m} \dot{\boldsymbol{\varepsilon}}_m \tag{60}$$

Di Re [30] proposed two different nonlinear iteration procedures for material condensation. The first procedure introduces an iterative algorithm within the element state determination. In contrast, the second procedure adopts a consistent non-iterative approach, which carries the residual vectors to the upper level of analysis, significantly reducing the computational effort. The condensation procedure does not affect the equations governing the element and material state determination. In this work, a condensation procedure at the element level available in *OpenSees* is adopted. Further details are provided in the Section 2.7.

2.6.3 Solution algorithm for 3D damage-plastic model

The following section outlines the solution algorithm for the 3D damage-plastic model. The procedure is based on a predictor-corrector algorithm model, consisting of two phases [29], [30], [32], [33], [61], [81]. The first phase, the *predictor phase*, solves the elasto-plastic problem through the return mapping algorithm, maintaining the damage constant. In the second phase, referred to as the *correction phase*, the damage variables are determined while the total and plastic strains are blocked. In Table 8, a brief overview of the solution procedure is provided. The detailed algorithm is presented in Table 9, where n+1 denotes the Newton-Raphson iteration at the current step. The implemented solution algorithm is consistent because the iterations are conducted at global level rather than at material level.

Elasto-Plastic Predictor Phase		**Damage Corrector**
Elastic predictor	Plastic corrector	
$\Delta\boldsymbol{\varepsilon} = \mathbf{L}^e \Delta\mathbf{u}^e$	$\Delta\boldsymbol{\varepsilon} = \mathbf{0}$	$\Delta\boldsymbol{\varepsilon} = \mathbf{0}$
$\Delta\boldsymbol{\varepsilon}^p = \mathbf{0}$	$\Delta\boldsymbol{\varepsilon}^p = \begin{cases} \mathbf{0}, & f(\boldsymbol{\eta}, \alpha) < 0 \\ \Delta\lambda\, \mathbf{n}, & f(\boldsymbol{\eta}, \alpha) \geq 0 \end{cases}$	$\Delta\boldsymbol{\varepsilon}^p = \mathbf{0}$
$\Delta\boldsymbol{\zeta} = \mathbf{0}$	$\Delta\boldsymbol{\zeta} = \begin{cases} \mathbf{0}, & f(\boldsymbol{\eta}, \alpha) < 0 \\ \frac{2}{3} H_k \Delta\boldsymbol{\varepsilon}^p, & f(\boldsymbol{\eta}, \alpha) \geq 0 \end{cases}$	$\Delta\boldsymbol{\zeta} = \mathbf{0}$
$\Delta\alpha = \mathbf{0}$	$\Delta\alpha = \begin{cases} \mathbf{0}, & f(\boldsymbol{\eta}, \alpha) < 0 \\ \sqrt{\frac{2}{3}} \Delta\lambda, & f(\boldsymbol{\eta}, \alpha) \geq 0 \end{cases}$	$\Delta\alpha = \mathbf{0}$
$\Delta D_t = 0$	$\Delta D_t = 0$	$\Delta D_t = 0, \quad g_t(Y_t, D_t) < 0$ $D_t = \frac{(Y_t - Y_{0t})}{(a_t Y_t + b_t)}, \quad g_t(Y_t, D_t) \geq 0$
$\Delta D_c = 0$	$\Delta D_c = 0$	$\Delta D_c = 0, \quad g_c(Y_c, D_c) < 0$ $D_c = \frac{(Y_c - Y_{0c})}{(a_c Y_c + b_c)}, \quad g_c(Y_c, D_c) \geq 0$

Table 8: Solution procedure for 3D damage-plastic model

Elasto-Plastic Predictor

From analysis: $\boldsymbol{\varepsilon}_{n+1}$ and all parameters at the previous step n

$\boldsymbol{\sigma}_{n+1}^{trial} = \mathbf{C}(\boldsymbol{\varepsilon}_{n+1} - \boldsymbol{\varepsilon}_n^p)$

if $f(\boldsymbol{\eta}_{n+1}, \boldsymbol{\zeta}_n, \alpha_n) < 0$

$\boldsymbol{\varepsilon}_{n+1}^p = \boldsymbol{\varepsilon}_n^p, \quad \boldsymbol{\zeta}_{n+1} = \boldsymbol{\zeta}_n, \quad \alpha_{n+1} = \alpha_n$

else $\dot{\lambda}_{n+1} = \dfrac{f(\boldsymbol{\eta}_{n+1}, \boldsymbol{\zeta}_n, \alpha_n)}{2G + 2/3(H_k + H_i)}, \quad \boldsymbol{\varepsilon}_{n+1}^p = \boldsymbol{\varepsilon}_n^p + \dot{\lambda}_{n+1}\mathbf{n}_{n+1}$

$\alpha_{n+1} = \alpha_n + \sqrt{\dfrac{2}{3}}\dot{\lambda}_{n+1} \quad and \quad \boldsymbol{\zeta}_{n+1} = \dfrac{2}{3}H_k\boldsymbol{\varepsilon}_{n+1}^p$

end

$\boldsymbol{\sigma}_{n+1}^{trial} = \mathbf{C}(\boldsymbol{\varepsilon}_{n+1} - \boldsymbol{\varepsilon}_{n+1}^p) = \mathbf{C}\boldsymbol{\varepsilon}_{n+1}^e, \quad \text{calculate} \quad \mathbf{C}^{ep}$

Damage Corrector

Calculate:

$\boldsymbol{\varepsilon}_{i,n+1}, \quad \boldsymbol{\varepsilon}_{i,n+1}^e, \quad e_{i,n+1}, \quad e_{i,n+1}^e, \quad e_{i,n+1}^e, \quad i = 1, ..$

$Y_{t,n+1}, \quad Y_{c,n+1}, \quad Y_{t,n+1}^e, \quad Y_{c,n+1}^e$

if $g_t(Y_{t,n+1}, D_{t,n}) < 0$ and $g_c(Y_{c,n+1}, D_{c,n}) < 0$

$D_{t,n+1} = D_{t,n}, \quad D_{c,n+1} = D_{c,n}$

else $D_{t,n+1} = \dfrac{Y_{t,n+1} - Y_{0t}}{a_t Y_{t,n+1} + b_t}, \quad D_{c,n+1} = \dfrac{Y_{c,n+1} - Y_{0c}}{a_t Y_{c,n+1} + b_c}$

$\eta_{t,n+1} = \dfrac{Y_{t,n+1}^e}{Y_{0t,n+1} + (a_{t,n+1}Y_{t,n+1}^e + b_{t,n+1})D_n},$

$\eta_{\mathrm{c,n+1}} = \dfrac{\mathrm{Y_{c,n+1}^e}}{\mathrm{Y_{0c,n+1}} + (a_{\mathrm{c,n+1}}\mathrm{Y_{c,n+1}^e} + b_{\mathrm{c,n+1}})\mathrm{D_n}}$

$\alpha_{t,n+1} = \dfrac{\eta_{t,n+1}^2}{\eta_{t,n+1}^2 + \eta_{c,n+1}^2}, \quad \alpha_{c,n+1} = 1 - \alpha_{t,n+1}$

$D_{n+1} = \alpha_{t,n+1}D_{t,n+1} + \alpha_{c,n+1}D_{c,n+1}$

end

$\boldsymbol{\sigma}_{n+1} = (1 - D_{n+1})^2\mathbf{C}(\boldsymbol{\varepsilon}_{n+1} - \boldsymbol{\varepsilon}_{n+1}^p), \quad \mathbf{C}_{t,n+1} = (1 - D_{n+1})^2\mathbf{C}_{n+1}^{ep}$

Table 9: Solution algorithm for 3D damage-plastic model [30]

2.6.4 Solution algorithm for modified damage-plastic model

This section introduces the solution algorithm for the modified damage-plastic model, detailed in Section 2.4.4. In Table 10, the part of the algorithm highlighted in blue represents the additional component compared to the 3D damage-plastic algorithm, described in the related Table 9.

Elasto-Plastic Predictor

See Table 9

Damage Corrector

Calculate:

$\varepsilon_{i,n+1}, \quad \varepsilon^e_{i,n+1}, \quad e_{i,n+1}, \quad e^e_{i,n+1}, \quad e^e_{i,n+1}, \quad i = 1,..$

$Y_{t,n+1}, \quad Y_{c,n+1}, \quad Y^e_{t,n+1}, \quad Y^e_{c,n+1}$

if $g_t(Y_{t,n+1}, D_{t,n}) < 0$ and $g_c(Y_{c,n+1}, D_{c,n}) < 0$

$D_{t,n+1} = D_{t,n}, \quad D_{c,n+1} = D_{c,n}$

else $D_{t,n+1} = \dfrac{Y_{t,n+1} - Y_{0t}}{a_t Y_{t,n+1} + b_t}, \quad D_{c,n+1} = \dfrac{Y_{c,n+1} - Y_{0c}}{a_t Y_{c,n+1} + b_c}$

$$\eta_{t,n+1} = \frac{Y^e_{t,n+1}}{Y_{0t,n+1} + (a_{t,n+1} Y^e_{t,n+1} + b_{t,n+1}) D_n},$$

$$\eta_{c,n+1} = \frac{Y^e_{c,n+1}}{Y_{0c,n+1} + (a_{c,n+1} Y^e_{c,n+1} + b_{c,n+1}) D_n}$$

$$\alpha_{t,n+1} = \frac{\eta^2_{t,n+1}}{\eta^2_{t,n+1} + \eta^2_{c,n+1}}, \quad \alpha_{c,n+1} = 1 - \alpha_{t,n+1}$$

if $D_{c,n+1} < \beta D_{t,n+1}$

$D_{n+1} = \alpha_{t,n+1} D_{t,n+1} + \alpha_{c,n+1} \beta D_{t,n+1}$

else

$D_{n+1} = \alpha_{t,n+1} D_{t,n+1} + \alpha_{c,n+1} D_{c,n+1}$

end

end

$\sigma_{n+1} = (1 - D_{n+1})^2 \mathbf{C}(\varepsilon_{n+1} - \varepsilon^p_{n+1}), \quad \mathbf{C}_{t,n+1} = (1 - D_{n+1})^2 \mathbf{C}^{ep}_{n+1}$

Table 10: Solution algorithm for Modified damage-plastic model

2.7 OpenSees Framework and Modelling strategy

This paragraph briefly introduces the software framework in which the 3D damage-plastic model has been integrated. *OpenSees*, an acronym for the *Open System for Earthquake Engineering Simulation*, is an open-source software framework originally designed for applications in the field of earthquake engineering [82]. The software platform is based on finite element methodologies and, due to its open-source nature, is widely used in the academic world. Unlike more common commercial software, it is a community-based environment designed to promote innovation and research. Especially, a fundamental characteristic of *OpenSees* is the possibility to add new element classes and libraries without necessitating modifications to the existing code. *OpenSees* is an *object-oriented* software framework, and its modular architecture enhances code flexibility and extendibility compared to traditional programming methodologies. Indeed, in conventional methods, data and algorithms are often within a single subroutine or procedure, leading to both a code redundancy and a complicated software maintenance [83], [84], [85], [86], [87]. The specific advantage of utilizing software developed with an object-oriented approach is detailed in scientific literature [88]. The source code of *OpenSees* is mainly written in the programming language C++, but it also includes the use of other languages, specifically C and Fortran.

The software architecture is composed of four main types of objects [87], [89], which are indicated in the dark grey blocks in Figure 27. In particular:

- *Model Builder* creates the finite element model subdividing the geometry into elements and nodes. Additionally, it assigns loads and constraints.
- *Domain* is responsible for storing the objects generated by the *ModelBuilder* and providing to the *Analysis* and *Recorder* access to these objects.
- *Analysis* governs the analysis procedure. It is composed by several sub-objects that define the type, static or transient, and the parameters of the analysis.
- *Recorder* monitors output variables during the analysis based on user-defined parameters set during the input phase.

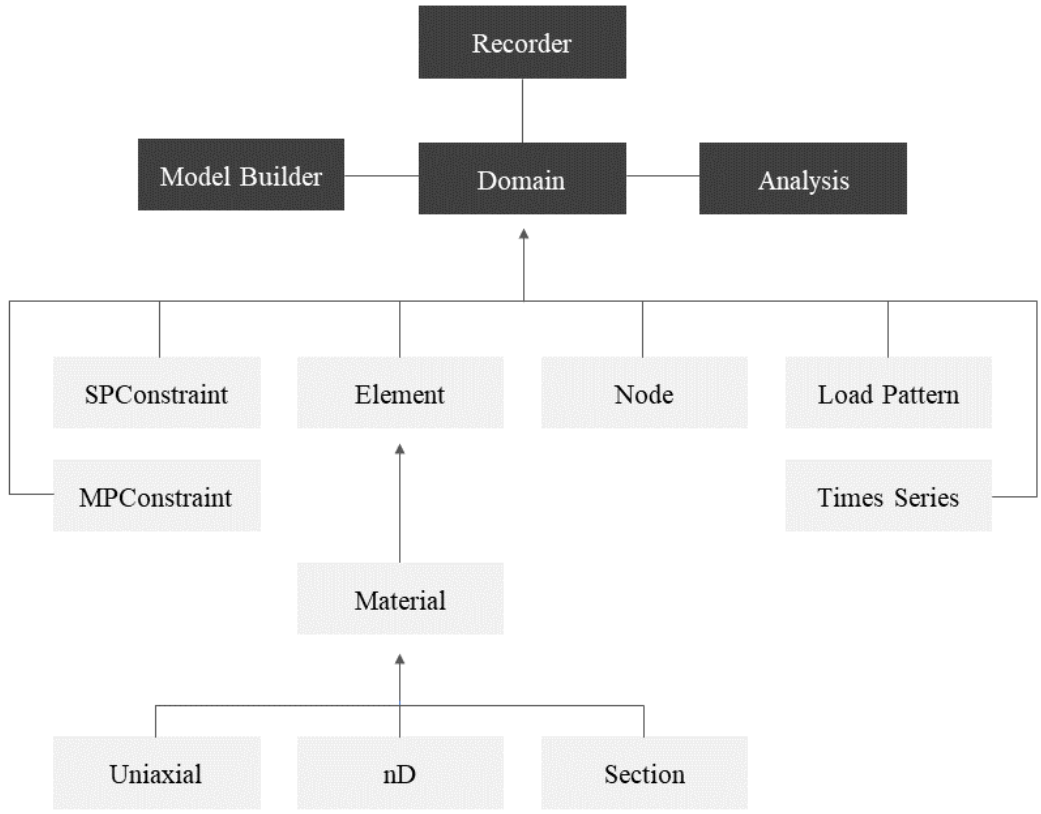

Figure 27: OpenSees software packages: Class diagram of high-level domain, analysis, and model building classes [84], [87]

OpenSees can be used either as a *Developer* or simply as a *User*. In the former case, *OpenSees* is utilized as framework to create new sub-classes, such as elements or materials. Developers can access the source code via shared online repositories, such as *GitHub*. As previously mentioned, the programming language is C++, but there is also the possibility to program in Fortran or C. There are mainly two methods to add a new class: the first involves compiling the entire program and producing a new executable (*.exe*). The second method is to create a *dynamic link library,* which can be used with the existing executable without the need to recompile the entire program. In this work, the changes and additions to the source code have been programmed in C++ and the first method has been adopted. Unlike *Developers*, *Users* can download directly the pre-compiled interpreter of the software, tailored to different computing needs. This includes *OpenSees.exe*, which is designed for sequential computing, ideal for standard analyses. For more complex analysis, parallel versions like *OpenSeesSP.exe* and *OpenSeesMP.exe* are also available. These versions leverage multi-threading and parallel processing capabilities, offering enhanced performance and efficiency for more computational demanding

simulations. *Users* can operate at the command level, where they can construct objects from existing classes available in the framework. The interaction with *OpenSees* occurs through input files, which are scripted in the Tcl (*Tool Command Language*) language. In recent years, the development of the *OpenSeesPy* interpreter has represented a significant advancement, facilitating the scripting of input files. Indeed, this interpreter enables the writing of input commands using *Python*, a language that is currently much more widespread in the research community. To facilitate the input of data and the visualization of outputs, specialized software serving as both pre-processor and post-processor has been developed. This is particularly crucial for handling complex FEM models, such as in case of bridges or entire buildings, where the definition of geometries and the management of several initial input parameters may be more demanding. In this work, the software *STKO* (Scientific ToolKit for OpenSees)[90], [91], developed by *Asdea Software Technology*, was adopted to generate and visualize FEM models. Especially, *STKO* is an *OpenSees GUI* (Graphical User Interface), combining the power of *OpenSees* solvers with the convenience of a user-friendly graphical interface. It enables users to generate a TCL input file for *OpenSees* and subsequently interpret the output file via its graphical interface. Additionally, it includes a Python scripting interface for the customization of results. Figure 28 schematically represents the tools for *Users* and *Developers*.

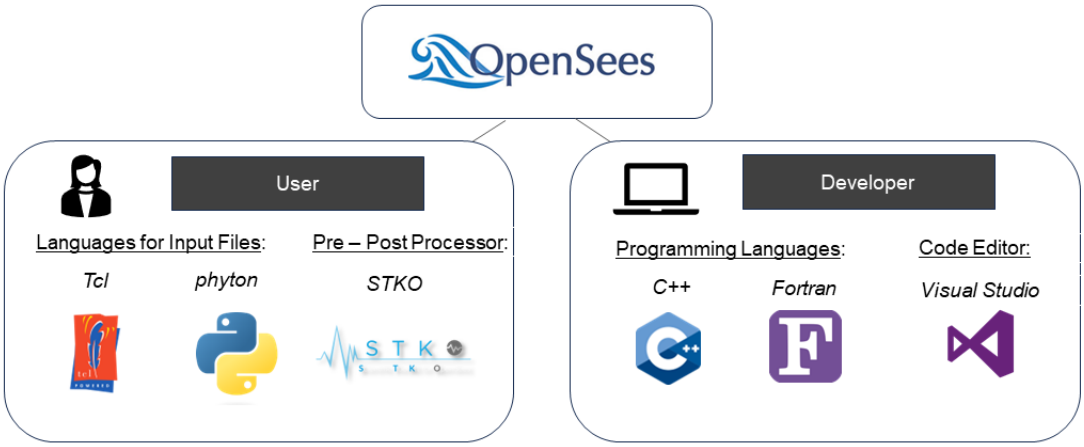

Figure 28: Tools to for OpenSees Users and Developers

Figure 29 shows the methodology adopted in this work for utilizing *OpenSees* as *User* and *Developer*. The process began with the procurement of the *OpenSees* source code, which was subsequently adapted to the specific objectives of the research work. This customization involved the modifications of pre-existing classes

and the introduction of new ones, which will be described in the following section. After these modifications, *OpenSees* was compiled to generate the executable file *NewOpenSees.exe*. To facilitate the definition of FEM model input parameters, the *STKO* software was adopted as a pre-processing tool. *STKO* provides the capability to directly execute the analysis or, as an alternative, to generate input files through the 'Write Input File' command. To incorporate the new implementations, which are not available in the *STKO* library, it is necessary to generate and modify the Tcl input files. Subsequently, the analysis can be run using the new executable, *NewOpenSees.exe*. Finally, outputs can be visualized directly through the *STKO* post-processor for a comprehensive and detailed view. This feature is particularly valuable in case of complex models, allowing for a more effective interpretation of the structural behaviours.

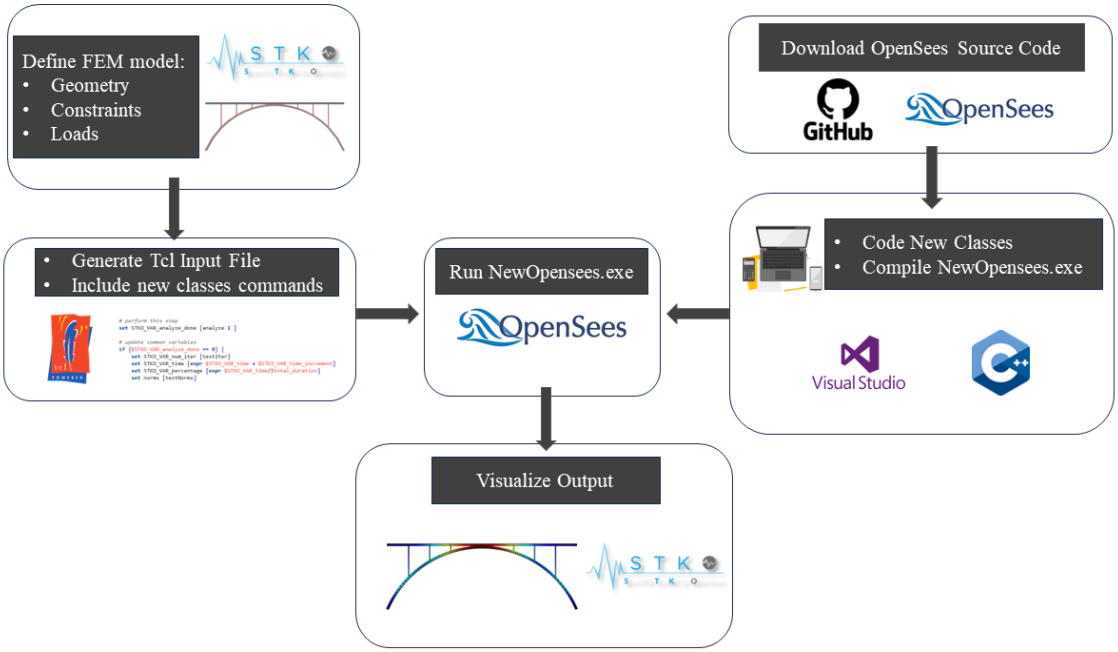

Figure 29: Methodology proposed for utilizing OpenSees as User and Developer.

2.7.1 Fiber Beam Element in *OpenSees*

In this section, a description of the fiber beam element implemented in *OpenSees* is provided. The beam formulation is composed by several subclasses. In particular [85]:

- **Element Class**: this class defines the formulation of the beam element, discussed in Section 2.2. In the case of distributed nonlinearity, two types of elements are distinguished: *DispBeamColumn and ForceBeamColumn*, which represent the DB and FB beam element formulation respectively. The latter is based on the non-iterative consistent element state determination algorithm, proposed by [46], where the residual error is carried into the global solution algorithm. Alternatively, the iterative form of the flexibility formulation can also be adopted [85].
- **Integration Class**: it defines the type of integration along the x-axis of the beam element. Specifically, it determines the positions and weights of the integration points, where the section stiffness and generalized section stresses are evaluated. Section 2.5 discusses various standard integration techniques to regularize the FB beam element. In *OpenSees*, several types of integration methods are already implemented. For example, *RegularizedHinge* represents the integration rules proposed by Scott and Hamutcuoglu [79]. Additionally, there is the possibility to use the class *UserDefined* to define the position and weights of all integration points. Adopting this class, it's also possible to integrate in *OpenSees* the regularization technique proposed by Addessi and Ciampi [29], described in Section 2.5.
- **Section Class**: the Section Class is responsible for modelling the cross-section of beam elements by subdividing them into fibers. It computes the section forces and stresses by integrating the stress vector and stiffness of each fiber in the cross-section. In *OpenSees*, there are two distinct classes: *FiberSection* and *NDFiberSection*. The former is adopted in case of uniaxial material law, while the latter is for three-dimensional constitutive law, called *NDMaterial*. *NDFiberSection* requires the adoption of a wrapper class that performs static condensation, as described in Section 2.6.2. Specifically, for static condensation, the *BeamFiber* class is adopted in this work.

- **Material Class**: this defines the nonlinear behaviour of materials at the fiber levels. As previously mentioned, *OpenSees* differentiates between two material classes: *UniaxialMaterial* and *NDMaterial*. These classifications are based on the number of stress and strain components defined by the constitutive law. In *OpenSees* library, an extensive range of materials is available, and for more detailed information, it is recommended to refer to the software manual.

2.7.2 New classes introduced in *OpenSees*

Figure 30 shows the new classes implemented in *OpenSees*. To include the modelling of tendons in prestressed bridges, this work adopts a modified version of the *NDFiberSection*, introduced by [81] and described in Chapter 3. The new material classes are the *DamagePlastic3d* and *PartialDamage*. The first law represents the damage-plastic model based on the formulation discussed in Section 2.4.3. The solution algorithm, written in C++, is detailed in section 2.6.3. *PartialDamage* is the added class referred to the modified damage-plastic model with partial closure of cracks, described in Section 2.4.4 and 2.6.4.

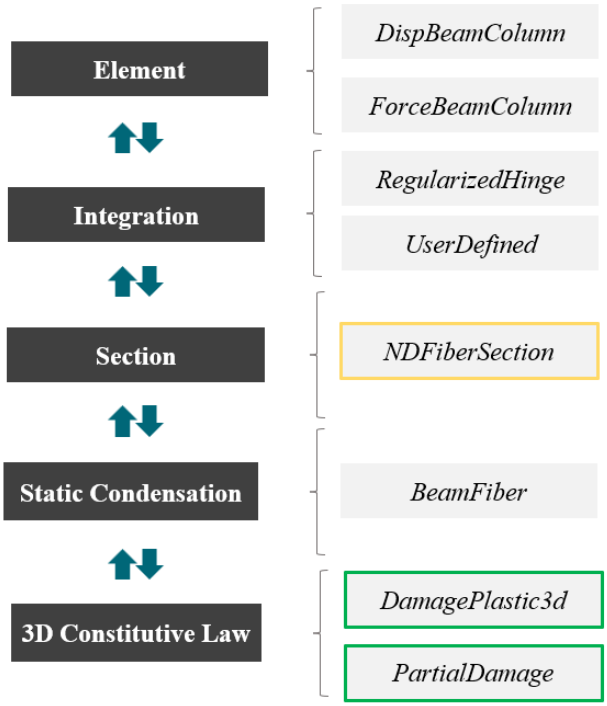

Figure 30: New Classes (green) and Modified Class (yellow) in OpenSees.

3 Application for Prestressed Concrete Beam

3.1 General

Concrete is strong in compression but has a negligible tensile strength. In reinforced concrete beams, tensile stresses lead to the beam cracking under service load, causing durability issues such as steel corrosion. The use of prestressing tendons improves the performance of structural elements, especially for bridges, allowing for greater slenderness and longer spans compared to traditional reinforced concrete bridges. Prestressing offers several advantages, including the capability to maintain an uncracked beam under higher bending moments, reducing flexural deformations, and minimizing fluctuations in state stresses due to variable loading. [92]. Prestressing can be either 'full', 'limited' or 'partial' [92], [93], [94]. In the first case, the axial stresses are always in compression, whereas in case of the 'limited prestressing', tensile stresses in the concrete are accepted up to a set value. Finally, the 'partial prestressing' allows a tension state in the concrete without restrictions.

Figure 31: A precast concrete bridge with T-beams [95]

There are two types of prestressing: pre-tensioning and post-tensioning [93], [94]. In pre-tensioning, tendons are tensioned by jacking against an abutment or stressing bed before the concrete is placed. After the concrete has set and reached sufficient strength, the strands are released, transferring the prestressing force to the beam through the bond between the strands and the concrete. A disadvantage of this technique is the rigidity of the tendon geometry, which is typically limited to straight trajectories or, at most, includes only few deviation points.

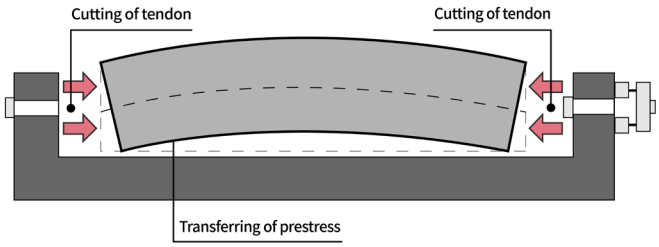

(a): Applying tension to tendons

(b): Casting of concrete

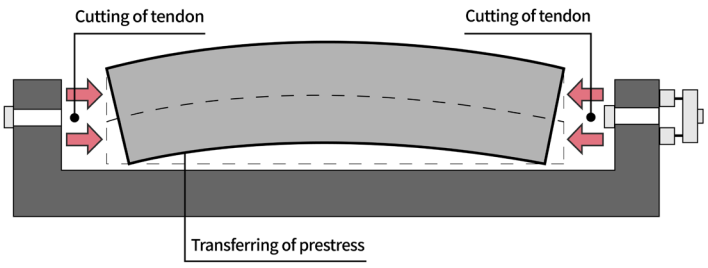

(c): Transferring of prestress

Figure 32: Stage of Pre-Tensioning [96]

In post-tensioning, the tendons are stressed with a jack on the hardened concrete. The prestressing forces are directly transferred to the beam through the tendon anchor. There are two types of post-tensioning methods: internal and external post-tensioning. The internal tendons are positioned within ducts into concrete, while the external tendons are placed in ducts outside of the concrete section [93], [94]. One of the advantages of post-tensioning is the possibility to adopt curved geometry

for tendons to improve the efficiency of the prestressing effect in the structural element. Post-tensioning with internal tendons can be categorized as bonded and unbonded. In the first case, the ducts are filled with grout after the prestressing of tendons to ensure the adherence of the steel to the concrete, and also to protect the cables from corrosion. In this case, the assumption of plane sections remains valid, as in the case of pre-tensioning. On the other hand, in unbonded post-tensioning, the bond between steel and the surrounding concrete is not guaranteed, thus the assumption of strain compatibility along the beam section is no longer valid.

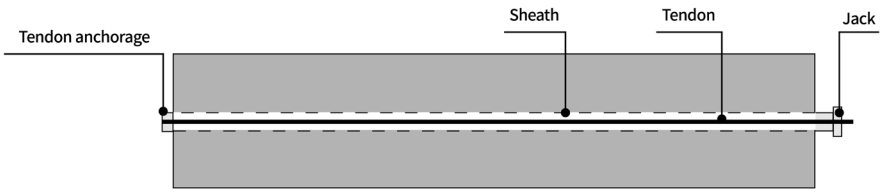

(a): Casting of concrete

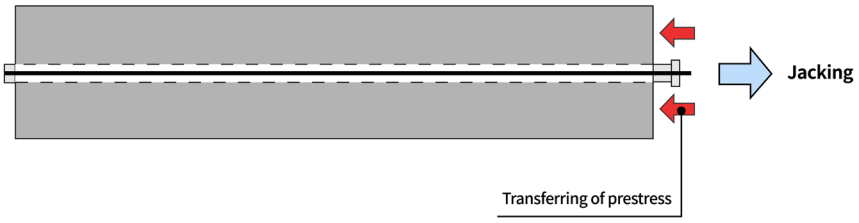

(b): Tensioning and anchoring of tendon

Figure 33: Stages of Post-Tensioning [96]

In finite element analysis, prestressing tendons can be modelled using different approaches [50], [97]. The first method considers the prestressing tendons as equivalent loads acting on the concrete, leading to inaccurate predictions of prestressing losses. The second method models the tendon as a structural element, which contributes to the structural stiffness. This approach, which includes the interaction between the tendon and concrete, allows for accurate modelling of long-term effects. In the second approach, various models have been proposed in literature [98], [99]. These models are based on the displacement method and assume that prestressing tendons are fully bonded to the concrete. Ayoub [50] developed a beam model based on a two-field mixed formulation which accounts for bond-slip effects of tendons, including distributed interface elements with a specific bond stress-slip law. The formulation requires a finer discretization of the beam, increasing the computational

effort of the analysis. In [81], [100], the modelling of prestressing effect is introduced at fiber-level as initial strain in force-based elements. This approach also includes the possibility to consider the tension losses in construction stage analysis. However, its main drawback is the lack of consideration for prestressing losses due to bond-slip. Moreover, for complex cable geometries, a considerable increase of number of integration points is necessary to ensure an accurate description of the cables.

In this chapter, an overview of the two main approaches to model the prestressing tendons in nonlinear analysis is presented. In Section 3.3, the prestressing losses are briefly described, with a special focus on the elastic shortening. Section 3.4 presents two applications of the adopted modelling approach. The first shows a comparison between the prestressed concrete fiber element model and the models available in *MIDAS GEN* and *Midas FEA NX*. Finally, the second application compares the numerical results with the experimental results conducted by Choi [101].

3.2 Modelling Approach for Tendons

For each tendon, the value of the initial tension $N_0(x,t)$ depends on the position x of the considered section and time t, to account for long-term prestressing losses. The prestressing stress in the steel fibers is equal to:

$$\sigma_0(x,t) = \frac{N_0(x,t)}{A_p} \tag{61}$$

where A_p is the effective area of steel tendons. The relative initial prestressing strain is equal to:

$$\varepsilon_0(x,t) = \frac{\sigma_0(x,t)}{E_p} \tag{62}$$

being E_p the Young's modulus of steel tendons. There are two main approaches to evaluate the effect of prestressing tendons in nonlinear analyses of prestressed reinforced concrete structures:

- **Approach 1 - Prestressing as initial steel fiber strain**: this approach involves considering prestressing effect as an initial strain in the steel fibers. The fiber stress is determined from the total strain, which is the sum of the

initial prestressing strain and the strain increment as resistant effect of the external load applied to the beam. The constitutive law should not be modified in this case, as shown in Figure 34 (a).

- **Approach 2 - Prestressing as external load**: in this method, the precompression force is considered as an external force acting on the beam element. Following the classical beam formulation, the tendons are modelled similarly to reinforcement. However, the tendon fibers necessitate a modification of the constitutive law by shifting its origin to the prestressing stress-strain point, as illustrated in Figure 34 (b).

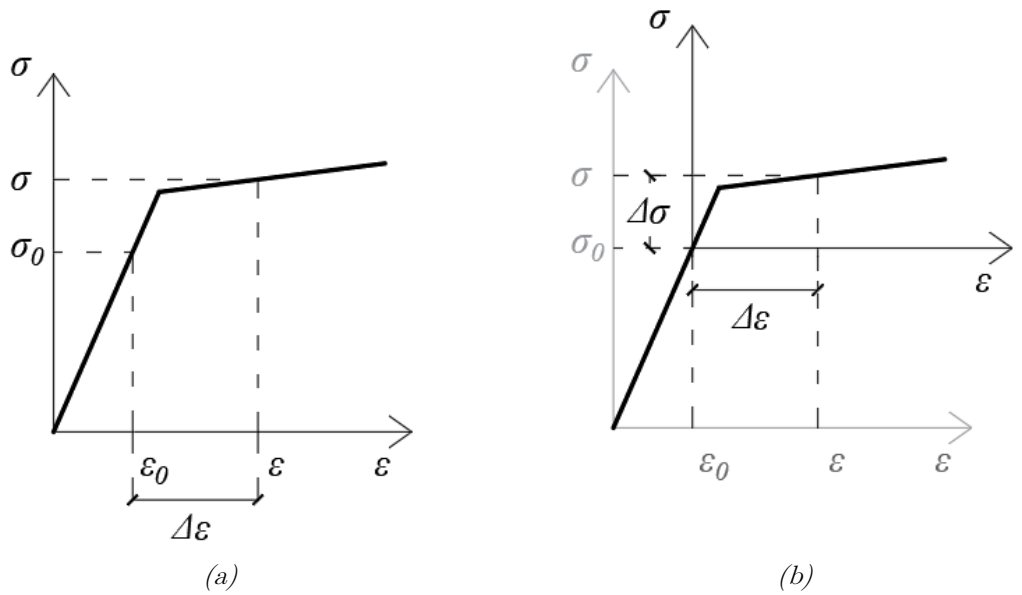

(a) *(b)*

Figure 34: Constitutive law of prestressing steel: in case Approach 1 (a) and Approach 2 (b)

In this work, the precompression is modelled in fiber beam element following the approach 1, according to [81], [100]. The fiber strains $\boldsymbol{\varepsilon}_f(x, y, z)$, defined in Chapter 2, are related to the generalized section strain vector $\boldsymbol{\varepsilon}_s(x)$ through the geometric transformation matrix $\mathbf{l}_s(y, z)$. The effect of the prestressing load is introduced as an initial fiber strain, as follows [81]:

$$\boldsymbol{\varepsilon}_f(x, y, z) = \boldsymbol{\varepsilon}_p(x, y, z) = \mathbf{l}_s(y, z)\boldsymbol{\varepsilon}_s(x) + \boldsymbol{\varepsilon}_0(x, y, z) \tag{63}$$

where $\boldsymbol{\varepsilon}_p(x,y,z)$ indicates the strain vector of prestressing tendon fiber; $\boldsymbol{\varepsilon}_0(x,y,z)$ is the initial prestressing vector, composed only by the initial axial strain of tendon ε_0. The explicit form of equation (63) is as follows:

$$\begin{bmatrix} \varepsilon_1(x,y,z) \\ \gamma_{12}(x,y,z) \\ \gamma_{13}(x,y,z) \end{bmatrix} = \begin{bmatrix} 1 & -y & 0 & 0 & z & 0 \\ 0 & 0 & 1 & -z & 0 & 0 \\ 0 & 0 & 0 & y & 0 & 1 \end{bmatrix} \begin{bmatrix} \varepsilon_G(x) \\ \chi_z(x) \\ \gamma_y(x) \\ \chi_x(x) \\ \chi_y(x) \\ \gamma_z(x) \end{bmatrix} + \begin{bmatrix} \varepsilon_0 \\ 0 \\ 0 \end{bmatrix} \tag{64}$$

In prestressed concrete beams, the cables are often characterized by a variable geometry along the beam axis. To account for the tendon inclination, the model proposed in [81] is adopted. In particular, this approach projects the fiber strain vector, which is oriented in the reference system *x*, *y*, *z* into the tendon direction. The rotation matrix is defined as:

$$\mathbf{R} = \begin{bmatrix} \cos\vartheta & 0 & -\sin\vartheta \\ -\sin\vartheta & \cos\psi & -\cos\vartheta\sin\psi \\ \cos\psi\sin\vartheta & \sin\psi & \cos\vartheta\cos\psi \end{bmatrix} \tag{65}$$

where ϑ and ψ are the inclinations with respect to the *x*-axis and *y*-axis, as illustrated in Figure 35.

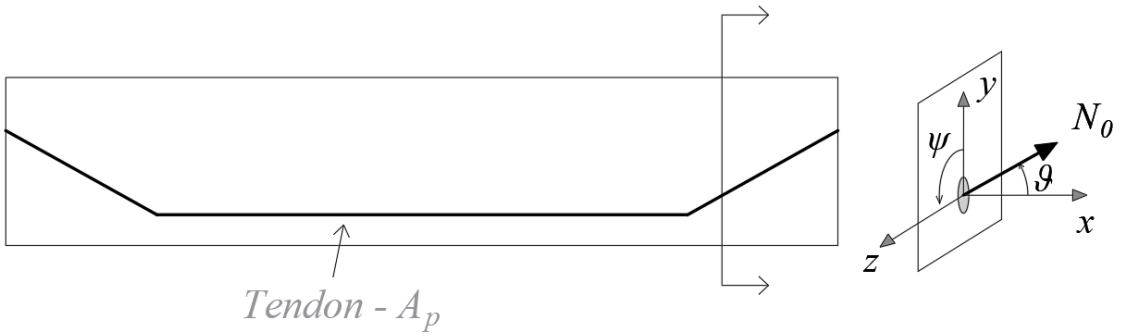

Figure 35: Variable geometry of tendons: angles between tendon and beam axes.

The section compatibility matrix in the tendon direction is given by:

$$\breve{\mathbf{l}}_s(y,z) = \mathbf{R}\ \mathbf{l}_s(y,z) \tag{66}$$

Finally, the generalized version of equation (63), which accounts for any geometry of the tendon along the beam, is equal to:

$$\boldsymbol{\varepsilon}_p(x,y,z) = \check{\mathbf{l}}_s(y,z)\boldsymbol{\varepsilon}_s(x) + \boldsymbol{\varepsilon}_0(x,y,z) \tag{67}$$

As discussed in Section 2.3, the fiber stresses are calculated through the tendon steel constitutive law, as follows:

$$\boldsymbol{\sigma}_p(x,y,z) = \mathbf{k}_p(x,y,z)\ \boldsymbol{\varepsilon}_p(x,y,z) \tag{68}$$

where $\mathbf{k}_p(x,y,z)$ is the stiffness matrix of the steel fibers.

A scheme of the fiber beam element, considering the prestressing tendon, is shown in Figure 36:

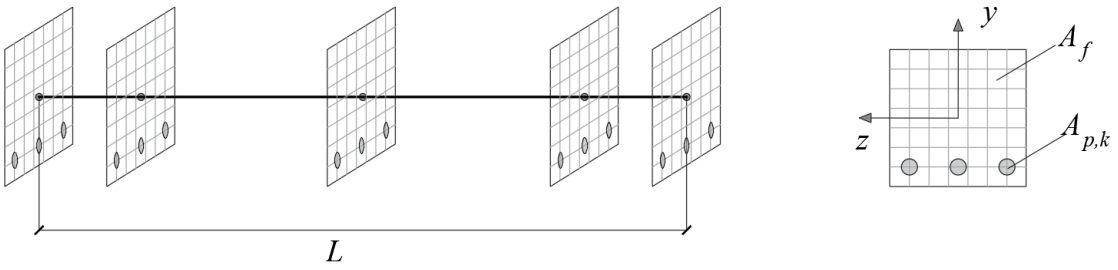

Figure 36: Prestressed concrete fiber beam element.

The generalized section stress vector is obtained with the following equation:

$$\boldsymbol{\sigma}_s(x) = \int_{A_f} \mathbf{l}_{\mathrm{s}}^T(y,z)\boldsymbol{\sigma}_f(x,y,z)dA_f + \sum_{k=1}^{n_p} \check{\mathbf{l}}_{s,k}^T(y,z)\boldsymbol{\sigma}_{p,k}(x,y,z)A_{p,k} \tag{69}$$

being n_p is the number of tendons in the prestressed beam.

Adopting the approach 1, which introduces precompression as fiber initial strain, the beam element deforms according to the plane sections assumption. Since the external loads associated with prestressing are zero, unlike approach 2, the stress diagram along the beam results null.

In finite element fiber beam models, the tendon position is considered constant along the length of the integration point. Therefore, in case of variable cable geometry (especially in case of post-tension tendons) along the beam, the model accuracy depends on the number of integration points adopted. Specifically, as the number of integration points increases, the tendon geometry is more finely discretized, enhancing the accuracy of the analysis. A detailed study concerning the influence of integration points for different shapes of the tendons is proposed in [81].

3.3 Prestress Losses

Tension losses of tendons influence the structural response of prestressed concrete beams. As known, different construction stages and time-dependent material properties alter the distribution of section stresses and internal forces within the prestressed element. Prestress losses are generally classified into two main types: instantaneous losses occurring at the time of tendon release, and time-dependent losses that occur after the release. The former mainly includes anchorage slip, friction between tendons and sheaths, and elastic shortening of the concrete. Long-term losses comprise creep and shrinkage in concrete, and relaxation of tendons. The prestress reductions are affected by various factors, notably the method of tensioning [102]:

- Pre-tensioning: before tensioning, the prestress losses are due to shrinkage and tendon relaxation, while after tensioning, they include elastic shortening, creep, shrinkage and tendon relaxation.

- Post-tensioning: the tension losses are mainly caused by the frictions between tendons and sheaths, anchorage slip, creep, shrinkage and tendon relaxation.

The application of prestressing force in a concrete member results in a state of compression in concrete, leading to the consequent shortening of the beam. Due to the adherence between the tendon and concrete, in cases of pre-tensioning or bonded post-tensioning, the tendon also undergoes shortening, resulting in a decrease of tension stresses. This phenomenon, known as elastic shortening, exhibits different characteristics between pre-tensioning and post-tensioning methods. Specifically, in pre-tensioning, an instantaneous elastic shortening of the beams occurs following the release of the tendon. As a result, the prestressing force N_0 on the

concrete beam, is less than the initial jacking tension force N_J. Instead, in post-tensioning, the prestressing force is directly applied to the concrete beam and the tension force in the tendon is measured after the shortening has occurred [102]. Consequently, unlike in pre-tensioning, there is no initial loss of tension due to elastic shortening in the post-tensioning method. However, in case of a group of tendons progressively tensioned, it is necessary to account for the loss of pretension related to the tensioning of the subsequent tendon.

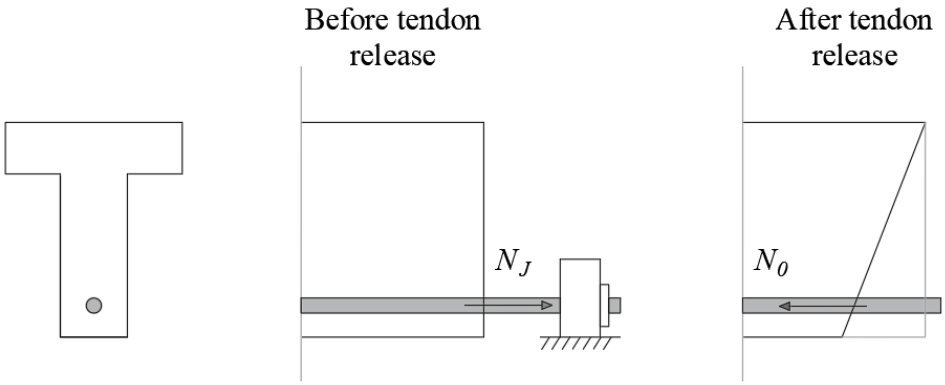

Figure 37: Elastic shortening in pre-tensioned beam [102]

Several studies have introduced prestress losses in fiber beam model [81], [100]. In Doty [100], the time-dependent phenomena have been included in the fiber beam element to consider different construction stages in segmental prestressed concrete bridges. Creep, shrinkage and relaxation are modelled as time-dependent strains in concrete and steel fibers, respectively. In [81], the fiber strain is defined as follows:

$$\varepsilon_p(x,y,z,t) = \mathbf{l}_s(y,z)\varepsilon_s(x) + \varepsilon_0(x,y,z) + \varepsilon_d(x,y,z,t) \tag{70}$$

where $\varepsilon_d(x,y,z,t)$ is the time-dependent strain which represents the following phenomena:

- Creep and Shrinkage in concrete fiber: these phenomena are introduced through the application of positive strains to the concrete fibers. Creep leads to tension in the concrete fibers and compression in the steel, while the shrinkage involves the concrete fibers in a compressed state, decreasing the compression in proportion to the stress applied.

- Tendon Relaxation: is modelled using negative strains $\varepsilon_d(x, y, z, t)$ imposed on the tendon fibers, leading to a decrease of cable pretension.

In this study, only instantaneous tension losses are considered, such as elastic shortening, in the case of pre-tensioned tendons, and steel relaxation. The first is directly calculated by imposing section compatibility, while the second is accounted for by reducing the initial fiber strain. The effects of creep and shrinkage are disregarded as they are beyond the scope of this work.

3.4 Validation

To validate the model described in the previous section, two application cases of the prestressed fiber beam element are presented. The first case examines the elastic phase, comparing the results obtained with the described model in *OpenSees* with those from *MIDAS GEN* and *MIDAS FEA NX* models. The second case focuses on validating the model in case of nonlinear analysis. Specifically, it involves comparing the numerical results of the proposed model with experimental results conducted by Choi [101].

3.4.1 Numerical application I

An example of a prestressed beam was modelled using both the described model in *OpenSees* and the existing models available in *MIDAS GEN* and *MIDAS FEA NX* software. The span length is 30 meters, and the geometry of the section is illustrated in Figure 38. The applied constraints correspond to those of a simply supported beam. The beam is composed of C40/50 concrete and an equivalent steel tendon with a tensile strength of 1860 N/mm^2. The initial stress applied to the tendon is σ_0 = 1488 MPa and the materials are assumed linear elastic. The aim of this example is to compare different approaches to modelling precompression and to validate the model previously described. For this purpose, this study compares the distributions of stresses along the midspan cross section, considering the contribution of precompression and the self-weight of the beam. For simplicity, a tendon with a constant position along the beam length is assumed.

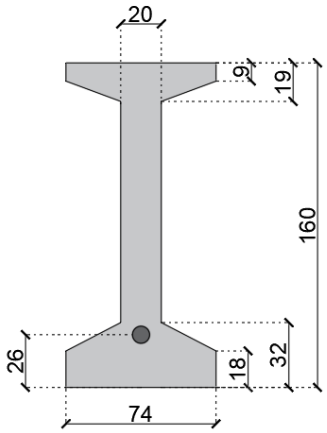

Figure 38: Section geometry of the example prestressed beam.

The prestressed concrete beam was modelled using the *STKO* pre-processor. A force-based beam element was adopted, employing the Gauss-Lobatto integration method. The beam section was discretized using the *Fiber Section Editor* in *STKO*, as illustrated in Figure 39. As previously mentioned, the fiber materials for concrete and steel were assumed linear elastic. An initial strain equal to $\varepsilon_0 = \sigma_0/E_p = 0.007440$ was applied to the steel fibers. First, only the precompression was applied. Subsequently, the self-weight load was applied to the beam, and through the superposition of effects, the final stress/strain state of sections was determined. In this example, precompression losses were neglected, except for the elastic shortening, which was directly evaluated due to the imposed section compatibility.

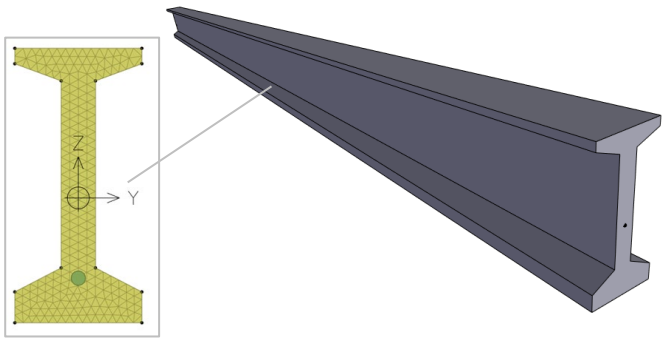

Figure 39: Prestressed concrete beam element model: view in STKO pre-processor.

Figure 40 (a) and (b) illustrate the distribution of concrete strains under the condition of only precompression and for the combined condition of precompression and self-weight. In the first case, the steel stress value results equal to 1357 MPa,

which is lower than σ_0. Similarly, the initial strain value of steel fiber, equal to 0.0068, is lower than the applied ε_0. As discussed above, the reason for this tension loss is related to the elastic shortening, which is intrinsically considered in the formulation. In particular, the application of prestressing causes the deformation of the beam. Consequently, for the section compatibility defined in Eq. (63), the reduction of the steel strain occurs. Figure 41 provides a detailed description of the elastic shortening. Specifically, ε_{comp} represents the steel strain related to the section compatibility; thus it is the first component of the vector $\mathbf{l}_s\boldsymbol{\varepsilon}_s$.

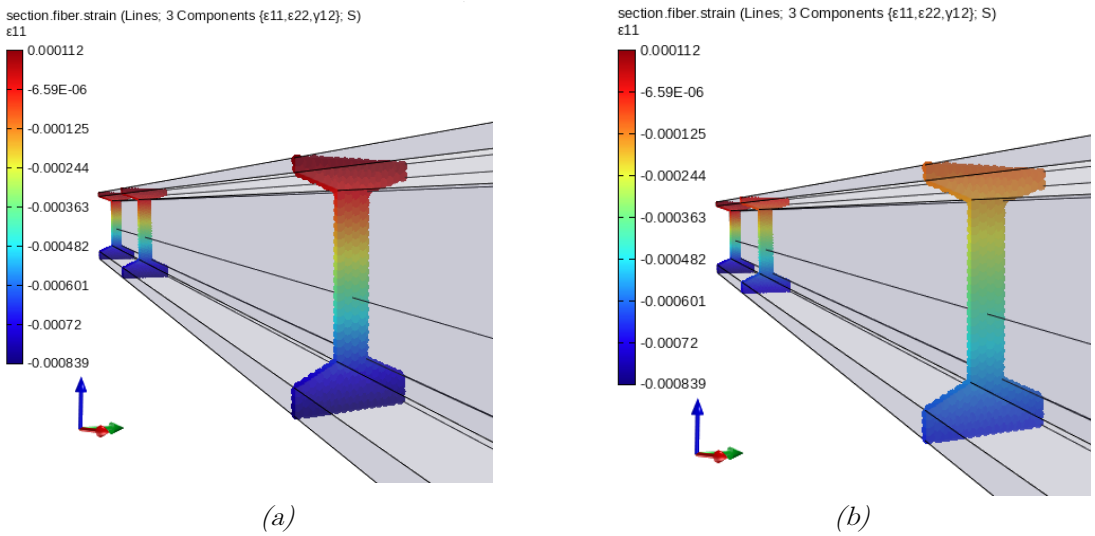

(a) *(b)*

Figure 40: Concrete strains: for precompression (a) and for the combined condition of precompression and self-weight (b).

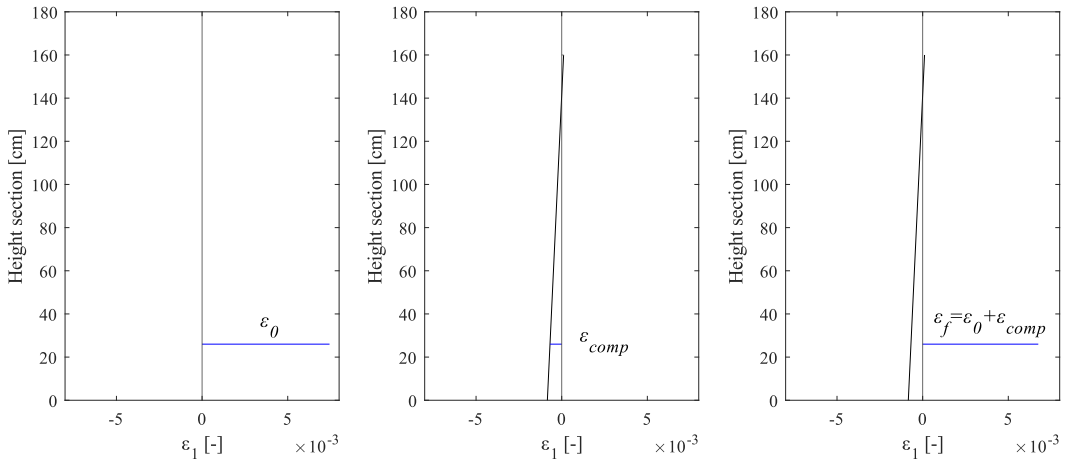

(a) *(b)* *(c)*

Figure 41: Elastic shortening: (a) applied prestressing strain in steel, (b) concrete strains along prestressed beam section and relative steel strain for section compatibility and (c) resulting strain of the steel fiber due to elastic shortening.

Figure 42 and Figure 43 show the beam modelled in *MIDAS GEN* [103] and *MIDAS FEA NX* [104], respectively. The modelling approaches for prestressed concrete beams are significantly different compared to the formulation described in Section 3.2. *MIDAS GEN* models the prestressing tendons as equivalent force, while the stiffness of tendons is included in the calculation of sectional characteristics. Specifically, the beam elements are divided into four segments, and for each of these, the equivalent prestressing load is evaluated assuming a linear geometry of tendons [102]. Moreover, in this software, the fiber sections can be defined specifically to include the nonlinear behaviour of materials.

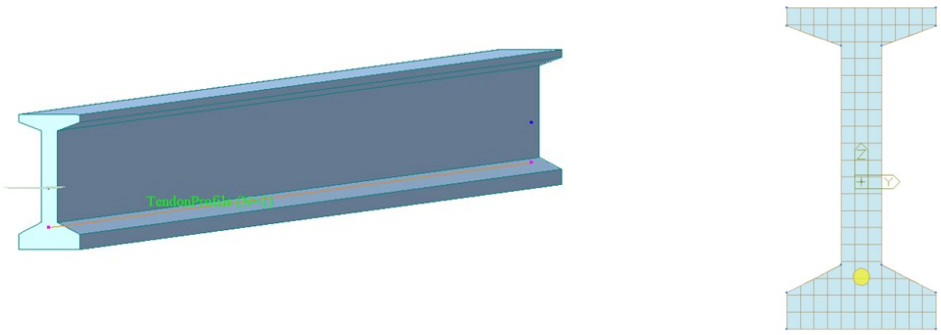

(a) *(b)*

Figure 42: MIDAS GEN: Prestressed concrete beam element (a) and fiber section (b).

MIDAS FEA NX is a finite element software developed for advanced nonlinear and detailed analysis for civil engineering applications. In this case, the beam was modelled using 3D finite elements, as illustrated in Figure 43 (a). The tendons are included in the FEM model as embedded trusses, shown in Figure 38 (b). This approach provides enhanced accuracy of the analysis in modelling the tendons geometry, however significantly increases the computational effort.

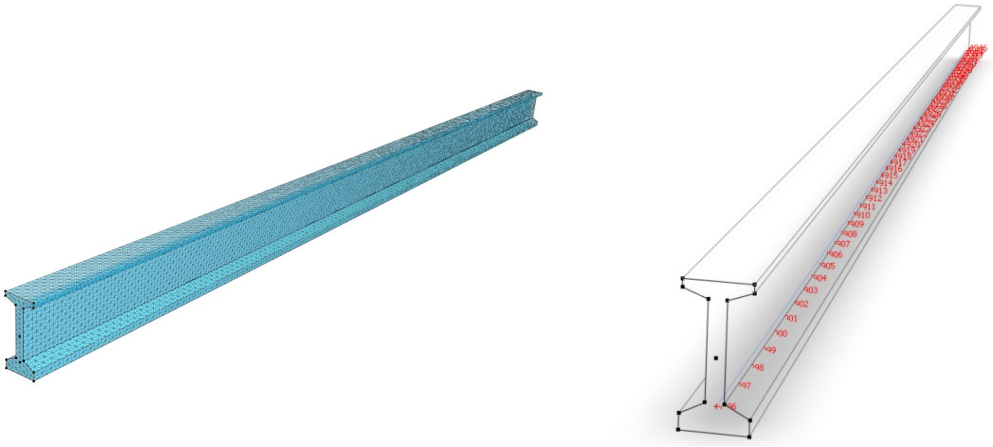

(a) *(b)*

Figure 43: MIDAS FEA NX 3D finite elements for concrete (a) and embedded trusses for steel tendons(b).

In *MIDAS GEN*, since precompression is treated as an equivalent external load, in case of the application of prestressing force, generalized section stress diagrams are visible in analysis outputs, as illustrated for axial stress N in Figure 44.

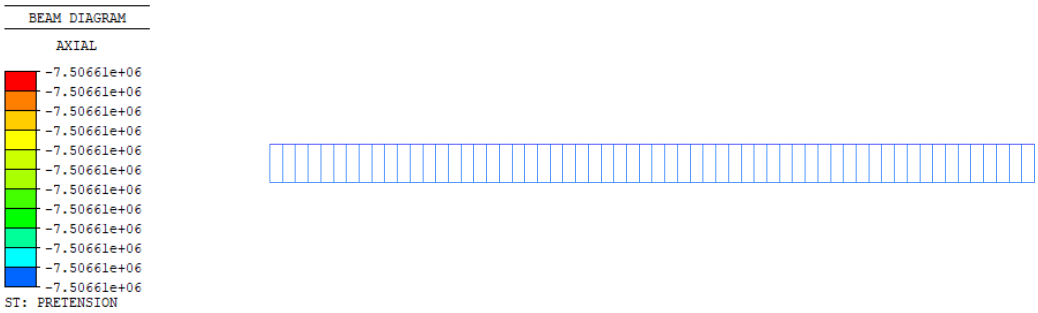

Figure 44: MIDAS GEN: Axial Stress for prestressing load.

The following figures show different outputs in *MIDAS FEA NX*. Figure 45 illustrates the axial force of tendons under the condition of only precompression. This software also accounts for elastic shortening, meaning the results consider the tension reduction associated with this phenomenon. Since the beam is modelled with 3D finite beam elements, it does not yield generalized stress diagrams commonly used in practice, but the stresses of 3D elements, as shown in Figure 46. Therefore, to calculate the bending moment or axial force of the beam, it is necessary to integrate the stresses along the section of interest.

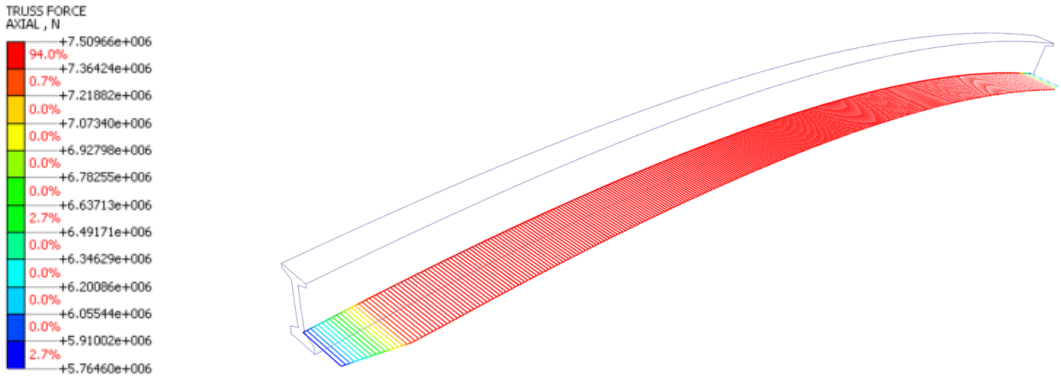

Figure 45: MIDAS FEA NX: Axial force in trusses for prestressing load.

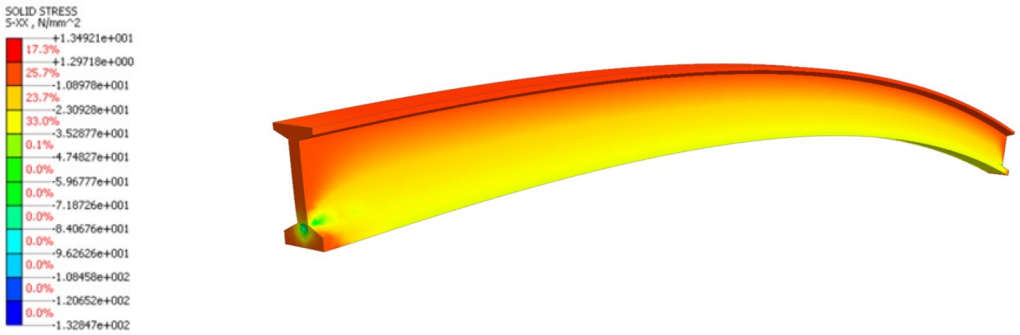

Figure 46: MIDAS FEA NX: stress in 3D elements for prestressing load.

Figure 47 (a) shows concrete stresses along the midspan section for the effect of precompression, while Figure 47 (b) for the condition of precompression combined with self-weight. Comparing the three different models, it can be observed that the results of the proposed model align with those from the *MIDAS FEA NX* model. However, it can be noted a slight difference in the curvature obtained in *MIDAS GEN*.

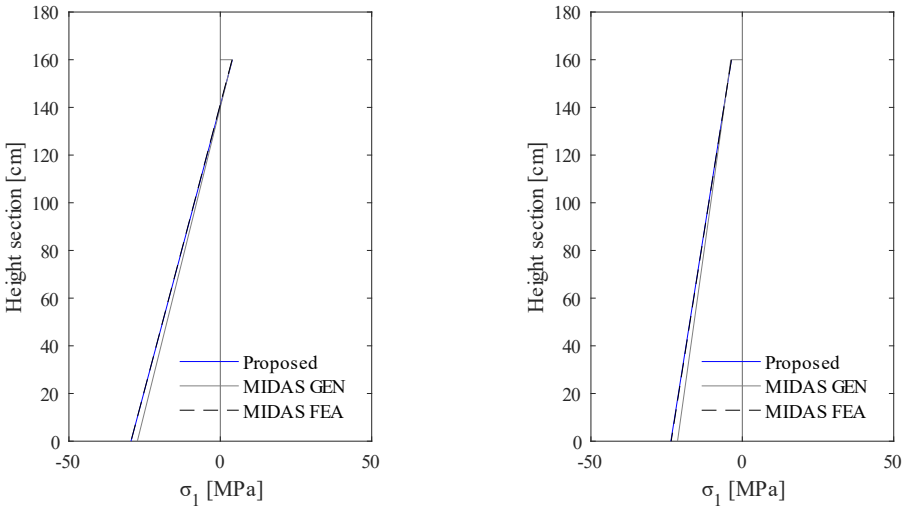

Figure 47: Concrete stress along the midspan section for the effect of precompression (a) and for the condition of precompression combined with self-weight (b).

In conclusion, the approach described in Section 3.2, which includes precompression as initial steel fiber deformation, accurately models the prestressing force, incorporating the elastic shortening in the case of pre-tensioning. However, attention is required in post-tensioning cases, as the tendon tension force is measured after the elastic-shortening.

3.4.2 Numerical application II

In this section, an application at the beam level of the prestressed finite element is shown, and the results of the nonlinear analyses are compared with the experimental results conducted by Choi [101], [105]. The purpose of the experiment was to analyse the flexural behaviour of High Strength Concrete (HSC) prestressed girders, which are commonly used in bridge construction. Nine prestressed AASHTO Type II girders, with three different concrete strengths and three configurations of slab, were tested under static loading conditions with a four-point loading test. The strands were tensioned to the 75% of their ultimate strength and the prestress losses were measured by internal strain gauges.

Figure 48: Test set-up for girder without deck with lateral frame [101].

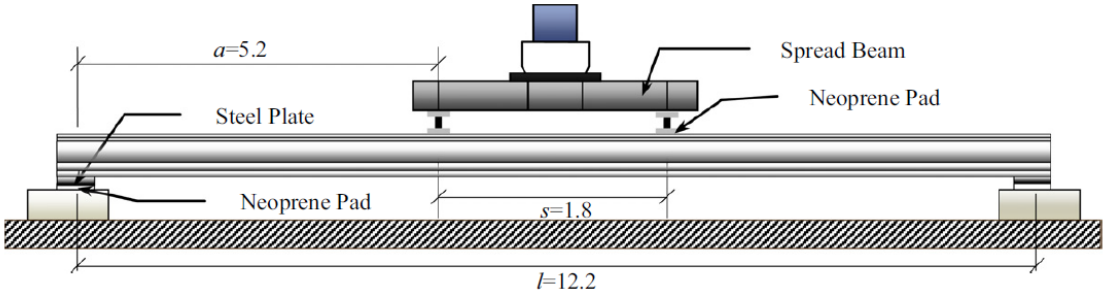

Figure 49: Scheme of the test set-up [106]

To validate the proposed model, the experimental test conducted on the specimen 10PS-N [101], [105], characterized by the absence of the slab and the concrete strength equal to 69 MPa, was modelled through *OpenSees* software as solver and *STKO* as pre- and post-processor. The specimen was divided into 4 elements to apply the vertical load in two nodes located about 90 cm from the midspan. To simulate the experimental test, the constraint conditions were represented by a simply supported beam. Figure 50 shows the model of the specimen visualized in *STKO*.

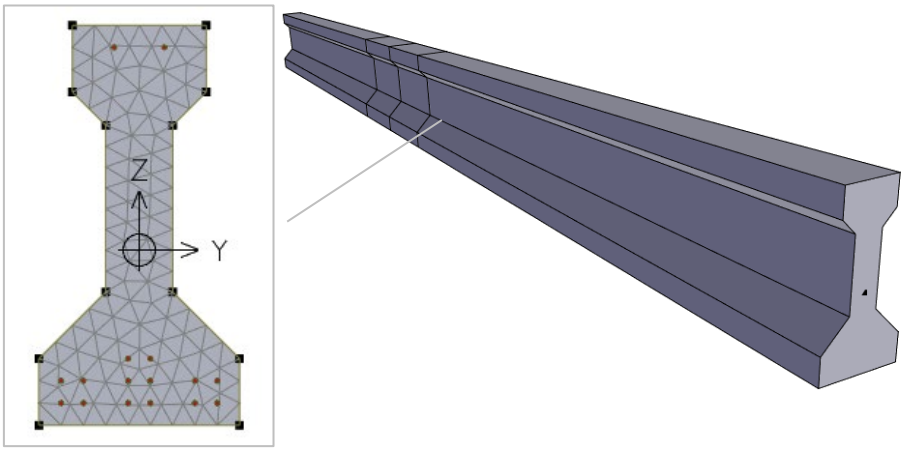

Figure 50: Test specimen model in STKO [106].

The damage-plastic constitutive law was assigned to the concrete fibers. The parameters, shown in Table 11, were calibrated to obtain the best fit with the experimental results deduced by material tests, as illustrated in Figure 51 (a). Given the brittle nature of HSC concrete, a damage constitutive law was assumed for concrete fibers. Instead, a plastic behaviour was considered for steel. In addition, a numerical model with uniaxial constitutive laws available in *OpenSees* was considered. Concrete was modelled using *Concrete02*, and steel using *UniaxialJ2Plasticity*, which were properly calibrated, as shown in Figure 51 (a) and (b).

E	ν	Y_{0c}	a_c	b_c	Y_{0t}	a_t	b_t	κ
[MPa]	[-]	[-]	[-]	[-]	[-]	[-]	[-]	[-]
35220	0.2	1.65e-03	0.05	4.3e-03	2e-05	0.8	2.5e-04	1

Table 11: Concrete material parameters

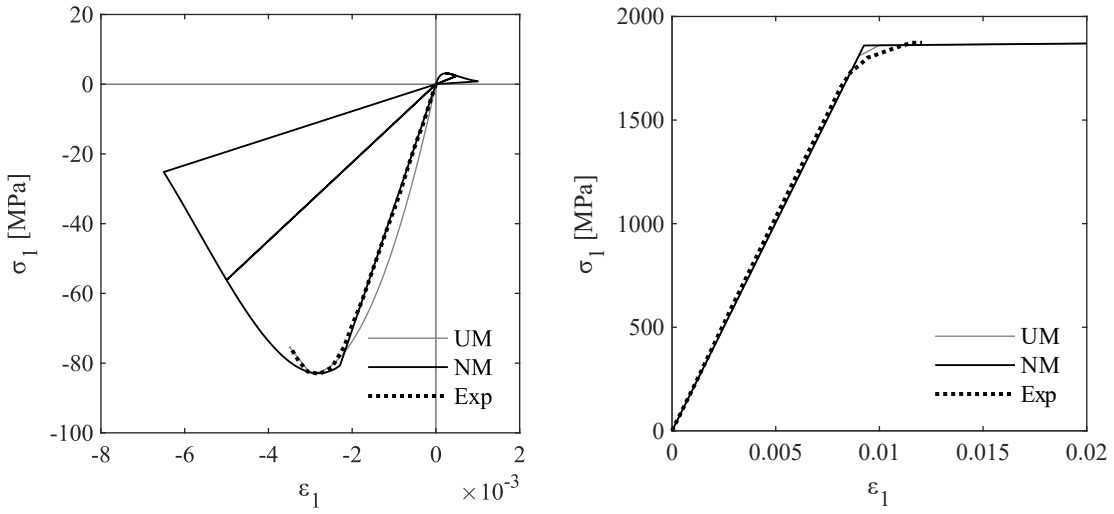

(a) *(b)*

Figure 51: Constitutive law of concrete (a) and steel fibers (b): Existing Uniaxial Material (UM), Damage-plastic Model (NM) and Experimental curve (Exp).

Figure 52 illustrates force-displacement curves, comparing the experimental response with numerical results obtained using the proposed three-dimensional material (NM) and the existing uniaxial material (UM). The results show a good agreement between the curves both in the concrete cracking phase and the yield phase. Instead, the ultimate displacement is highest in the numerical results, as the concrete in compression reaches an ultimate deformation almost equal to 0.4% while in the experimental test the failure is obtained for a value of about 0.3%. Figure 53 shows the sudden beam failure followed by the buckling of prestressing strands in the compression zone.

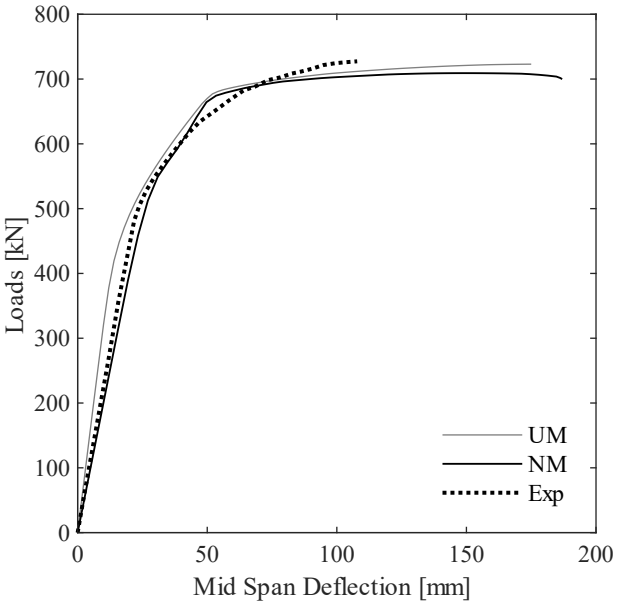

Figure 52: Force-displacement curve: Existing Uniaxial Material (UM), Damage-Plastic Model (NM) and Experimental curve (Exp).

Figure 53: Typical failure modes for the AASHTO girder without deck [105].

4 Vibration-Based Monitoring

4.1 General

Several structural monitoring techniques have been developed for the control and management of existing bridges. Visual inspections allow for the identification and quantification of visible damage, such as corrosion, cracks or spalling. In common practice, a qualified inspector assesses the damage state of structures through visual inspections, yet this method, while standard, tends to be time-consuming and susceptible to human error. Recent years have seen the emergence of new technologies based on the use of autonomous platforms and image processing algorithms [107], designed to enhance and support this evaluation process. One of the limitations of the vision-based techniques is that the correlation between visual observations and structural reliability is often challenging [108]. For structural assessment of the global condition, Vibration-Based Monitoring (VBM) are more suitable to detect features indicative of changes in structural behaviour. These techniques identify the structural damage through the continuous monitoring of the characteristic dynamic parameters of the structure [109]. From the structural vibrational response, such as acceleration or velocity records, it is possible to identify dynamic parameters that describe the structural behaviour. The variations of these parameters are indicative of alterations in structural behaviour associated with damage of the structural components, consequently, they can be defined as indicators of damage. Various approaches have been proposed for identifying damage utilizing dynamic monitoring data, employing both time series analysis [11], [110] and the dynamic responses in the frequency domain [12], [111]. Vibration-based methods are categorized into model-based and data-driven approaches [112]:

- **Model-based approach** involves using structural identification and model updating procedures to calibrate physical models, often FE model, according to experimental measurements [13]. However, their applicability for real-time monitoring is constrained by significant computational effort related to the model updating process. The main advantage of a model-based approach is its capacity to evaluate the residual service life of a structure. This is particularly efficient when a degradation model is integrated into the FE model, facilitating a reliable estimation of the structural durability.

- **Data-driven approach** relies on developing statistical models, which involves applying *pattern recognition* to experimental data to quantify the damage state of the structure. Based on the available data, two types of learning algorithms can be distinguished: *supervised* or *unsupervised learning algorithms* [14]. *Supervised learning* algorithm is used when the behaviour of both the intact and damaged structure is known. On the other hand, *unsupervised learning* is applied when only the behaviour of the intact structure is known. The application of *unsupervised* methods is generally confined to recognizing the presence of damage, offering the advantage of requiring only knowledge of the parameters of the undamaged structure. In contrast, *supervised* methods application allows for the localization and quantification of damage. In data-driven approach, damage features are extrapolated from the recorded response, and changes in these features are detected compared to the undamaged condition of the structure. This method is particularly advantageous for real-time monitoring. However, without an associated physical model, it does not allow for the estimation of the damage severity and the remaining life of the structure. Some examples of data-driven methods using statistical algorithms are: Artificial Neural Networks (ANNs), Genetic Algorithms and Bayesian Regression, discussed in [113].

Several research works discuss about the effects of environmental and operational conditions, such as temperature, humidity, wind and traffic intensity, in damage identification problem. In this regard, a large variety of approaches have been proposed for compensation of temperature effects [114], [115]. Further insights may be interesting for future developments of this work.

In Section 4.2 of this chapter, an introduction to the vibration-based method is provided, with a focus on the detection of structural damage through frequency variation. This is followed by an introduction of the key concepts of dynamic analysis for fiber beams. Finally, Section 4.4 presents an application of the proposed model, compared with experimental results presented in [116]. Specifically, the proposed procedure consists in performing a nonlinear analysis to induce damage, followed by a modal analysis of the structure to assess frequency variation.

4.2 Vibration-Based Damage Detection

Structural analysis problems are distinguished into two types: *direct* and *inverse*. The *direct problem*, typically used in the design of new structures, involves known actions and structural properties, while the structural response remains the unknown. Conversely, in the *inverse problem*, often used in structural health monitoring, the structural responses are known, while the structural characteristics are unknown. In the typical problem of *Structural Health Monitoring*, the structural response is given by the experimental tests, for example static or dynamic, and the unknown factor is the structural damage state. Modal models, based on the vibration-based approach, are most used in inverse problems, involving a process called *model updating* to refine the physical model using experimental data.

Due to the different challenges presented by various structures and systems, several methods have been developed for monitoring existing bridges, which are largely discussed in literature [108], [112], [117]. Rytter [118] proposed a classification of these methods based on four levels:

1) Level 1: confirming damage presence in the structure

2) Level 2: identifying the damage location

3) Level 3: quantifying the damage severity

4) Level 4: predicting the structural remaining service life

The first level simply indicates the presence of damage in a structure, instead the second level finds the specific damage locations. The third level evaluates the severity or extent of the damage, necessitating a parametric model to characterize the damage, such as crack length and stiffness reduction. The most advanced level of structural assessment involves predicting the remaining service life of a structure, but it requires a global structural model with localized models of continuum damage or fracture mechanics [117].

Vibration-based damage identification is a pivotal approach in the field of structural health monitoring [8], [9], [10], [119], [120]. This technique utilizes the vibrational characteristics of a structure to detect, locate, and assess damage. Damage or deterioration of the structural elements causes the modification of the vibration modal parameters, such as natural frequencies, mode shapes and modal damping. The vibration-based damage identification methods based on vibration features are

classified into four main groups [8]: methods based on natural frequency, mode shape, curvature mode shape, and a combination of mode shapes and frequencies. Mode shape-based and curvature mode shape-based methods typically focus on the localization of damage. Mode shape-based approaches often depend on optimization algorithms or signal processing techniques for precise damage localization, whereas curvature mode shape-based methods are generally effective for this purpose. One of the most reliable and commonly used methods for assessing structural damage involves the use of natural frequency as a diagnostic parameter. Specifically, this method examines the resonant frequencies obtained from dynamic testing results. A decrease of these frequencies can indicate a reduction of the structural stiffness, caused by the presence of damage in one or more structural components. A variation of about 5% of natural frequency is often required to distinguish it from variations caused by environmental factors. Conversely, an increase of frequencies may suggest stiffer supports [10]. The degree of natural frequency reduction depends on the damage position relative to the mode shape. Especially, a crack located at regions of high curvature for the modes leads to a significant reduction of the local bending stiffness, affecting the natural frequencies. Lower frequency vibration modes are generally regarded as effective for detecting structural damage. However, higher modes are more sensitive to local damage, but their availability in full-scale vibration tests is limited.

Various studies have indicated that in prestressed concrete structures, vibration frequencies are not particularly sensitive to the reduction of stiffness of the prestressing steel [10], [121]. Particularly, until the prestressing cable remains elastic, even in the presence of cracks, small frequency variations are observed. However, a significant reduction of frequency occurs only when prestressing wires exceed their elastic limit.

4.3 Dynamic Analysis for Fiber Beam Elements

In the context of structural engineering and particularly for beam elements under dynamic loading, the discretized equations that govern the motion are given by:

$$\mathbf{M}\ddot{\mathbf{u}} + \mathbf{C}\dot{\mathbf{u}} + \mathbf{P}^{int}(\mathbf{u}) = \mathbf{P}^{ext} \tag{71}$$

where $\ddot{\mathbf{u}}$, $\dot{\mathbf{u}}$, and $\mathbf{u}$ represent the nodal acceleration, velocity, and displacement, respectively. The global mass matrix, denoted as $\mathbf{M}$, is determined using a lumped or a consistent method. The matrix $\mathbf{C}$ indicates the global damping matrix. These global matrices are obtained by assembling the corresponding element submatrices $\mathbf{M}^e$ and $\mathbf{C}^e$ [32]. One of the most used approaches in dynamic structural analysis consists in the adoption of the Rayleigh damping. This method is based on the concept that the damping in a system can be represented as a linear combination of the mass and stiffness matrices. This is expressed as:

$$\mathbf{C}^e \ = a_1 \ \mathbf{M}^e \ + \ a_2 \ \mathbf{K}^e \tag{72}$$

being a_1 and a_2 the coefficients that determine the relative contribution of damping proportional to mass and stiffness, respectively. The main advantage of Rayleigh damping consists in its simplicity of implementation in FE models. Especially, it allows for the introduction of damping into the system without needing to define a complex viscous damping matrix.

The adoption of a *consistent mass matrix* or a *lumped mass matrix* are two distinct approaches used in computational mechanics to represent the mass distribution of a structural element. The *consistent mass matrix* reflects a more realistic distribution of mass across the entire element. In this approach, the mass matrix is typically non-diagonal and captures the inertia and dynamic properties of the element more accurately. The mass matrix of the element can be expressed in a consistent form as follows:

$$\mathbf{M}^e = \int_{\Omega^e} \mathbf{N}^T \rho \ \mathbf{N} \ d\Omega^e \tag{73}$$

where ρ is the mass density of the beam and $\mathbf{N}$ is the matrix of the shape functions. In contrast, the *lumped mass matrix* simplifies the analysis by allocating the entire mass of an element to its nodes. This results in a diagonal mass matrix, where the mass is *lumped* at the nodes rather than being distributed along the element. The diagonal components of the lumped mass matrix can be expressed as:

$$M_{jj}^{e} = \sum_{k} M_{jk}^{e} = \int_{\Omega^{e}} \rho \; N_j \; d\Omega^{e} \tag{74}$$

Although this method is less accurate compared to that adopting consistent matrix, it requires a lower computation effort. The choice between a consistent and lumped matrix depends on the specific type of analysis, the required accuracy, and the computational complexity.

In case of the displacement-based fiber beam element, the formulation of the consistent mass matrix is relatively straightforward, because the interpolating functions of the section displacements from the nodal degree of freedom are easy to obtain. In contrast, for force-based beam elements, the definition of the consistent mass matrix becomes significantly more complex [122]. Several methods were proposed in literature to determine the exact shape functions interpolating the section displacements from the nodal degrees of freedom [122], [123], [124], [125]. Molins [125] introduced a method to evaluate the exact flexibility-based consistent mass matrix by applying d'Alembert's principle. However, the drawback of this method is that it requires the computation of a triple integral over the element. De Souza [124] proposed a simpler approach based on the Unit Load method, reducing the complexity to a double integral for 2D elements. This technique was further refined and extended to 3D elements by Shen [123]. Specifically for force-based elements, the consistent element mass matrix is defined as follows:

$$\mathbf{M}^{e} = \int_{0}^{L} \mathbf{N}_{s}^{T}(\boldsymbol{x}) \; \mathbf{m}_{s}\,(\boldsymbol{x})\, \mathbf{N}_{s}\,(\boldsymbol{x})\, dx \tag{75}$$

where $\mathbf{N}_{s}$ is shape function matrix for force-based beams obtained by the virtual work equivalence [122]:

$$\mathbf{N}_s(x) = \mathbf{b}_{rs}^T(x) \left[\int_0^L \mathbf{b}_r^T(\xi) \mathbf{f}_s(\xi) \mathbf{b}_s(\xi)\, d\xi \right] \mathbf{F}^{e-1} \mathbf{a}_g + \mathbf{N}_r(x) \mathbf{a}_r \tag{76}$$

where $\mathbf{b}_{rs}(x)$ calculates the nodal reactions of the simply supported restraints for unit loads at x, instead $\mathbf{b}_r(\xi)$ computes the section stresses at ξ, which is the abscissa along the element axis. The matrix $\mathbf{N}_r(x)$ is the shape function matrix for the rigid body displacements. Finally, $\mathbf{a}_g$ is the element compatibility matrix and $\mathbf{a}_r$ is the rotation matrix from the global to local reference system.

To simulate environmental vibrations, the White Noise signal is applied to the nodes of the structural model. In this case, the equation (71) becomes:

$$\mathbf{M\ddot{u}} + \mathbf{C\dot{u}} + \mathbf{Ku} = \mathbf{h}w(\mathrm{t}) \tag{77}$$

where $\mathbf{h}$ represents the vector indicating the nodes of the model where the excitation force is applied, and $w(\mathrm{t})$ is a stochastic process of the White Noise. In particular, White Noise (WN) is a random signal characterized by the lack of periodicity over time and a constant amplitude in its entire frequency spectrum [113]. The key aspects of white noise signal include that the average value is zero and the variance function is constant. Additionally, the power spectral density of white noise is flat, signifying a uniform distribution of energy for different frequencies. In Figure 54, an example of a White Noise signal generated in MATLAB and applied to the model is shown. The terms μ_x and σ represent the mean and the standard deviation of the generated signal, respectively.

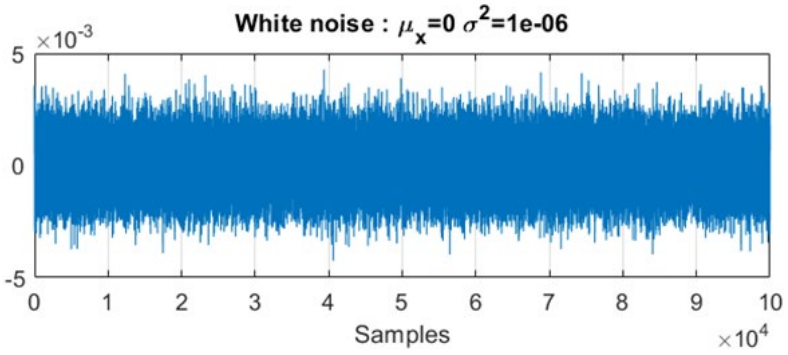

Figure 54: Example of a White Noise signal.

To assess the dynamic characteristics of the structure corresponding to its damaged state, a very low amplitude of the WN force is used. The outputs of the model, in terms of either displacements or accelerations, are then utilized for training a neural network. Additionally, the pseudo-experimental responses are analysed in the frequency domain, obtained through the application of the Fast Fourier Transform (FFT). Further details on the procedure are provided in the following chapter. Several solution algorithms for nonlinear dynamic analyses are available in *OpenSees* [89]. In this work, the Newmark method is adopted for the time integration of equation (71), utilizing coefficients γ and β, equal to 0.5 and 0.25 respectively.

For completeness, a brief overview of the linear modal analysis formulation used to evaluate the natural frequencies of the structural system is also provided. In this case, the equation (71) becomes as follows:

$$\mathbf{M}\ddot{\mathbf{u}} + \mathbf{K}\mathbf{u} = \mathbf{0} \tag{78}$$

The general solution to the previous equation can be expressed as:

$$\mathbf{u} = \overline{\mathbf{u}}\ \mathrm{e}^{\mathrm{i}\omega t} \tag{79}$$

where $\overline{\mathbf{u}}$ is a vector of the time-independent amplitudes. Substituting (79) in equation (78), the formulation of the generalized eigenproblem is expressed in eq. (80), where ω and $\overline{\mathbf{u}}$ must be determined.

$$(-\omega^2\ \mathbf{M} + K)\overline{\mathbf{u}} = \mathbf{0} \tag{80}$$

To solve the linear eigenvalue problem, the determinant of the following matrix needs to be zero:

$$|-\omega^2\ \mathbf{M} + \mathbf{K}| = 0 \tag{81}$$

The most common commercial FE software can perform linear modal analysis of the structures. When a nonlinear analysis precedes a linear modal analysis, the solution to the eigenvalue problem considers the global stiffness matrix obtained at

the last step of the nonlinear analysis. Since the current global stiffness matrix is reduced by the material damage, the frequencies derived from the modal analysis are influenced by the current damaged state of the structural system. Further insights on these aspects are provided in the following section.

4.4 Application

In this section, an application of the proposed finite element model to evaluate the frequency variation due to beam cracking is presented, and the numerical results are compared with those experimentally obtained by Cerri et al. [116]. The experimental test involved both static and dynamic tests on two reinforced concrete beams, each measuring 2.45 meters in length, with a cross-section of 100 x 150 mm^2. The beam is reinforced by two steel bars in compression and two in tension, with a total area of 151 mm^2 and 57 mm^2, respectively. The class of concrete is C30/37, and the smoothed steel bars are characterized by f_{yk} =320 MPa. Further details regarding the reinforcements and materials used are provided in [116]. In the static test, seven load-unload steps were performed. Subsequently, for each load step, a dynamic test was conducted after removing the load to assess the frequencies of the main vibration modes. The beam for the dynamic tests was hung by flexible springs to simulate the free-free condition. The resulting accelerations were transformed into the frequency domain to obtain the natural frequency in different damage phases.

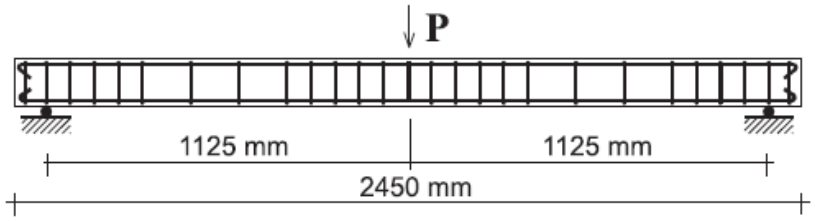

Figure 55: Experimental arrangement for Static test [116]

The experimental test was numerically modelled through *OpenSees* software as solver and *STKO* as pre- and post-processor. To simulate the experimental test, a simply supported beam with a span equal to 2.25 m was modelled. The beam was divided into two FB fiber beam elements, each 1125 mm in length. The regularization technique proposed by Addessi in [29] was adopted, which is described in detail in Section 2.5. Specifically, a length L_p equal to 0.2 L was assumed, where L is the length of the element. Initially, the self-weight was applied as a distributed load on

the beam. Subsequently a load-controlled analysis was performed by applying a vertical force at the midspan of beam, corresponding to the point of application of the experimental load. Specifically, seven cycles of loading and unloading were applied, according to the experimental test, which resulted in the cracking of the beam. The load amplitude was increased with each cycle, leading to the further spread of cracks. At the unloading point, a modal analysis was performed to assess the variations of frequencies caused by the increasing damage in the beam. In particular, the modal analysis is utilized to extract the frequency of the first mode of vibration. The percentage of frequency variation is calculated relative to the frequency measured before the application of the load, which is considered the undamaged state of reference. This method allows for an assessment of the structural integrity by quantifying the degree of frequency variation with respect to the undamaged condition, thereby providing a relation between damage and dynamic parameters.

The three-dimensional damage-plastic law implemented as a new material in *OpenSees* and described in Section 2.4 was assigned to the concrete fibers; instead, a plastic model was considered for steel. Three different constitutive models for concrete were adopted to compare their performance in simulating complex mechanical phenomena, such as damage and plasticity, for both nonlinear static and dynamic analyses. This comparison is crucial for identifying the most accurate and reliable model for predicting the structural response of damaged structural elements.

The first model adopted considers a tensile behaviour characterized only by damage. The parameters are summarized in Table 12. Figure 56 (a) and (b) shows the results of the *patch test* for a loading-unloading cycle in tension. Specifically, Figure 56 (a) illustrates the results in terms of stress-strain, while Figure 56 (b) shows the evolution of damage. As observed in the figure, the unloading branch is characterized by a reduction of stiffness, which is a direct consequence of the damage occurred during loading, as well described in Section 2.4.

E	ν	Y_{0c}	a_c	b_c	Y_{0t}	a_t	b_t	κ
[MPa]	[-]	[-]	[-]	[-]	[-]	[-]	[-]	[-]
30000	0.25	4.2e-04	0.9	2e-03	2e-05	0.65	1e-04	1

Table 12: Concrete material parameters for damage model

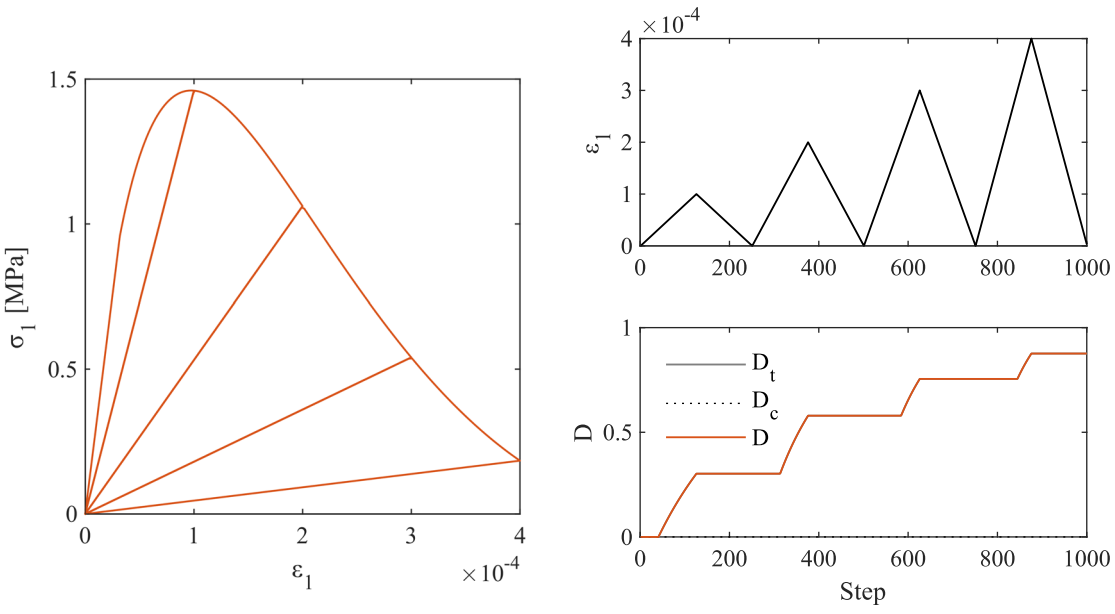

Figure 56: Damage model: strain history and damage evolution.

The results in Figure 57 show a good agreement between the curves both in the concrete cracking phase and in the yielding phase. Especially, it is observed that the model accurately captures the onset of cracking, evidenced by the reduction of stiffness occurred for a vertical load of approximately 2 kN. The stiffness in the initial cracked phase and in the post-yield phase closely matches the experimental curve. However, the numerical model predicts that the reinforcement yielding occurred at a lower displacement value compared to that observed in the experimental tests. This discrepancy may be attributed to a possible slip of the reinforcement bars during the experimental test, particularly since smoothed bars were used. The numerical model does not consider the bond-slip between the reinforcement bars and the surrounding concrete. This phenomenon, while important, falls outside the scope of this study. Regarding the unloading branch, it is observed that the model, being based on a damage formulation, fails to capture the residual displacement. This results in a lower stiffness of the unloading branch compared to the experimental data. Figure 58 shows the frequency variation of the first mode of vibration obtained from the numerical simulation, comparing it with the experimental results. It is noticeable that the model significantly overestimates the frequency variation from the initial loading steps, corresponding to the onset of the beam cracking.

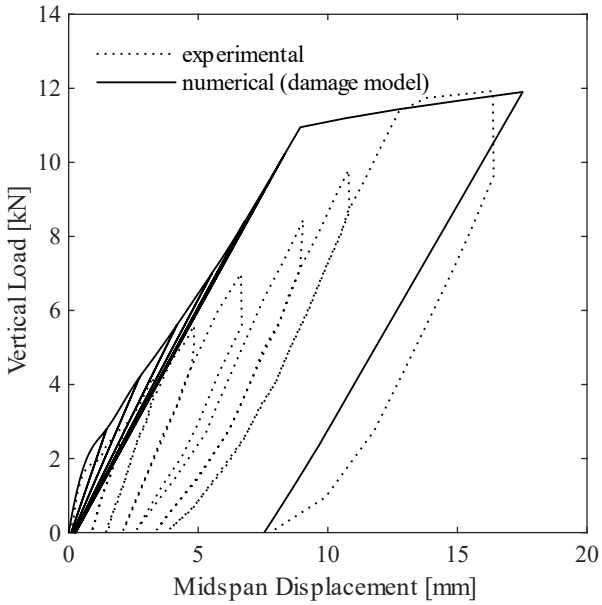

Figure 57: Nonlinear static response: damage model and experimental results.

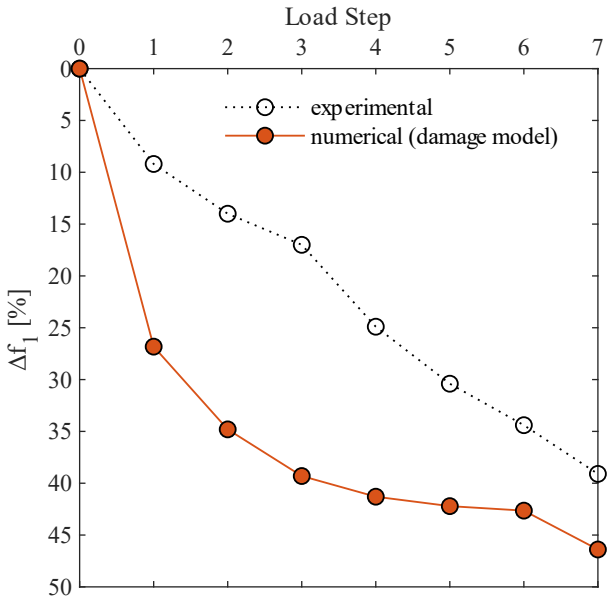

Figure 58: Frequency variation: damage model and experimental results.

The second and third constitutive law adopted in this study are based on the damage-plasticity model, described in Section 2.4. The material parameters defined for concrete fibers are detailed in Table 13. Adopting a Drucker-Prager plasticity model, the proposed constitutive law can also consider the plasticity in tension, thereby enabling to capture the plastic residual after the unloading of the beam, as shown

by experimental results. While the second model assumes the complete closure of cracks, the third model adopts a more refined approach considering the partial closure of cracks, as described in Section 2.4.4. Figure 59 illustrates a comparison of the *patch test* results using the model with complete crack closure, given by $\beta = 0$, and the model that considers the partial cracks closure with $\beta = 0.6$.

E [MPa]	ν [-]	σ_t [MPa]	H_i [MPa]	H_k [MPa]	Y_{0c} [-]
30000	0.25	1.5	0.01 E	0.01 E	4.2e-04

a_c [-]	b_c [-]	Y_{0t} [-]	a_t [-]	b_t [-]	κ [-]
0.9	2e-03	2e-05	0.9	1e-04	1

Table 13: Damage-plastic model: material parameters

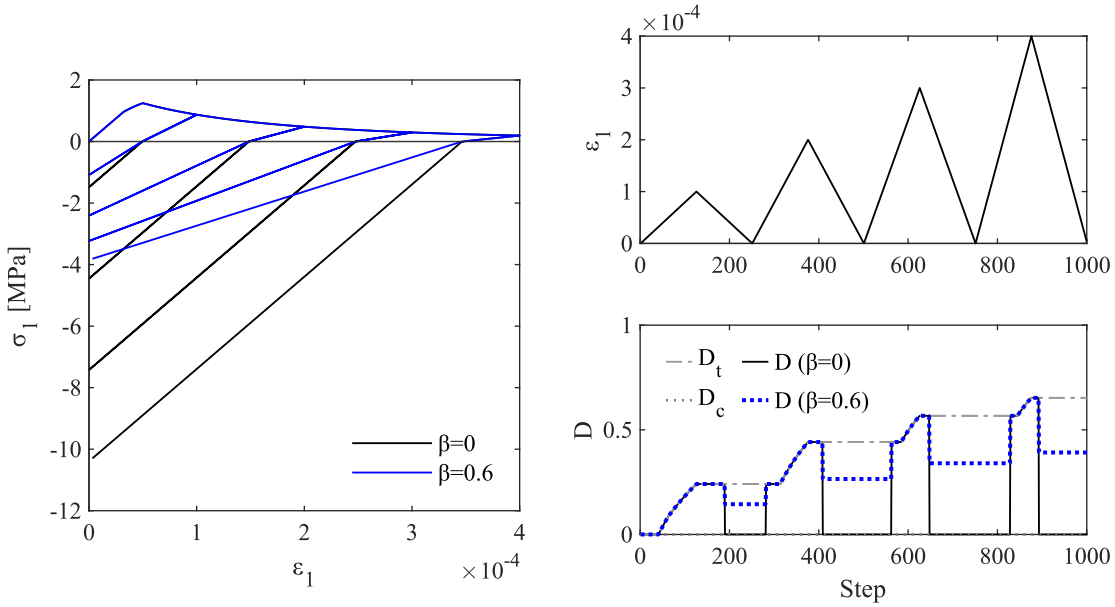

(a) *(b)*

Figure 59: Damage-plastic model, $\beta = 0$, vs Modified damage-plastic model, $\beta = 0.6$, loading and unloading cycle.

Figure 60 illustrates the uniaxial constitutive response in tensile and compression of the concrete and steel material, which were adopted in this numerical application.

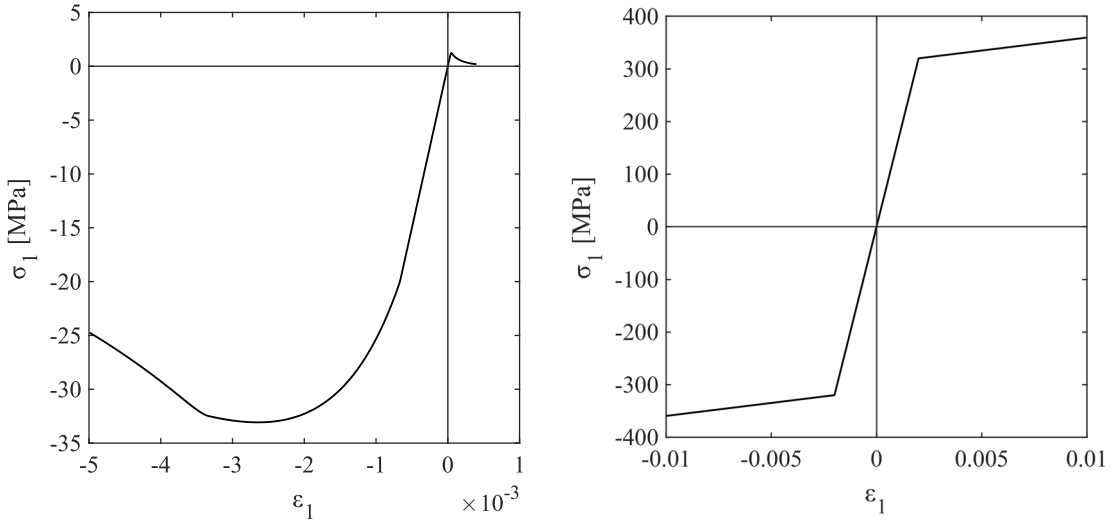

(a) *(b)*

Figure 60: Constitutive law of concrete fibers(a) and steel fibers (b).

The results of the nonlinear analysis and the frequency variation for the damage-plastic model with $\beta = 0$ are shown in Figure 61 and Figure 62. Thanks to the capability of modelling the tensile plasticity of concrete, it has been possible to capture the residual plastic displacement of the global curve during the crack diffusion phase, as shown in Figure 61. Due to the plastic residuals, the unloading phase causes compressive stresses in the concrete, as clearly visible in Figure 59. Therefore, the global stiffness of the unloading phase results significantly influenced by the compressive behaviour after the closure of cracks. In Figure 62, it can be observed that the frequency variation when $\beta = 0$ is underestimated compared to the experimental results. Adopting the modified damage-plastic model described in Section 2.4.4, it is possible to include the effects of the partial closure of cracks. Figure 63 presents the results of the nonlinear analysis using the modified model with $\beta = 0.6$. Differing from the results obtained for $\beta = 0$, the stiffness in the unloading branch more accurately aligns with the experimental results. Additionally, the results in terms of frequency variation closely match the experimental frequency variation, as illustrated in Figure 64.

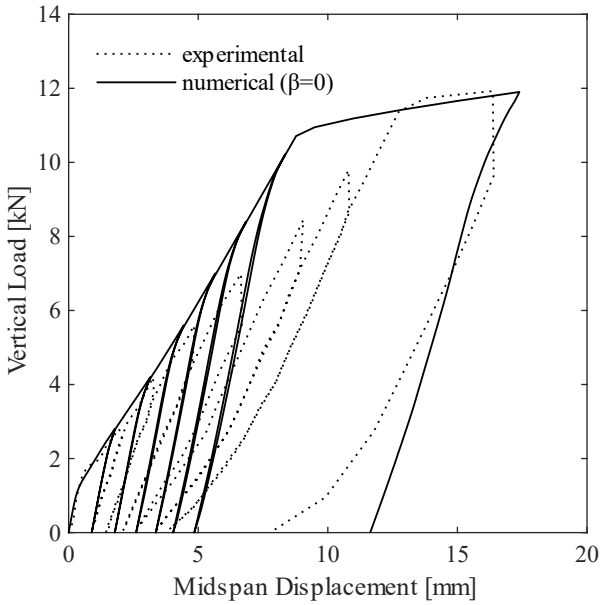

Figure 61: Nonlinear static response: damage-plastic model and experimental results.

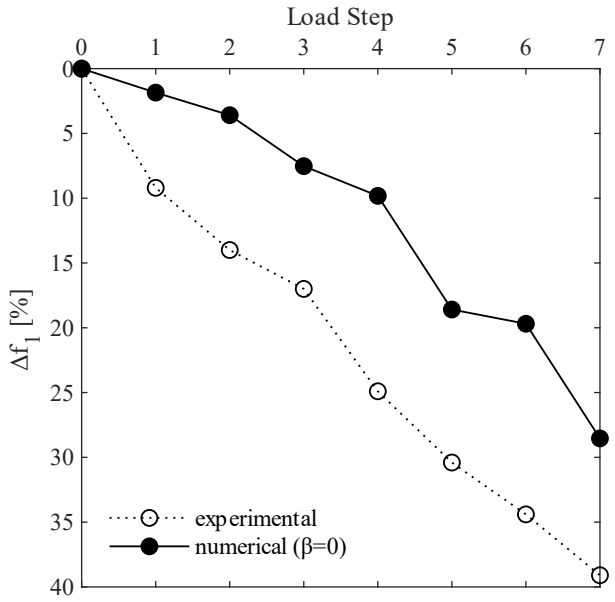

Figure 62: Frequency variation: damage-plastic model and experimental results.

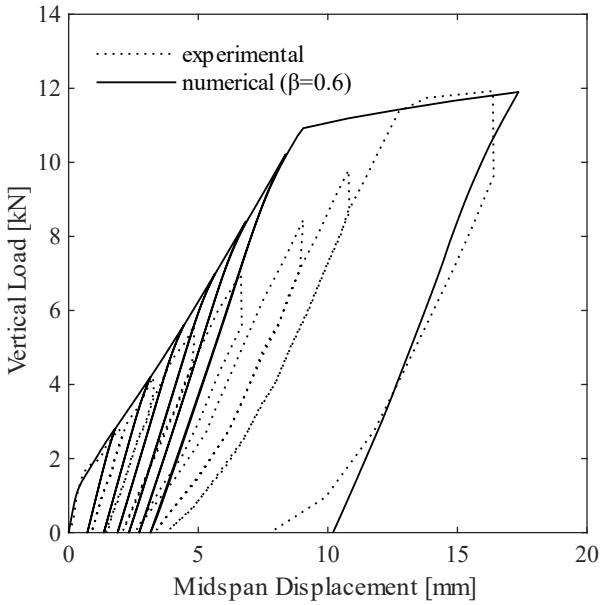

Figure 63: Nonlinear static response: modified damage-plastic model with partial reclosure of crack and experimental results.

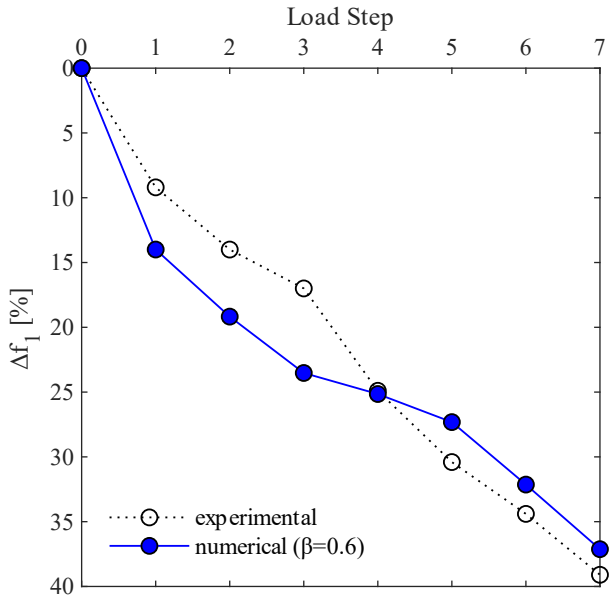

Figure 64: Frequency variation: modified damage-plastic model with partial reclosure of crack and experimental results.

Figure 65 provides a comparison of the frequency variation for the three models previously described. The model based on only damage shows a significantly deviation from the experimental results, highlighting the inadequacy to represent the

frequency variation. Especially, this model overestimates the changes of frequency, so the results can be considered as an *upper bound*. The classical damage-plastic model, corresponding to $\beta = 0$, tends to underestimate the frequency changes. The curve obtained with this model can be considered as a *lower bound*. Conversely, the modified damage-plastic model, proposed in this thesis, which accounts for the partial closure of cracks, more accurately represents the frequency variation of the damaged beams in the unloading phase.

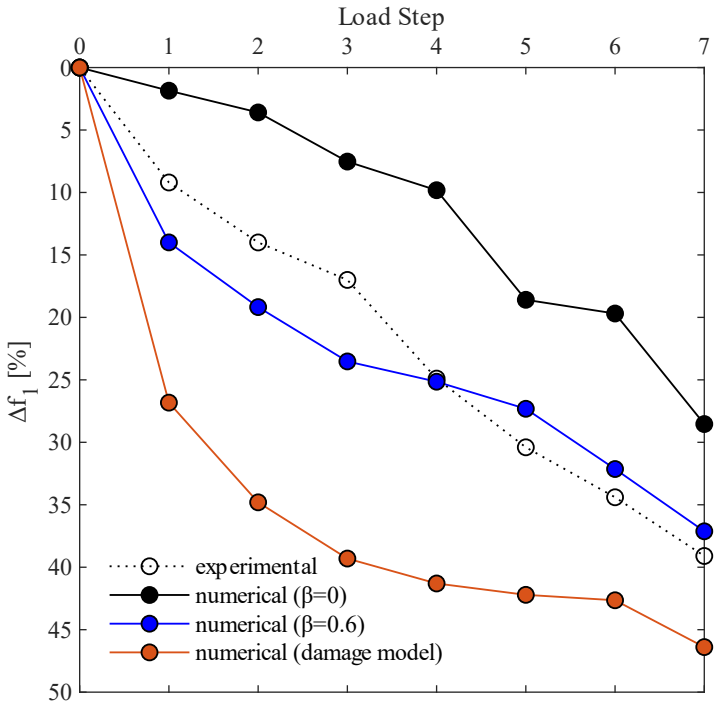

Figure 65: Comparison of frequency variation for the three models.

In conclusion, the proposed fiber beam model is capable of not only representing the nonlinear behaviour of a concrete beam but also accurately assessing the variation of frequency, as the damage of the beam increases. Therefore, the proposed modelling approach can offer a reliable and efficient method for vibration-based assessment of structural elements.

5 Neural Network training for Structural Health Monitoring

5.1 Introduction of Machine Learning for SHM

The Machine Learning technique in the context of Structural Health Monitoring (SHM) refers to the application of algorithms designed to understand structural behaviour through the experience, mirroring the learning principles of the human brain [14]. In SHM, Machine Learning is used to analyse and interpret data collected from sensors or other data sources, to detect patterns, anomalies and trends that may indicate changes in the condition or performance of a structure. Several studies discuss the application of machine learning techniques in SHM, [14], [126], [127], [128]. As mentioned in the previous chapter, two main methods are distinguished in SHM: the physics-based method and the data-driven method. The physics-based methods identify the damage of structures correlating measured data from sensors with numerical results of finite element models. Conversely, the data-driven method primarily adopts machine learning algorithms, which are based on learning from past measured data of structures. Two types of learning approaches can be identified for these algorithms: supervised and unsupervised learning. The supervised learning is based on the algorithm training with data from both undamaged and damaged conditions, whereas in unsupervised learning the training data derive exclusively from the undamaged condition of the structure. Often in bridge monitoring, the only data available are measured in the healthy state of the structure, leading to the frequent adoption of unsupervised learning methods.

In the context of machine learning techniques, the most common approach involves the use of Artificial Neural Networks (ANNs), for which numerous applications can be found in the scientific literature. For example, ANNs have been adopted for detecting damage in bridges [17], [129], for model updating to assess the structural condition [16], and for prediction of structural behaviour integrating air temperature data into the neural network [130]. Several types of neural networks are frequently utilized, such as Time Delay Neural Networks (TDNN), Layer Recurrent Networks [19], and Nonlinear AutoRegressive (NAR) networks [20]. Especially, NAR networks have been found to be particularly effective for multi-step ahead prediction, providing more precise results compared to other common neural network models.

In this chapter, the proposed fiber beam element model is adopted to train a neural network for detecting structural damage. Especially, Section 5.2 describes the proposed method to train the NAR model, while in Section 5.3 the results of two applications are presented.

5.2 Training of Artificial Neural Networks (ANNs) with Simulated Data

This section introduces the neural network model and the training strategy adopted in this work. The main idea consists in using the proposed finite element model to generate simulated data for training of ANNs algorithm, as illustrated in Figure 66. The trained algorithm can be integrated into monitoring alarm systems, which indicates the presence of structural damage, triggering timely alerts and facilitating the activation of maintenance interventions. Specifically, various damage states of the structure can be simulated through nonlinear analyses of finite element models. For each damage scenario, a low-amplitude force with White Noise time variation is applied, and nonlinear dynamic analysis is performed. The results in terms of displacement and/or acceleration are used as time-series data to train the ANNs algorithm.

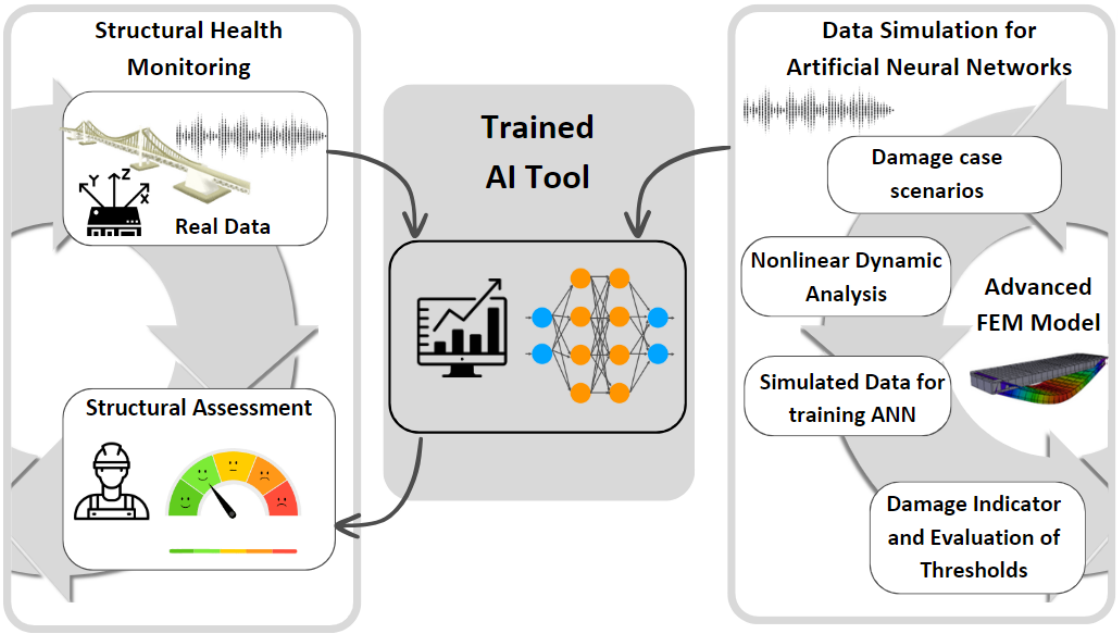

Figure 66: Monitoring strategy adopting the Artificial Neural Networks (ANNs) algorithm trained through simulated data.

This work adopts a Nonlinear AutoRegressive (NAR) networks model, implemented in MATLAB and trained using time series from the response obtained through dynamic simulations in undamaged conditions (unsupervised learning). Specifically, Nonlinear AutoRegressive (NAR) networks model predicts future values of a time series from its past values. To update the weights and biases of the neural network, the Levenberg-Marquardt optimization algorithm [131] was utilized as the training function. The architecture of the network structure is defined by two inputs: the number of hidden layers and the time delay *d*, which denotes the number of the past values adopted to predict the future value at the *d+1* time step. In the applications detailed in Section 5.3, the hidden layers and time delay are set equal to 10 and 6, respectively. The scheme of Nonlinear AutoRegressive (NAR) networks model is shown in Figure 67.

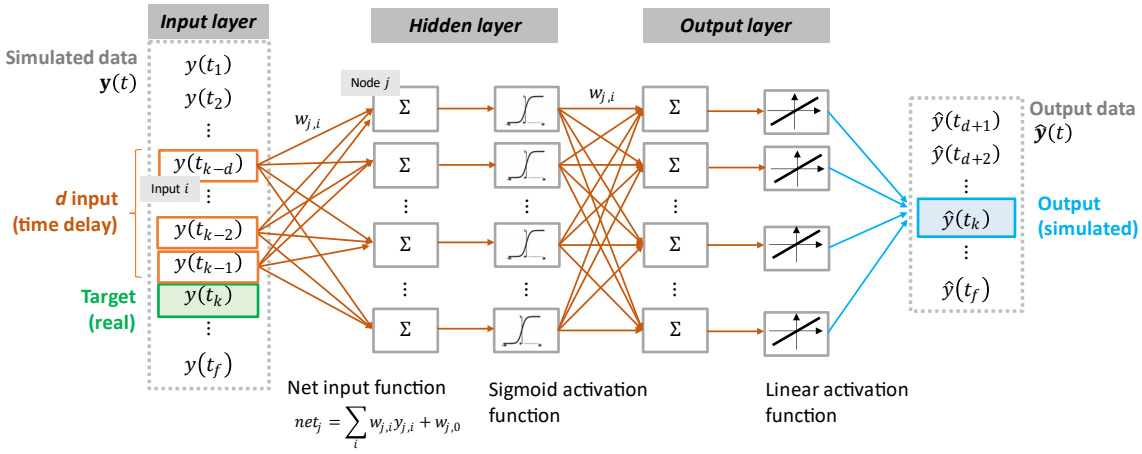

Figure 67: Nonlinear AutoRegressive (NAR) networks model.

The performance of the NAR model can be assessed by calculating the Root Mean Squared Error (RMSE) and the Normalized Root Mean Squared Error (NRMSE) between the network predictions $\hat{y}(t_k)$ (Output) and the numerical values (Target) $y(t_k)$, as follows:

$$\mathrm{RMSE} = \frac{\sum_{k=d+1}^{f} [\hat{y}(t_k) - y(t_k)]^2}{f - d}, \quad \mathrm{NRMSE} = \frac{\mathrm{RMSE}}{y^{max} - y^{min}} \tag{82}$$

where f is the final time step. The damage state of the structure can be associated to the prediction error of the neural network. The NRMSE (Normalized Root Mean Square Error) can be effective for the definition of a damage indicator and the determination of a damage detection threshold, as proposed in [132]. Figure 68

illustrates a diagram of the proposed training process adopting an unsupervised learning method. In the following section, the results of two applications are presented.

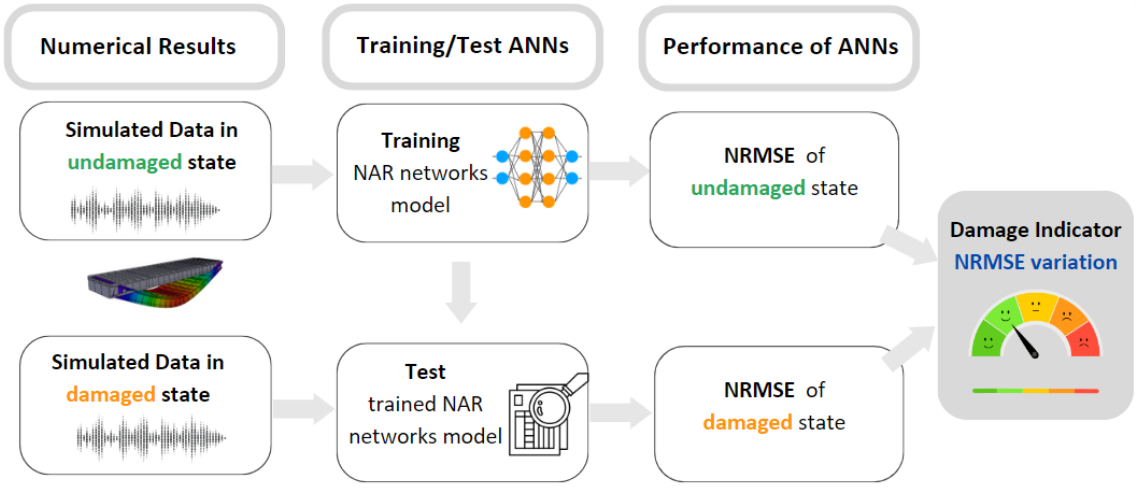

Figure 68: Definition of damage indicator in case of unsupervised learning.

5.3 Applications

This section presents two applications of the ANNs training approach described in the previous section. Specifically, the numerical results are obtained for the two beams described in Section 3.4.2 and 4.4, which correspond to the experimental tests conducted by Choi [101] and Cerri [116], respectively.

5.3.1 Application I

As illustrated in Section 3.4.2, the results of the nonlinear analysis of the HSC prestressed girder tested by Choi [101] demonstrated high accuracy in representing the nonlinear flexural behaviour of beams. For the training of the ANNs algorithm, four distinct phases of the nonlinear analysis were defined as characteristic points of the beam damage state, as shown in Figure 69. The initial phase represents the beam subjected only to its self-weight and the prestressing force. Subsequently, a vertical load, corresponding to that applied in the experimental test, was introduced. Step 2 represents the initial phase of the tensile damage at the mid-span of the beam. The third phase is characterized by a stiffness reduction caused by concrete cracking on the beam intrados. Finally, the yielding of the strands occurs in the final phase at Step 4. For each step, a nonlinear dynamic analysis was performed,

utilizing a low-amplitude force characterized by a White Noise time variation, as illustrated in Figure 69.

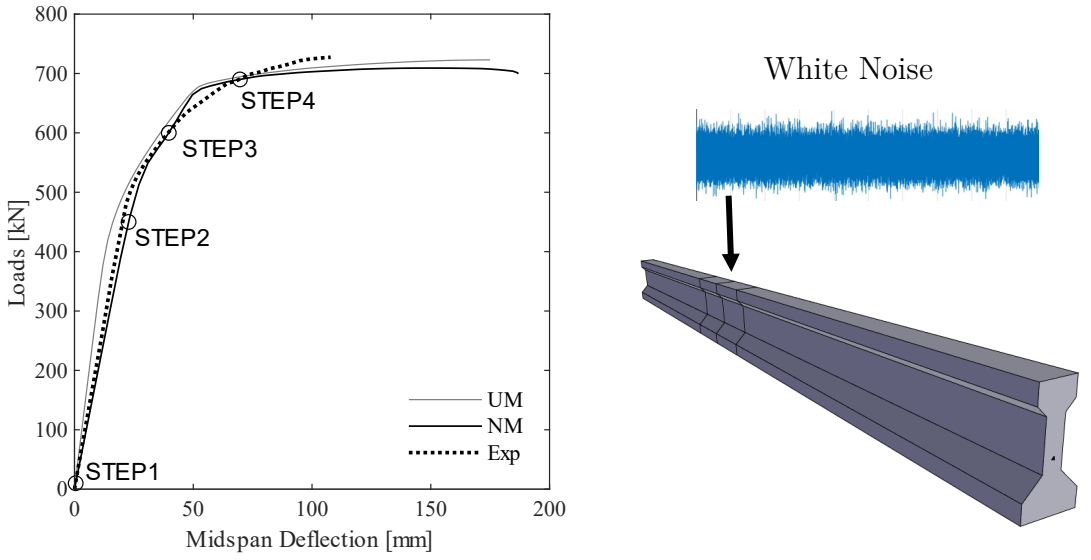

(a) *(b)*

Figure 69: Force-displacement curve (a): Uniaxial Material Model (UM), Damage-Plasticity Model (NM) and Experimental curve (Exp). Application of White Noise in FEM (b).

Six different White Noise signals were generated, each with 20000 samples and with a sampling frequency of 100 Hz. Two signals were used as excitation force applied to the beam in its reference state (Step 1) to generate training data in the undamaged scenario. The remaining four signals were employed to obtain the simulated data for testing the algorithm. Specifically, four tests were conducted: one for the reference state, Step 1, and the other three for damaged configurations, corresponding to Steps 2, 3, and 4. From the results of nonlinear dynamic analyses, the midspan displacement was extracted and converted into acceleration time series through the double integration. Applying the Fast Fourier Transform (FFT) to the time series response enabled the determination of the frequency of the first flexural mode for each damage state. Figure 70 and Figure 71 illustrate the generated acceleration time series (Target line) and the corresponding frequency response for Step 1 and Step 4, respectively. A notable reduction in the first bending mode frequency was observed, from around 10 Hz to approximately 6 Hz, which is related to the concrete cracking and the yielding of strands during the loading phases. As previously mentioned, the Nonlinear AutoRegressive (NAR) networks model was trained using two distinct White Noise (WN) signals at Step 1. Following the

training phase, the NAR networks model was employed to predict the acceleration data of four loading steps, utilizing four different WN signals. This allowed for the evaluation of the model accuracy and effectiveness in predicting the beam response to different loading conditions. The prediction response of the neural network for Steps 1 and 4 is illustrated in Figure 70 and Figure 71 with red curves (Output) and compared with simulated data from the FEM (Target).

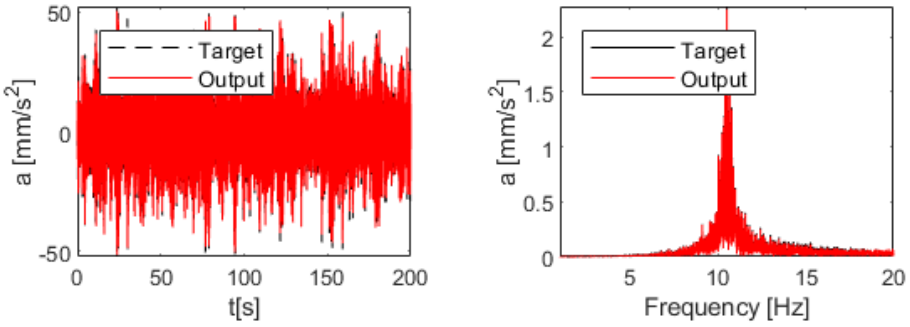

(a) *(b)*

Figure 70: Comparison between FEM (Target) and NAR (Output) results in testing phase for STEP1 in time domain (a), frequency domain (b).

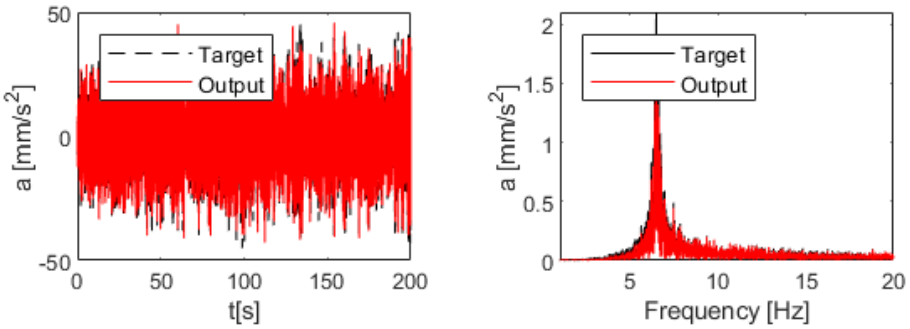

(a) *(b)*

Figure 71: Comparison between FEM (Target) and NAR (Output) results in testing phase for STEP4 in time domain (a), frequency domain (b).

Figure 72 and Figure 73 provide a zoomed view of the comparison between the acceleration derived from the FEM model (Target) and those predicted by the NAR algorithm (Output). Additionally, the error, calculated as the difference between the two time series, is illustrated.

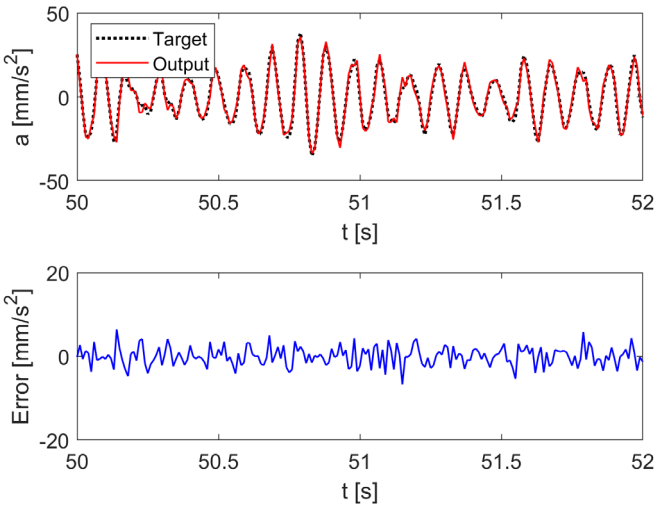

Figure 72: Performance of NAR model in testing phase - Step 1: comparison between acceleration time series from FEM (Target) and NAR (Output) model (above) and prediction error by NAR algorithm (below).

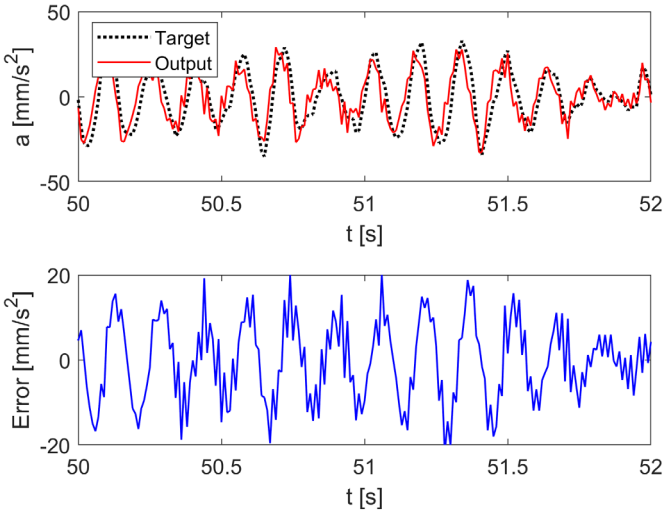

Figure 73: Performance of NAR model in testing phase - Step 4: comparison between acceleration time series from FEM (Target) and NAR (Output) model (above) and prediction error by NAR algorithm (below).

As illustrated in Figure 70 (b) and Figure 71 (b), the prediction of spectral contents in signals by the NAR model is not influenced by the damage level. In contrast, as the damage level intensifies, there is a noticeable increase in the errors related to the prediction of the amplitude of the acceleration time series, which is highlighted in Figure 72 and Figure 73. The evaluation of the Normalized Root Mean Squared Error (NRMSE) for time series predictions, as illustrated in Figure 74, allows for the analysis of the prediction error through varying damage intensities. This

evaluation allows to establish a correlation between the structural damage state and the prediction error. The results show that the prediction error can represent a suitable measure for the definition of a damage indicator able to detect the presence of damage. Specifically, it is possible to define a damage threshold, marked by a dashed red line, above which the NRMSE value indicates beam damage, and below which the beam results undamaged. Further developments of the proposed study will concern the accurate characterization of the prediction error in the reference configuration. To achieve this, a larger dataset for training phase has to be taken into account, also by considering different load cases and intensities.

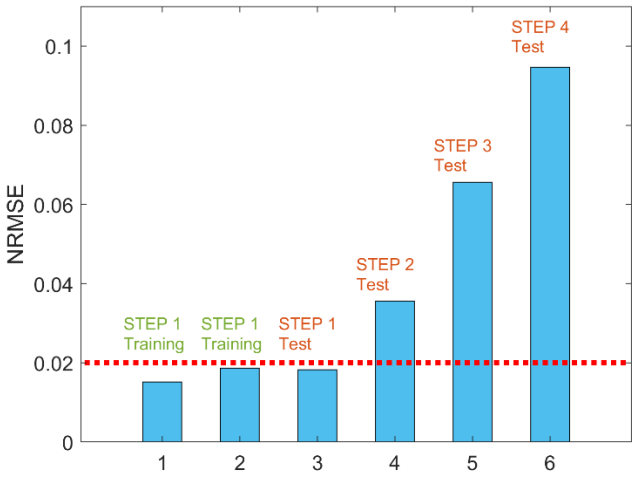

Figure 74: Normalized Root Mean Squared Error in training (undamaged configuration of structure, STEP 1) and test (undamaged, STEP 1, and damaged, STEP 2-4, configuration) phase.

5.3.2 Application II

This section presents an additional application of the proposed procedure for generating simulated data from FEM model to train the neural network. Specifically, training data were generated from the beam model representing the experimental test conducted by Cerri [116], described in Section 4.4. Figure 75 illustrates the resulting force-displacement curve of the nonlinear analysis and the analysis steps defined as characteristic points of the damage state of the beam.

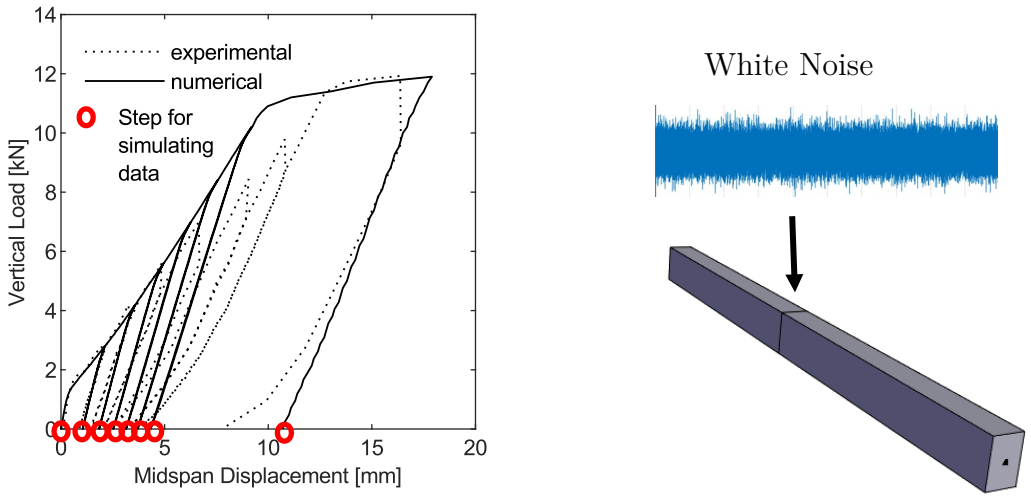

(a) *(b)*

Figure 75: Nonlinear analysis response (a). Application of White Noise in FEM model (b).

For each defined scenario, different White Noise signals were generated. A sampling frequency of 2500 Hz was adopted to obtain a frequency content able to excite the significative vibration modes of the beam. Ten nonlinear dynamic analyses were performed: three for undamaged scenarios (U1-U3) in the elastic stage, six for the different damage scenario (D1-D6) during the concrete cracking phase, and one in the yielding phase (P1). In contrast to the application discussed in the previous section, which utilized the acceleration time-series, the displacement responses were employed as simulated data for training and testing the NAR model. Specifically, the algorithm was trained using the displacement time-series obtained in the undamaged phase U1 and then tested for the various damage scenarios (U2, U3, D1-D6, P1). To avoid overfitting issues, different magnitude orders of the vibration amplitudes were adopted as training data in U1 state, as shown in Figure 76 (a). It has been observed that the neural network model encounters difficulties in providing good results if the static displacement of testing signals is higher than the displacement of training signals. Consequently, to achieve more precise predictions, the simulated data were detrended, thereby removing their static component and retaining solely the vibrational response. Figure 76 (a) shows the displacement at midspan obtained from the numerical model (Target) and network prediction (Output) for U1 state. The corresponding frequency content is illustrated in Figure 76 (b). As demonstrated by the results, the neural network prediction is accurate both in time and frequency domain.

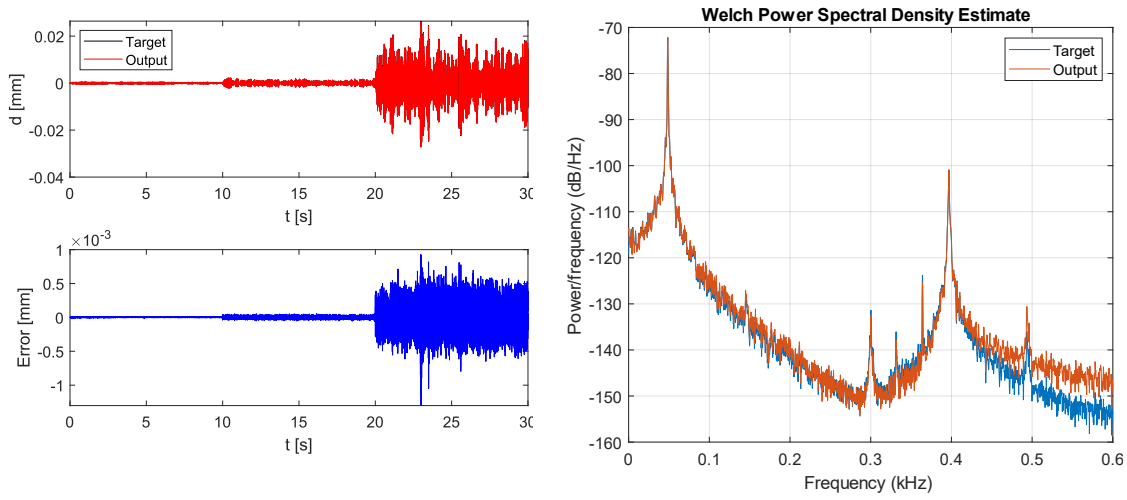

(a) *(b)*

Figure 76: Dynamic response prediction under white noise excitation through NAR model in training phase (U1): comparison between numerical response (target) and network prediction (output) of displacement time series (a) and frequency content (b).

The NAR model, trained for undamaged conditions (U1), was tested using the simulated displacement responses corresponding to conditions U1-U3, D1-D6, and P1. Figure 77 and Figure 78 illustrate the performance of the NAR model in the testing phase for state conditions D4 and P1, respectively. Specifically, the figures provide a zoomed view of the comparison between the displacement time series from the FEM (Target) and the predictions obtained through the NAR model (Output). Additionally, the corresponding prediction error is also illustrated. The results reveal a reduction of the accuracy of the neural network model prediction as damage occurs. This pattern highlights the model sensitivity to changes of structural conditions, showing that the presence of damage influences the predictive performance of the neural network model.

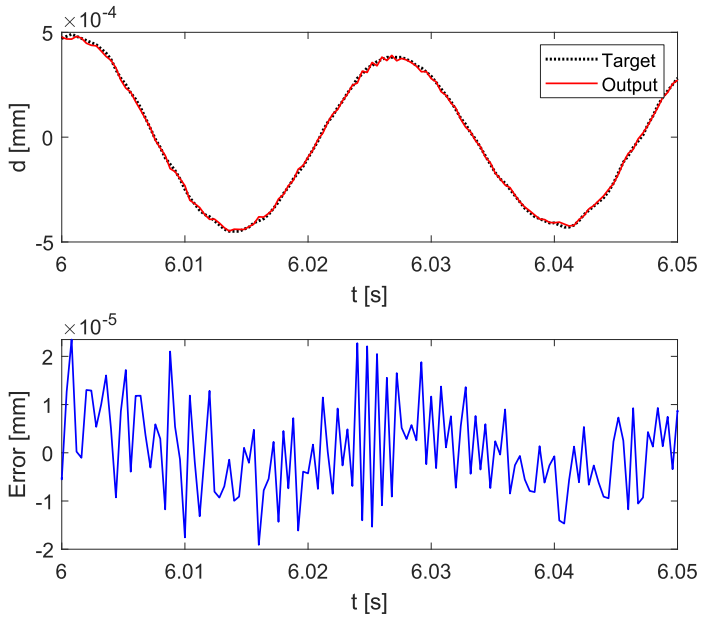

Figure 77: Performance of NAR model in testing phase - D4: comparison between displacement time series from FEM (Target) and NAR (Output) model (above) and prediction error by NAR algorithm (below).

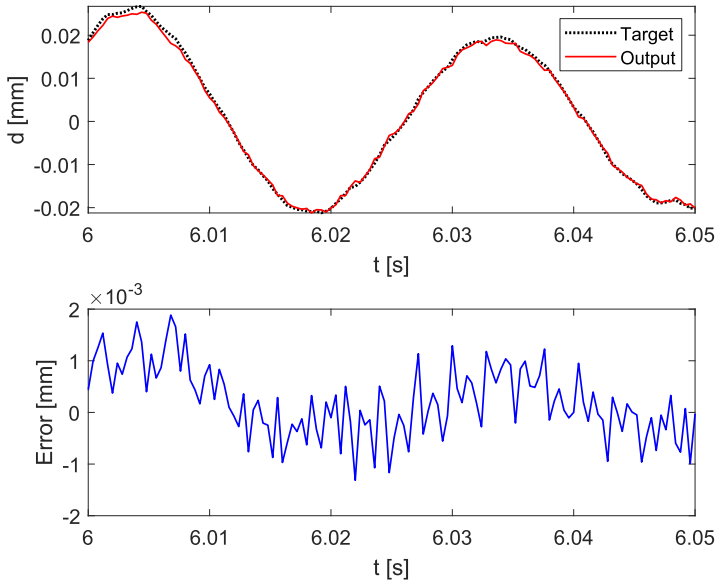

Figure 78: Performance of NAR model in testing phase - P1: comparison between displacement time series from FEM (Target) and NAR (Output) model (above) and prediction error by NAR algorithm (below).

As previously discussed, by examining the prediction error via the evaluation of NRMSE in different beam conditions, a correlation can be identified between the

error in prediction and the state of the beam. Unlike the previous application, NRMSE Variation was used as the measure of prediction error, which is defined as:

$$\text{NRMSE Variation} = \frac{\text{NRMSE} - \text{NRMSE (U1)}}{\text{NRMSE (U1)}} \tag{83}$$

being NRMSE (U1) the NRMSE calculated for the undamaged state U1. Figure 79 shows NRMSE Variation for the considered scenarios. From the results, it is possible to establish the threshold level (the red line depicted) which identifies the presence of concrete cracking.

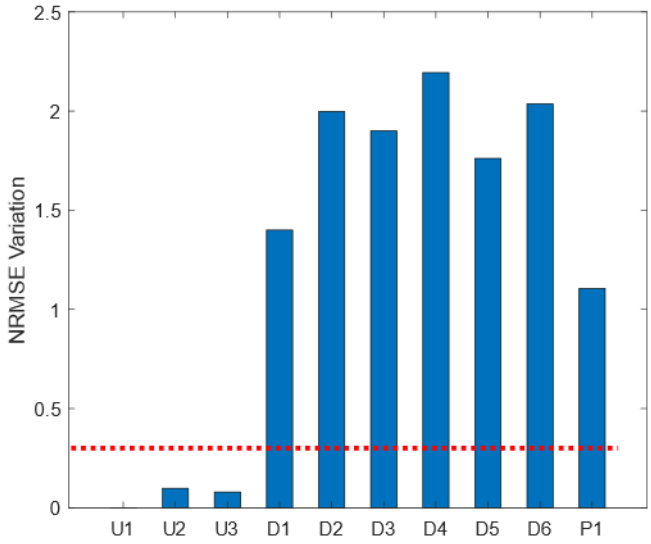

Figure 79: NRMSE Variation for the considered scenarios.

In conclusion, through the simulation of the dynamic response under white noise excitation, a neural network model has been trained in the healthy state of the structure. The failure in predicting the structural response of the damaged beam has been considered as a damage indicator able to detect the presence of the concrete cracks. Such further investigations, supported by experimental validation aiming to test the effectiveness of the simulation-based procedure in real scenarios, can improve the accuracy and applicability of machine learning techniques and better understand the relationship between prediction errors and specific types of damage.

6 Vision-Based Monitoring

6.1 Introduction of Vision-Based for Infrastructure Monitoring

Several monitoring techniques have been proposed and developed in the field of Structural Health Monitoring. The most widely adopted method for assessing structural conditions is the visual inspection conducted by human inspectors. However, this technique is often subjective and requires significant time investment, leading to considerable costs over time [[127], [133], [134], [135]]. In recent years, significant advancements in technological innovations have revealed new opportunities to overcome the disadvantages of traditional assessment methods. This technological evolution is spurring interest in innovative research areas, particularly in vision-based techniques using image acquisitions. In particular, the integration of digital image processing (DIP) and computer vision, utilizing devices like digital cameras and scanners, is becoming increasingly prevalent in civil engineering for efficient infrastructure inspection [133]. Another application of the vision-based approach consists in the use of convolutional neural networks (CNN) [136], [137] and semantic segmentation using deep learning techniques to extract region of an object in an image [138]. Grosman [139] proposed a procedure which utilizes numerical model results of a masonry bridge to generate synthetic video files to calibrate camera setups for Digital Image Correlation (DIC) monitoring. One of the most innovative technologies currently being developed is the use of unmanned aerial vehicles (UAVs) for automated inspections [21]. These UAVs, equipped with high-resolution cameras, are revolutionizing the way of conducting inspections improving their efficiency and accuracy. Recent advancements in this technology are geared towards integrating autonomous capabilities for the identification and localization of critical structural elements, as well as the detection and quantification of structural damages [22], [23], [24], [25]. To develop a fully automated vision-based assessment process, the algorithm of visual recognition systems needs to be trained through an extensive dataset of images that covers a wide variety of combinations of bridge types and damages. The complexity and variability of real structures, along with the different types of damage of structural components, mean that creating a comprehensive dataset from real images is extremely challenging. To overcome the limitations given by the scarcity of available datasets, Narazaki [25] proposed the use of synthetic environments to increase the size of these datasets to train vision-based algorithms. These artificial environments generate virtual images to simulate the real-image and associated ground truth annotations for semantic segmentation of

structural components and damage. To ensure the accuracy of the algorithm, several types of bridges with different simulated damage scenarios are generated and included in the synthetic environment. For instance, in [25], 200 synthetic environments that included 2,000 standard design railway viaducts were created. These environments produced a dataset comprising 8,648 images for structural component recognition and depth estimation, and 7,990 images for damage identification. The algorithm based on fully convolutional networks for semantic segmentation was trained using the generated dataset and real-world images. Figure 80 shows a schematic view of the use of synthetic environments for the application of unmanned aerial vehicles (UAVs) in Structural Health Monitoring.

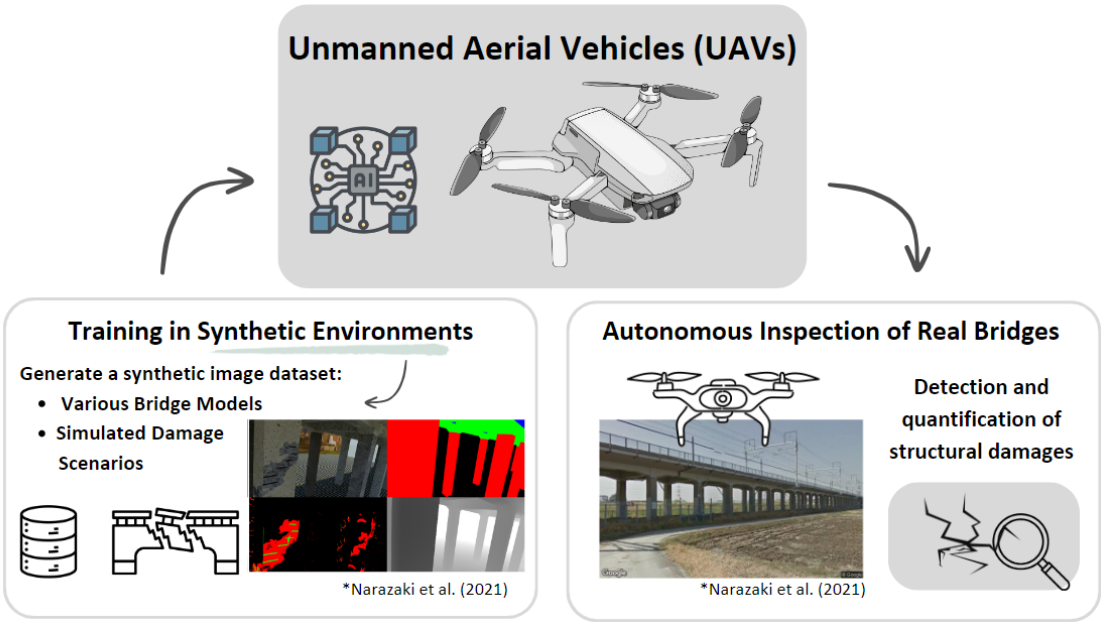

Figure 80: Scheme of unmanned aerial vehicles (UAVs) in Structural Health Monitoring.

The process of creating synthetic environments for generating training datasets in visual recognition is proposed in [25] and illustrated in Figure 81. Initially, geometric representations of the structure are determined through the creation of meshes (Step 1). Following this, the textures corresponding to different materials and damage are defined (Step 2). In the subsequent step (Step 3), these chosen images are applied to the structural model by establishing a correlation with the mesh surfaces. Once the structural model is finalized, synthetic cameras are positioned to capture the render images (Step 4) obtaining ground truth maps of structural component labels, damage labels and ground truth depth maps, which are essential for visual recognition.

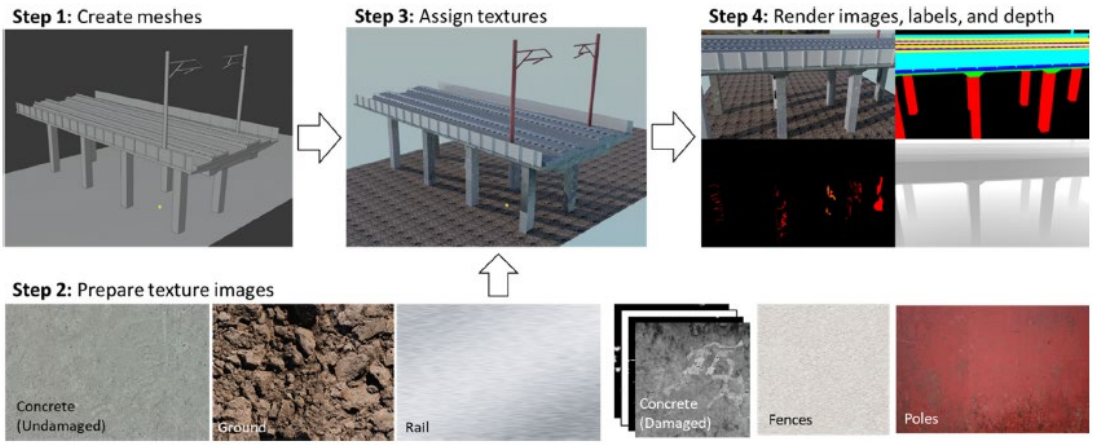

Figure 81: Scheme of creation of Synthetic environment. Figure in [25].

A significant limitation of the described work is the absence of a mechanical model in the definition of damage scenarios. Specifically, the damage is considered equally probable along the entire structural surface, without considerations for the distribution of shear forces and bending moment. Therefore, it is essential to integrate a mechanical model into this procedure that can realistically represent damage zones, thereby ensuring a more accurate simulation of real structural conditions. By integrating a mechanical model, the synthetic environment would be enhanced, leading to more robust and reliable algorithm in damage recognition.

The goal of this chapter is to adapt the proposed beam model to the process of creating synthetic environments. As demonstrated in previous chapters, the proposed fiber beam element has proven reliable in predicting the nonlinear behaviour of concrete beams, requiring low computational effort. This characteristic is crucial for creating a synthetic environment, which demands numerous nonlinear analyses to simulate several damage scenarios. Section 6.2 presents the development of a tool to use the fiber beam element in the context of vision-based techniques. Section 6.3 presents an application of the model comparing the use of DB and FB approach. Finally, Section 6.4 discusses future developments for integrating the proposed numerical model into synthetic environments.

6.2 Fiber Beam Element for Vision-Based Models

This section presents a MATLAB tool designed for post-processing visualization of fiber beams in the context of vision-based monitoring. As shown in previous chapters, fiber beam elements can reliably describe the nonlinear behaviour of beams while requiring less computational effort compared to two-dimensional or three-dimensional elements. However, their application in vision-based monitoring may be limited due to the visualization of material outputs being confined to the sections at the integration points. Indeed, to integrate a mechanical model into a vision-based procedure, it is necessary to visualize the material outputs across the external beam surface. To achieve this, a MATLAB tool was created that first interpolates fiber damage across the cross-section and then along the length of the beam, as illustrated in Figure 82. Through this method, a detailed surface-level output is produced, effectively differentiating between the cracked and uncracked areas of the beam. Additionally, this allows obtaining the length of the cracked zone, which is a key parameter to assess the damage state of the beam.

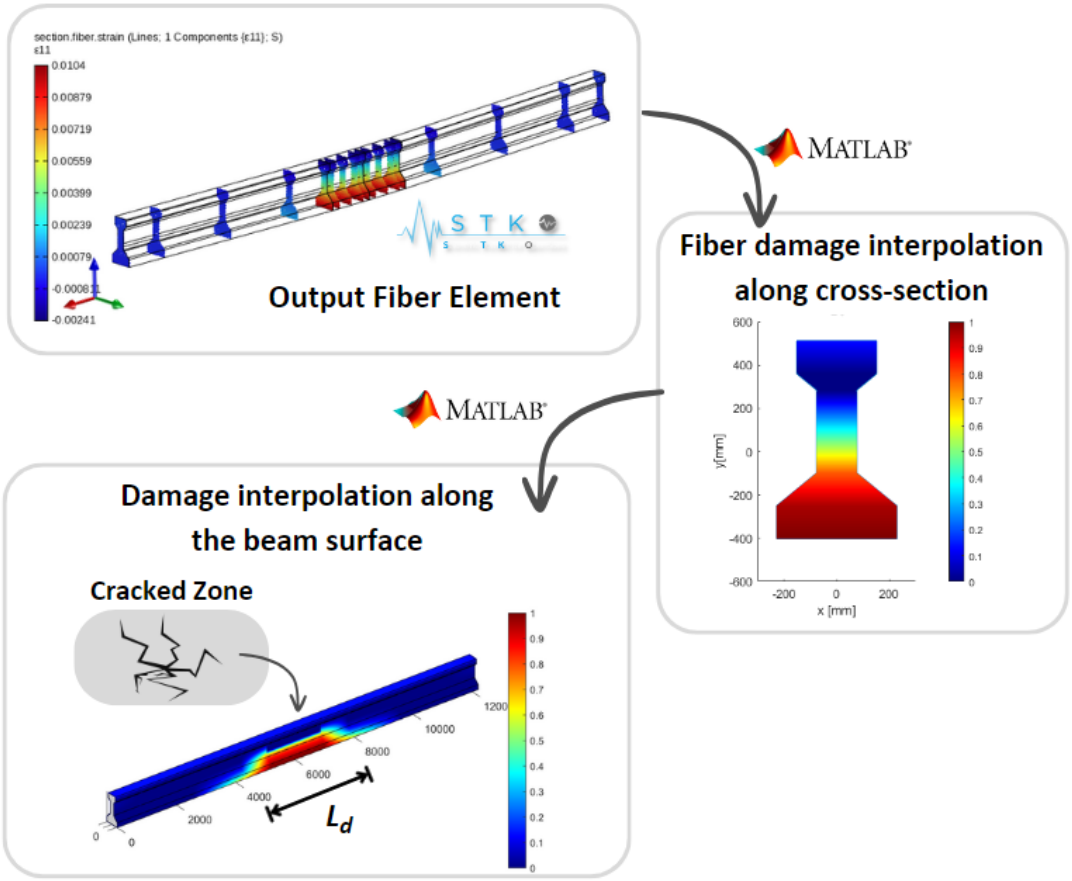

Figure 82: New Tool for post-processing of fiber beam elements for vision-based techniques.

6.3 Application

In this section, an application of the procedure proposed in the previous section is shown, comparing the use of a DB and FB fiber beam elements. The reference for this comparative study is the experimental test conducted by Cerri [116], which was initially discussed in Chapter 4. During the experimental test, the extension of the damaged zone along the beam was measured after each load increment. The experimental crack extension lengths are compared with those obtained through the numerical simulations. Differently from Chapter 4, unregularized DB and FB fiber beam finite elements were adopted. For each load step, damage results of all fibers of the beam were imported into the new MATLAB tool. This enabled the generation of a colourmap where undamaged zones (in blue) correspond to the areas where the damage variable is 0, and the cracked zones (in red) are characterized by the damage variable approximately equal to 1. The other colours are related to intermediate values of the damage variable. Figure 83 illustrates a comparison between the experimental and numerical results obtained for the DB beam element at load steps 2 and 4. It can be observed that the proposed model effectively captures the progression of damage along the beam corresponding to the increasing load.

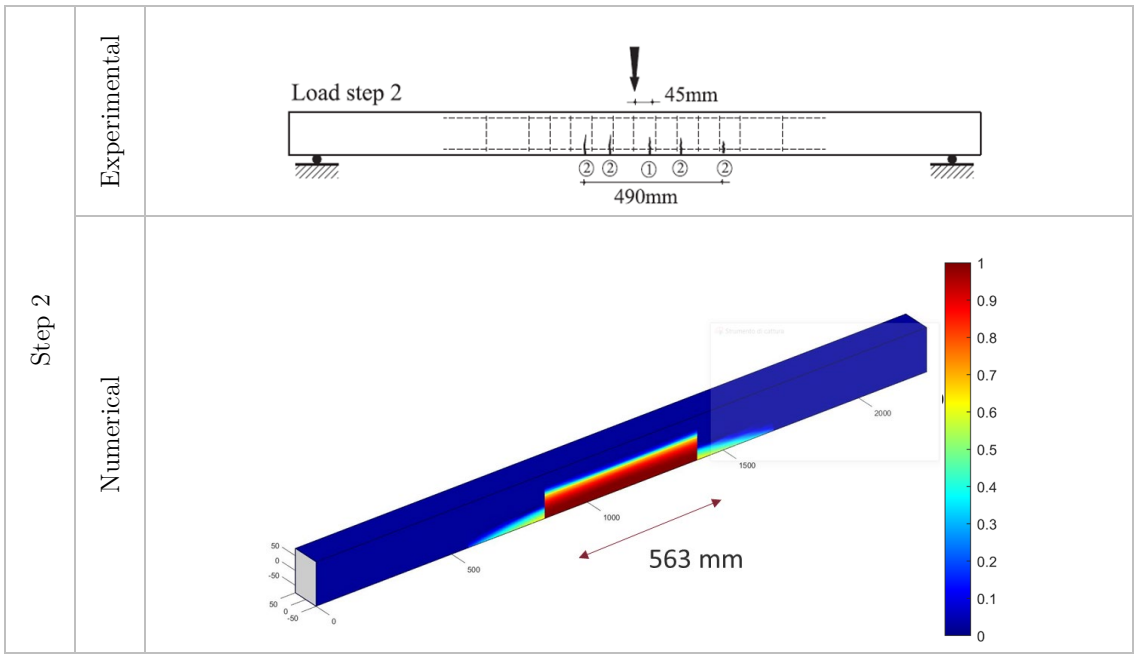

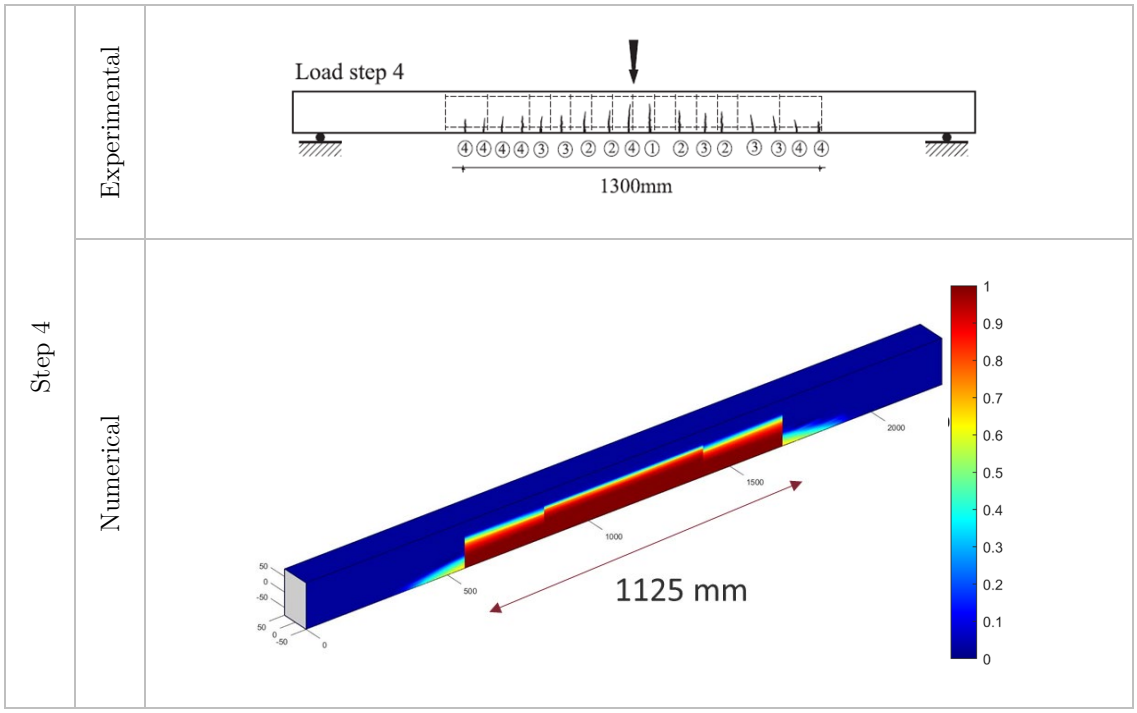

Figure 83: Experimental crack diffusion length vs numerical simulation with DB element for Step 2 and Step 4. The figures of the experimental test are in [116].

The structural response was simulated adopting both the DB and FB beam elements. Figure 84 presents a comparison of the outputs obtained with both approaches. It can be observed that for the DB beam, the progression of damage along the beam is more discontinuous compared to the FB beam, which exhibits a more uniform pattern. This behaviour is influenced by the curvature distribution, which depends on the adopted formulation, as shown in Figure 84. Analogous to the discussion presented in Section 2.5, the extension of the damaged zone along the beam is influenced by the characteristic length of the element. Therefore, when a displacement-based approach is adopted, the cracked zone length is governed by the length of the finite element. Conversely, for FB beam element, it is influenced by the selected numerical integration rule. Figure 85 shows the results obtained adopting 2, 3, and 4 elements in case of DB fiber beam element. Additionally, Figure 86 illustrates the cracked zone length, L_d, for different load steps, comparing the numerical and experimental results. It is observed that, in case of DB formulation, a finer mesh is required to accurately determine the length of the damaged zone. The results obtained adopting the FB formulation are shown in Figure 87 and Figure 88. In this case, the crack diffusion length converges to experimental results with a fewer number of elements compared to the DB approach.

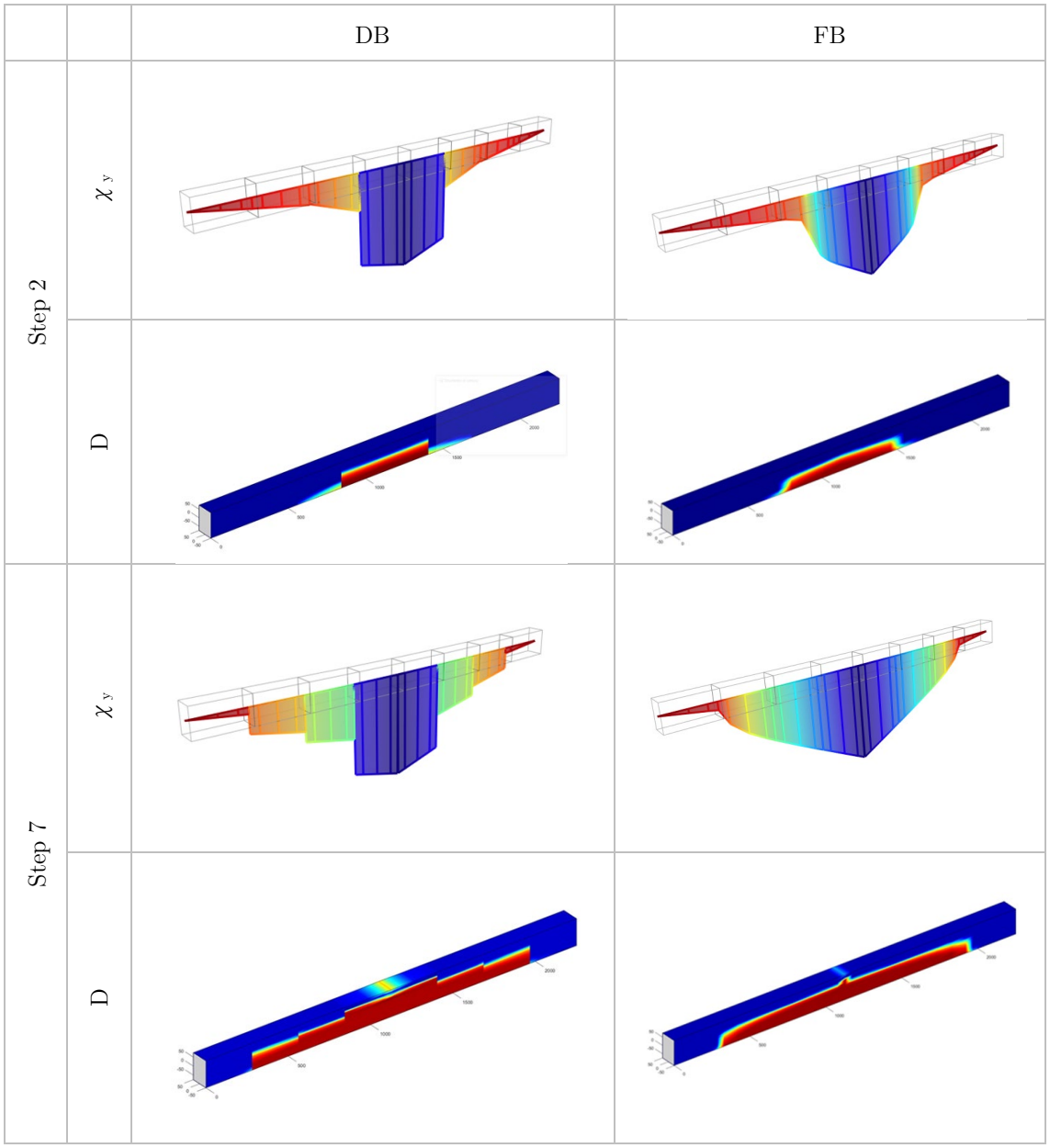

Figure 84: Curvature and damaged zone visualization for Step 2 and Step 7 for DB and FB fiber element.

In conclusion, this application demonstrated better computational performance of the FB method compared to the DB method, as discussed in Section 2.5. This investigation, however, expands the application of the fiber beam elements to the evaluation of the cracked zone extension.

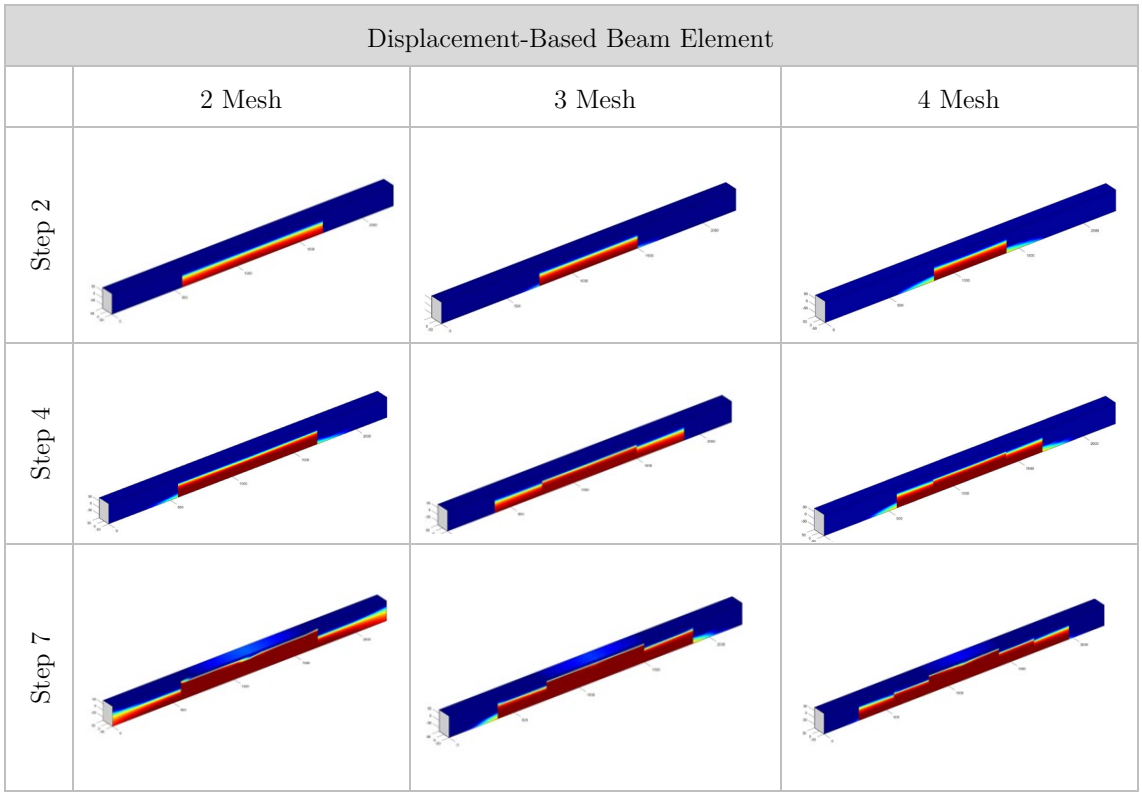

Figure 85: Damaged zone visualization: results for DB Beam Element adopting 2, 3 and 4 mesh.

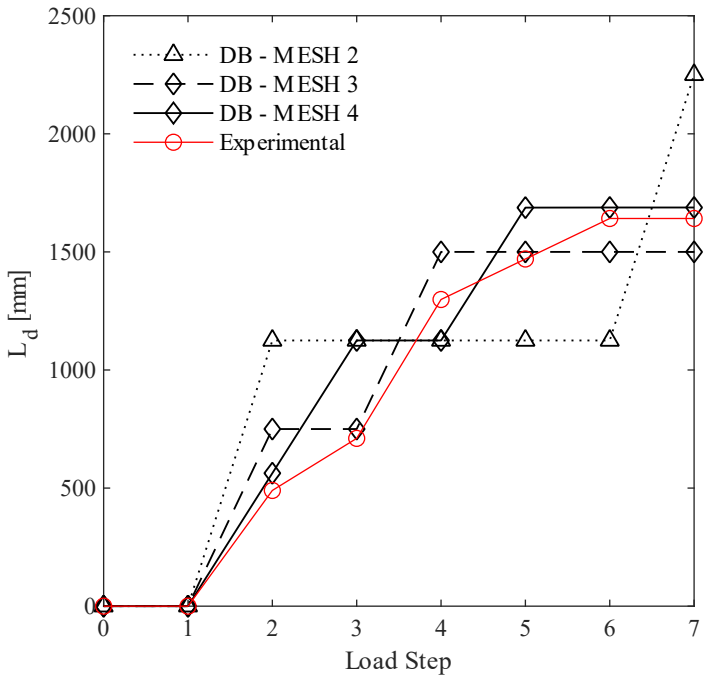

Figure 86: Cracked zone length: Experimental vs numerical results adopting DB beam elements.

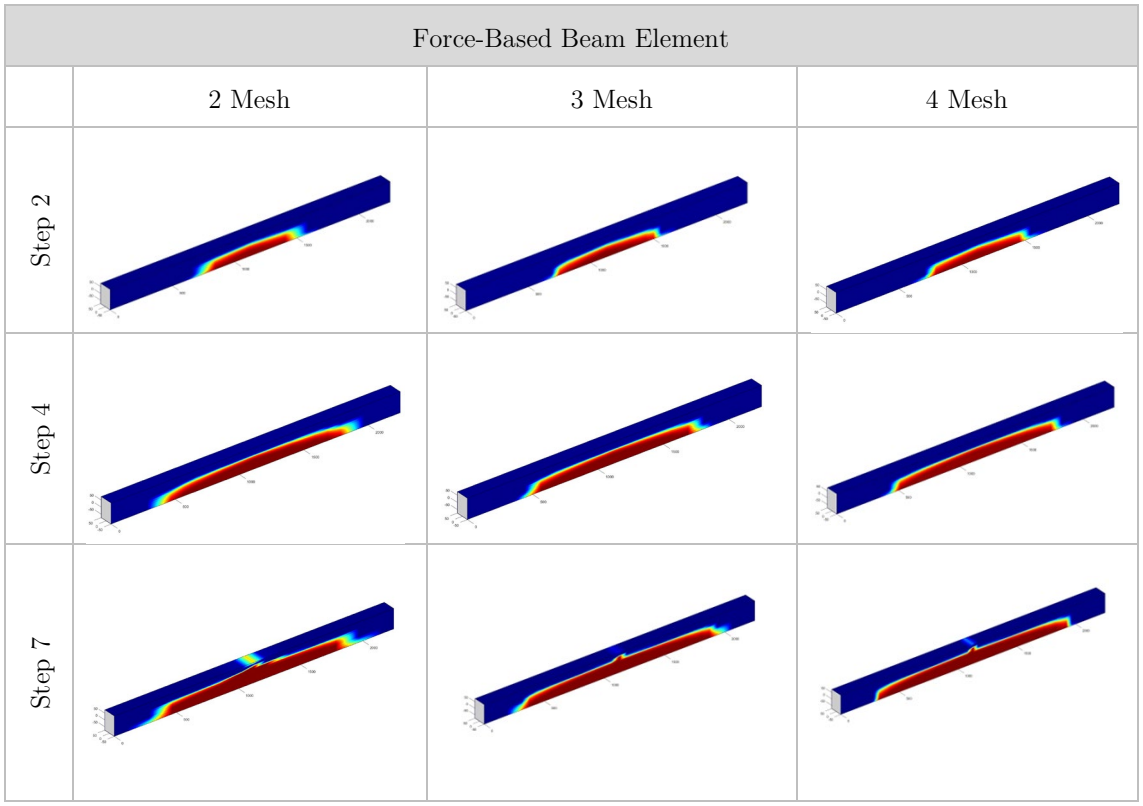

Figure 87: Damaged zone visualization: results for FB Beam Element adopting 2, 3 and 4 mesh.

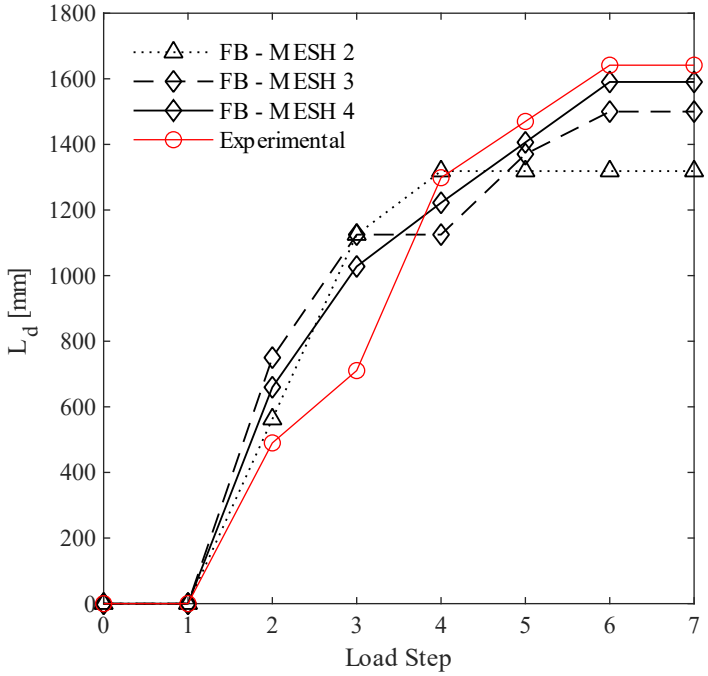

Figure 88: Cracked zone length: Experimental vs numerical results adopting FB beam elements.

6.4 Future Developments for 3D Synthetic Environments

The previous section demonstrated that fiber beam elements can capture the extension of the cracked zone along the beam surface. Through the developed MATLAB tool, which is introduced in Section 6.2, it is possible to distinctly visualize a cracked and an uncracked zone. Integrating this model in the generation of synthetic environments is suggested as a direction for future research. In [22], a methodology for physics-based graphics models (PBGMs) was introduced to simulate the damage of buildings caused by earthquakes. The application of the same concept adopting fiber beam elements in the field of SHM could represent a promising research area to enhance the reliability of vision-based system. Specifically, various damage scenarios can be simulated performing several nonlinear structural analyses for different load conditions or different degradation states of materials. To create a physics-based synthetic environment, assigning textures to cracked and uncracked areas, as illustrated in Figure 89, can improve the accuracy of generated images representing the damaged structure.

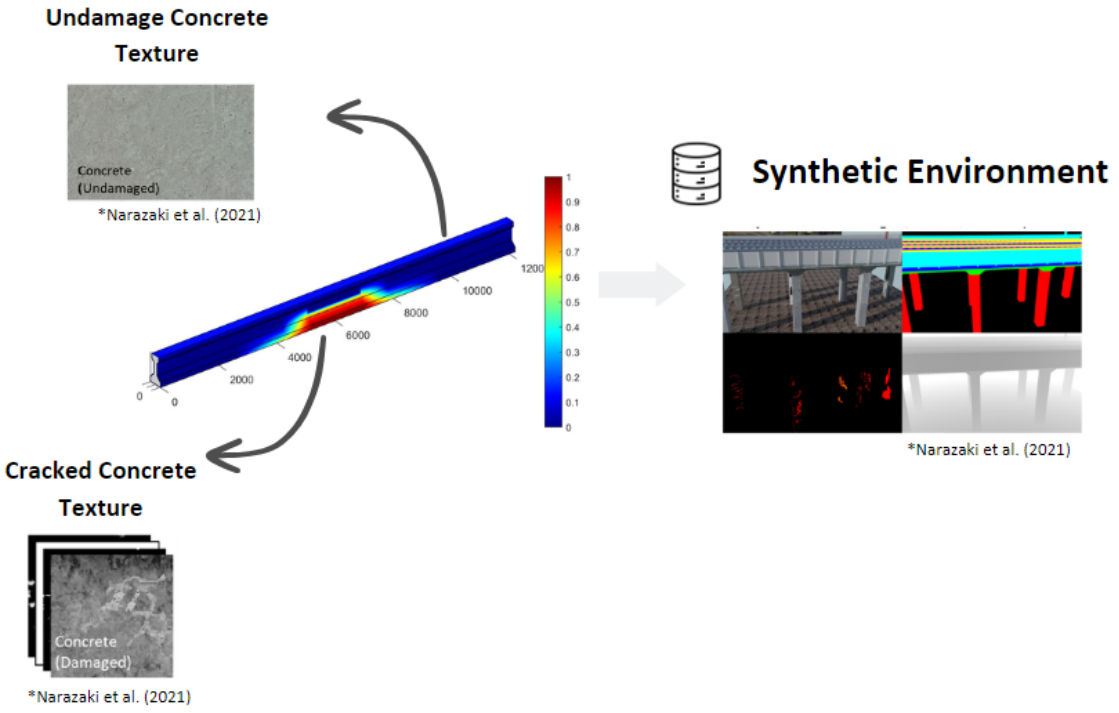

Figure 89: Future developments for proposed element in 3D synthetic environments.

7 Case Study: Alveo Vecchio Viaduct

7.1 Experimental Test

This chapter presents the application of the proposed numerical approach in the simulation of a full-scale test of an existing prestressed reinforced concrete bridge. This application aims to validate the effectiveness of the described fiber beam element in modelling the nonlinear static and dynamic behaviour of concrete bridges, highlighting the potential developments in structural health monitoring. In scientific literature, there is a limited number of full-scale bridge experiments due to a range of difficulties. Indeed, such tests are not only costly but also present organizational and safety issues. In [140], a review of full-scale failure tests on concrete bridges is provided. The experimental test selected and modelled in this research is the Alveo Vecchio viaduct, which is located in the old track of the A16 Napoli-Canosa Italian highway [141], [142]. This viaduct is representative of 52% of Italian highway bridges in terms of structural type, age and deterioration. The geometry of the bridge is illustrated in Figure 90 [142].

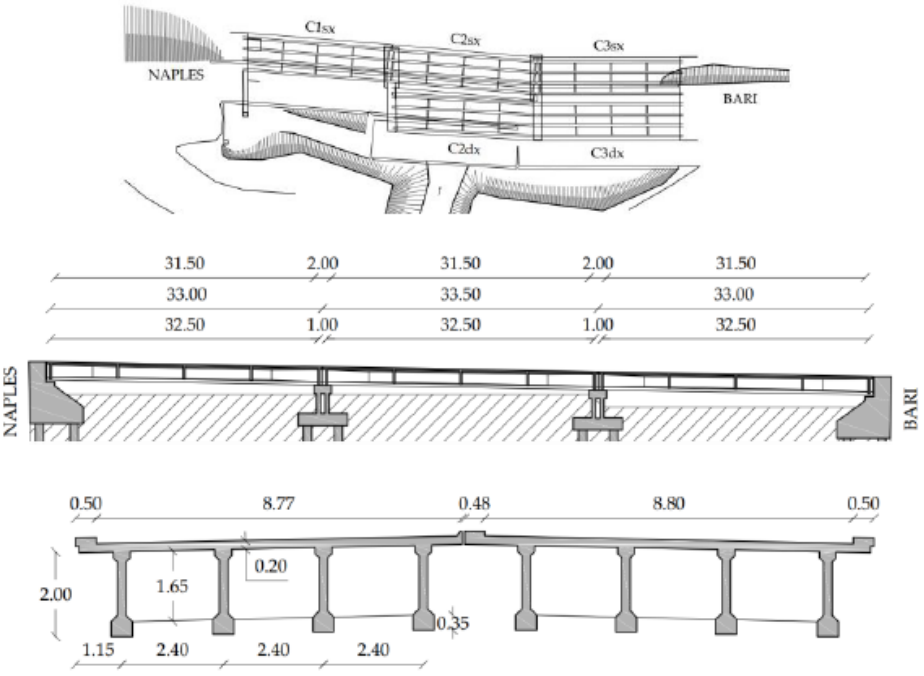

Figure 90: Geometry of Alveo Vecchio viaduct [142]

The viaduct is composed of two independent decks, characterized by three 32.5 m long simply supported spans. The structure of each span includes four prestressed concrete (PC) girders, with a height of 2 meters, and a concrete slab which is 20 cm thick. Five reinforced concrete cross-girders connect the longitudinal girders, and the bridge deck is supported by fixed and free neoprene bearings. The beams were prestressed using 14 post-tensioned parabolic cables, with a jacking tension of 1250 MPa. The ultimate strength and the yielding strength are equal to 1700 MPa and 1450 MPa, respectively. Further information regarding the structure can be found in [141].

The experimental test on span C3x involved five cycles of loading and unloading, employing progressively greater number of steel ballast blocks. Each block measured 2.35 × 1.84 × 0.45 meters and weighed 100 kN. These blocks were positioned at the centre of span C3sx, as illustrated in Figure 91. To induce the deck collapse, the experimental test was structured into five loading phases, with each phase followed by a complete unloading of the structure. The total weight applied was: P1—1200 kN, P2—2400 kN, P3—4800 kN, P4—7200 kN, and P5—9600 kN. The monitoring setup for the experimental test included several sensors, categorized into eight different types: wire displacement sensors, deformation sensors, crack-opening sensors, electronic level, temperature sensors, inclinometers, accelerometers, and acoustic emission sensors. Further details on the experimental test and the layout of the SHM system are provided in [141].

Figure 91: Picture of the Alveo Vecchio viaduct during the experimental test. Figure in [142].

To characterize the material properties, an experimental campaign was conducted both on the concrete of girders and slab and on the steel of prestressing cables and reinforcement. The results of the experimental campaign are reported in [123].

The structure was dynamically excited with a mass of 50 kg dropped from a height of 0.5 meters in loading and unloading conditions for each phase. The main frequencies were calculated from the vibrational data measured by 15 accelerometers with a sampling frequency of 800 Hz. The results, reported in Section 7.3, indicate a reduction in the frequency of the first (flexural) and second (torsional) modes of vibration, related to the progression of structural damage. Further details about the experimental results can be found in literature in [141], [142].

7.2 Finite element model

This section describes the modelling of the experimental test conducted on the Alveo Vecchio viaduct. Especially, the deck of the viaduct was numerically modelled with *OpenSees* software as solver and STKO as pre- and post-processor. Each of the four girders was divided in 24 fiber beam elements, as suggested in [141]. Additionally, the cross-girders and transverse elements representing the slab were also modelled to account for the transverse stiffness of the deck. The restraints corresponding to a simply supported structure were applied at the ends of the girders. Figure 92 and Figure 93 show the finite element model of the Alveo Vecchio viaduct.

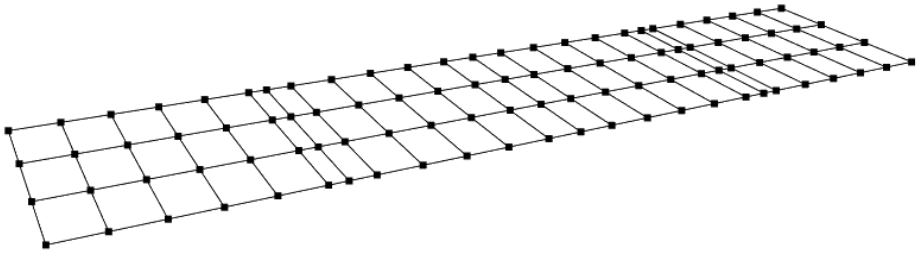

Figure 92: Model of Alveo Vecchio Viaduct: Beam elements.

Fiber beam elements were adopted to model the nonlinear behaviour of the girders, while elastic beam elements were utilized for cross-girders and slab in transversal direction. The cross-sections of fiber beam elements are given by the geometry of the girder and the portion of the collaborating slab, determined accordingly with [141]. Additionally, for beam T4, the curb was also modelled. In Figure 94, the cross-sections at the midspan of each girder are shown. The prestressing cables and the steel rebars were modelled for each cross-section according to the design

documentation of the bridge. Different beam elements along the girders were considered to account for the parabolic trajectory of the cables and the variation of the girder section geometry, as shown in Figure 95

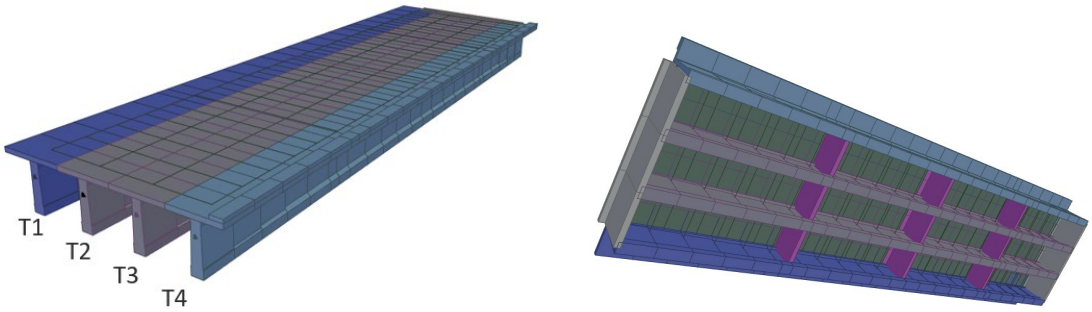

Figure 93: Model of Alveo Vecchio Viaduct: Extruded views.

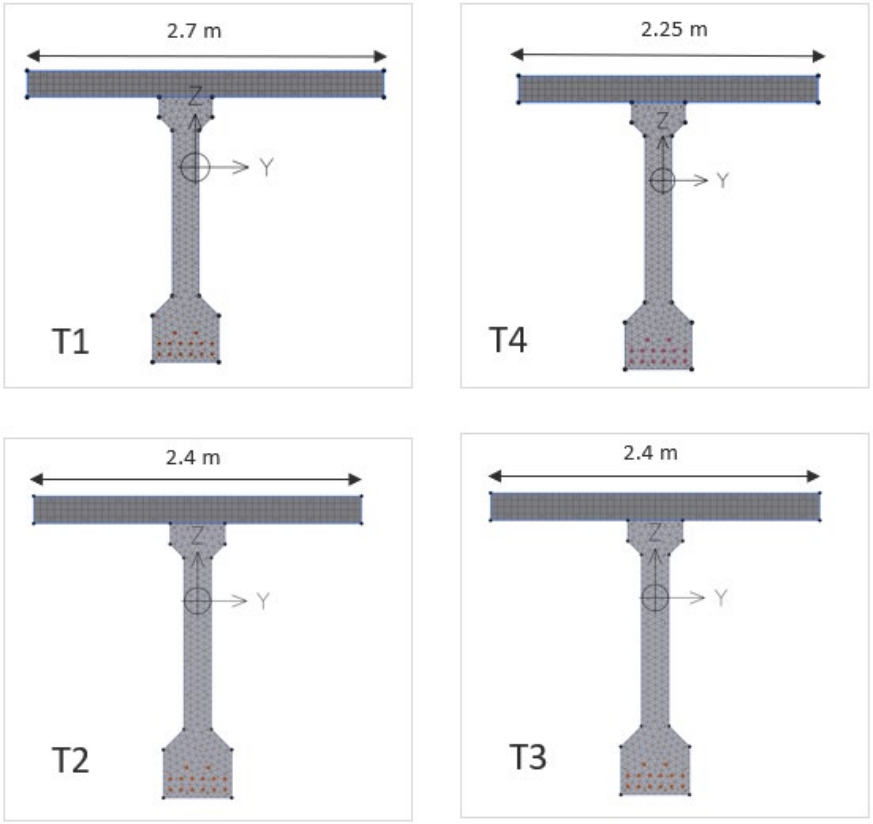

Figure 94: Cross-sections of fiber beam element at the midspan of each girder.

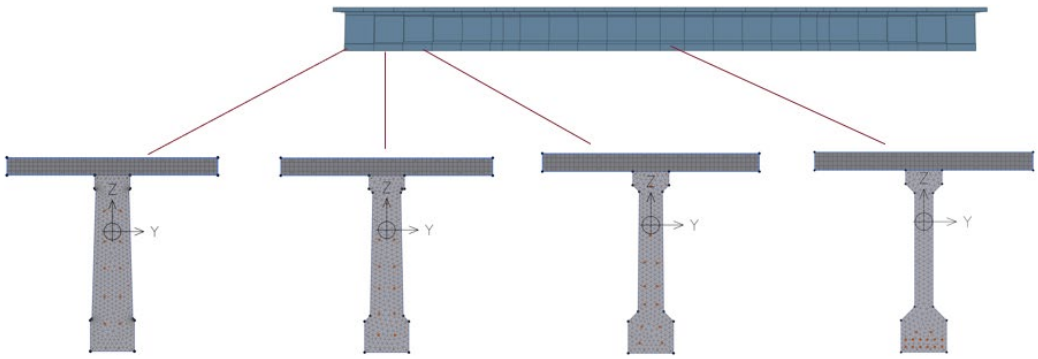

Figure 95: Cross-sections along the girders.

Permanent loads were distributed along beam elements, including the self-weight of the structural components, g_1, the weight of the pavement and the load of concrete casting used for surface levelling, g_2. To simulate the experimental test, distributed loads (p) were applied to the girders where the steel ballast blocks were positioned during the experimental test. Figure 96 shows an overview of distributed loads applied to the model. A force-controlled nonlinear analysis was performed by applying five loading-unloading cycles to simulate the experimental test.

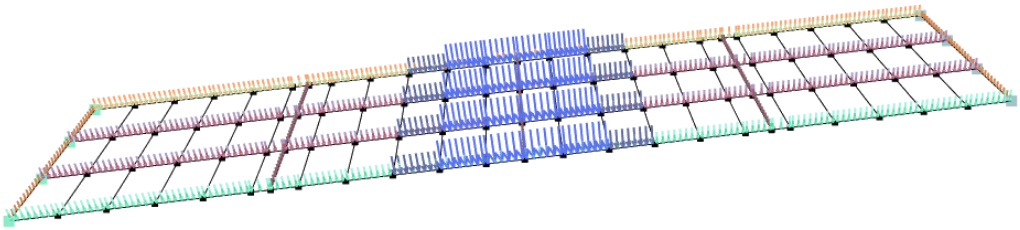

Figure 96: Distributed loads applied to the model: g_1, g_2 (in light blue purple, yellow, and orange) and p (blue).

The prestressing forces applied to the cables for each girder are detailed in Table 12. These values represent the residual stresses of the cables accounting for prestress losses over time, which resulted different for each girder. Specifically, the prestressing forces adopted in this FEM model refer to the calibrated values obtained in [141].

$T1$ [MPa]	$T2$ [MPa]	$T3$ [MPa]	$T4$ [MPa]
696	794	820	950

Table 14: Adopted values of residual stresses in prestressing cables for each girder.

Two different FEM models were considered to compare the uniaxial material (UM) existing in *OpenSees* with the modified damage-plastic (MPDM) constitutive law proposed in this research. In the first case, the *Concrete04* material was adopted for the concrete of girders and slab, with parameters listed in Table 15. The uniaxial material adopted for the steel was the *Steel04* with $f_y = 1633$ MPa and *Steel01* with $f_y = 529$ MPa for the cables and reinforcement, respectively. The mechanical parameters are aligned with hypothesis C in [141], corresponding to the 95th percentile of the Non-Destructive Testing (NDT) results.

	E_c [MPa]	f_c [MPa]	f_t [MPa]	ε_c [-]	ε_{cu} [-]
Girder	39899	49.5	2.45	0.002	0.0035
Slab	34561	36.4	2.45	0.002	0.0035

Table 15: Concrete parameter for UM constitutive laws

Regarding the modified damage plasticity model, the parameters for the concrete adopted for the girders and the slab are listed in Table 16 and Table 17, respectively. The comparison between the described uniaxial material (UM) and the new material model (MPDM) is presented in Figure 97 (a) and (b). For the steel, a plastic stress-strain relation (PM) was used for both the cables and the reinforcement, as illustrated in Figure 98 (a) and (b).

E [MPa]	ν [-]	σ_c [MPa]	σ_t [MPa]	H_i [MPa]	H_k [MPa]	κ [-]
39899	0.2	60	2.5	0.7 E	5 E	1

Y_{0c} [-]	a_c [-]	b_c [-]	Y_{0t} [-]	a_t [-]	b_t [-]	β [-]
7e-04	0.6	2.6e-03	4e-05	0.9	1.3e-04	0.2

Table 16: Concrete for Girders: modified damage-plastic model (MPDM)

E [MPa]	ν [-]	σ_c [MPa]	σ_t [MPa]	H_i [MPa]	H_k [MPa]	κ [-]
34561	0.2	50	2.5	0.2 E	0.1 E	1

Y_{0c} [-]	a_c [-]	b_c [-]	Y_{0t} [-]	a_t [-]	b_t [-]	β [-]
4e-04	0.9	2.8e-03	4e-05	0.9	1.3e-04	0

Table 17: Concrete for Slab: modified damage-plastic model (MPDM)

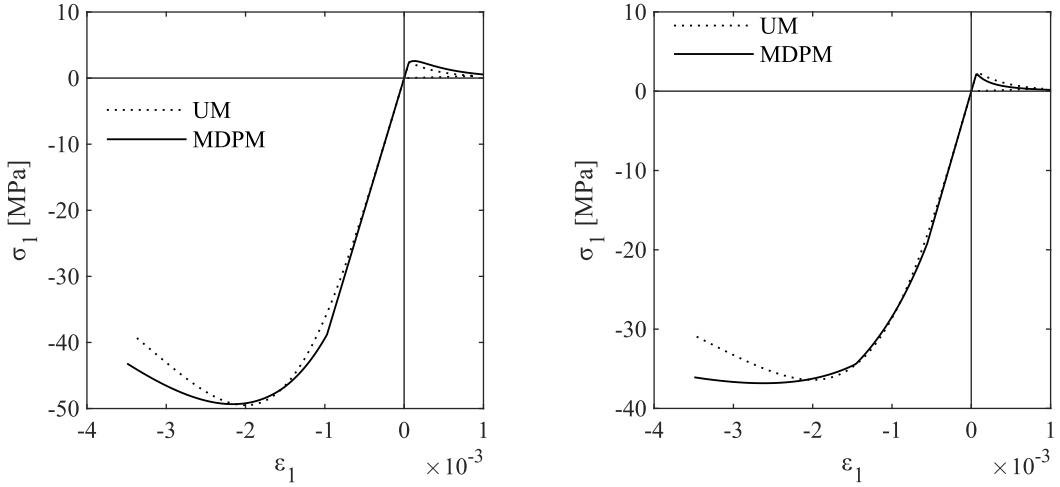

(a) *(b)*

Figure 97: Constitutive law of concrete fibers for girders (a) and slab (b): Existing Uniaxial Material (UM), Modified Damage-Plasticity Model (MDPM).

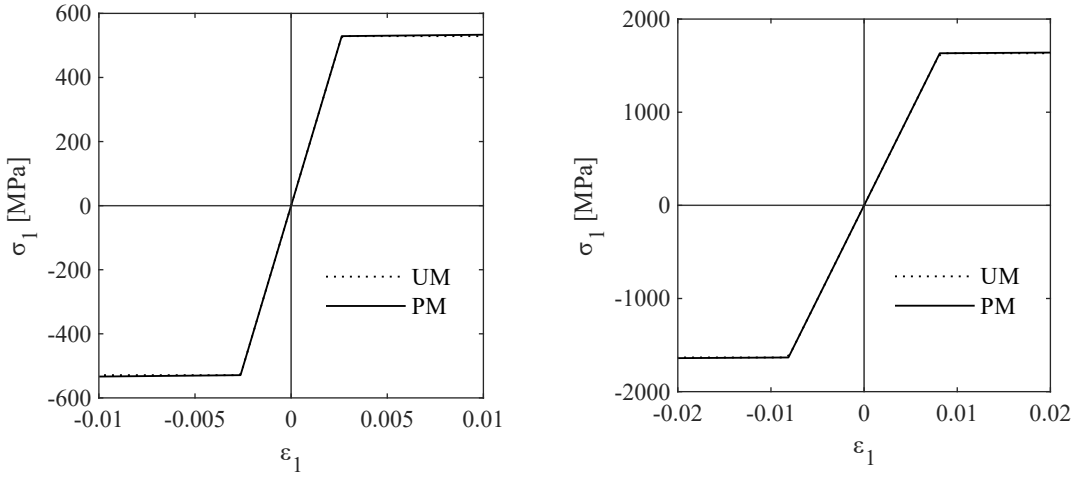

(a) *(b)*

Figure 98: Constitutive law of steel fibers for and reinforcement (a) cable (b): Existing Uniaxial Material (UM), Plasticity Model (PM).

7.3 Nonlinear Static Response and Variation of Dynamic Response with Damage

This section presents the results obtained from the nonlinear analysis for loading and unloading cycles. Figure 99 illustrates the nonlinear static response of each girder in terms of force-displacement curves. Especially, the figure compares the experimental curves with the numerical results obtained adopting the existing Uniaxial Material (UM) models for concrete and steel.

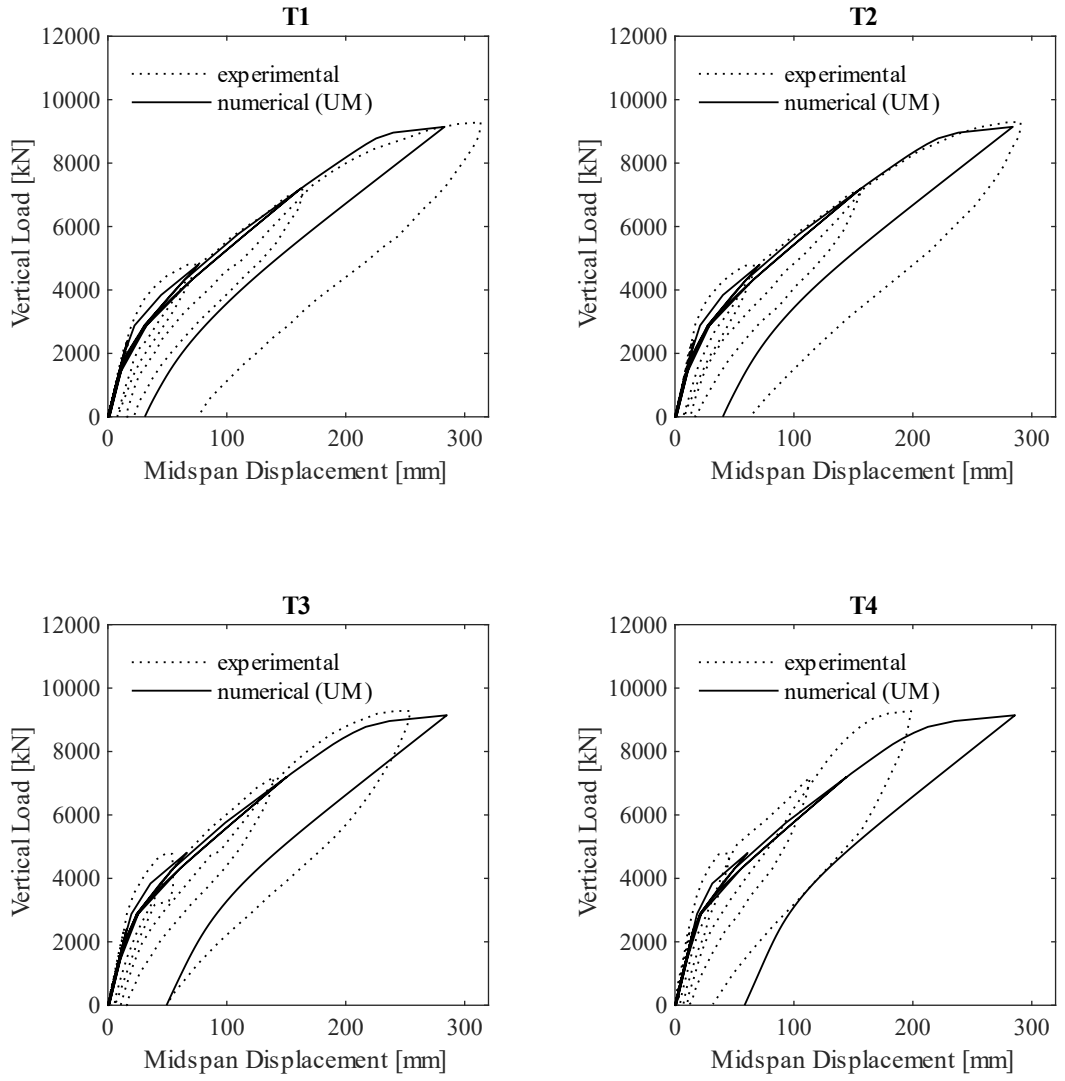

Figure 99: Nonlinear static response: Force-displacement curve for each girder - uniaxial material (UM) and experimental results.

The numerical results obtained from the model which adopts the modified damage-plastic model (MPDM) for concrete, as described in the previous paragraph, are illustrated in Figure 100.

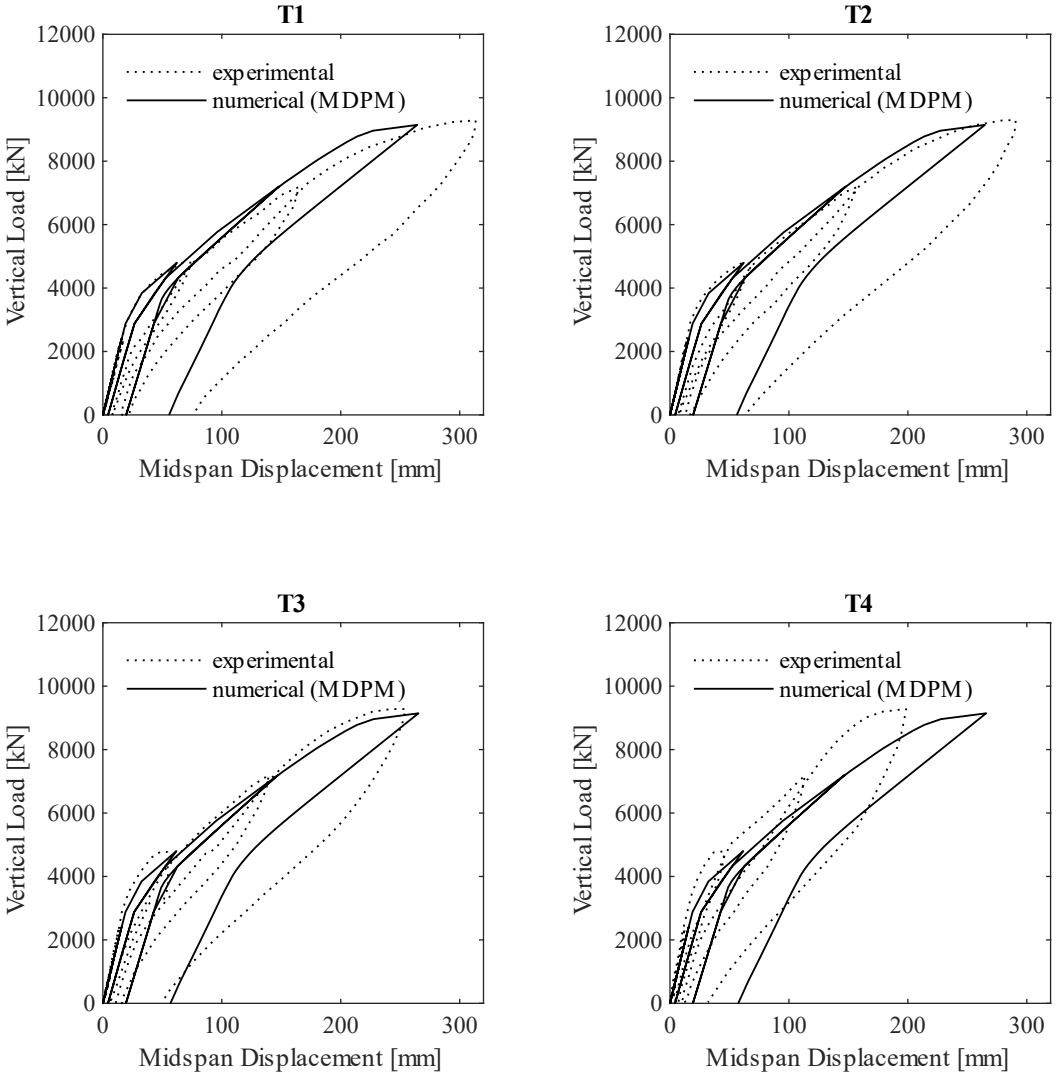

Figure 100: Nonlinear static response: Force-displacement curve for each girder - modified damage-plastic model (MDPM) and experimental results.

Both models capture the stiffness of the initial phase, which represents the elastic behaviour mainly governed by the concrete elastic modulus of the structural components. The first change of stiffness is related to the onset of the first cracks in the girder. The first-cracking point is influenced by the concrete tensile strength and the residual stress of the prestressing cables. As suggested in [141], it can be observed that the residual stress determines the first-cracking load and the post-

cracking stiffness without affecting the ultimate load capacity. In both models, the results show a good fit with the experimental data, except for the girder T4, for which the first-cracking load and the post-cracking stiffness result underestimated. The ultimate capacity is influenced by several factors, including the tensile and compressive strength of the concrete, the yield and ultimate tensile strength of the prestressing steel, and the ultimate strain of both concrete and steel. The results demonstrate a good numerical prediction for the yield point and the post-yield stiffness, except for the girder T4.

The initial phase of the unloading branch and the plastic residual displacement are mainly governed by the tensile plasticity of the concrete and, after the cables yielding, by the plasticity of the steel. As discussed in Section 4.4, the change of the stiffness in the unloading branch indicates the closing of cracks, transitioning from the tensile to compressive stress state in the cracked zone. The structural behaviour of this phase is determined by the compressive stiffness of the concrete. Although both the uniaxial material (UM) and modified damage-plastic model (MPDM) provide similar results for the loading branches, the UM does not capture the plastic residual displacement in the post-cracking phase. Since the proposed MPDM model also considers tensile plasticity of concrete, it captures the plastic residual displacements during the cracking phase, achieving a closer alignment with the experimental curves.

Although the difference between the models may not seem significant in the nonlinear response curves, it becomes crucial in the evaluation of the decrease of the first vibration frequency due to cracking. Figure 101 shows the first two modes of vibration of the deck. Specifically, the first mode is flexural, and the second mode is torsional.

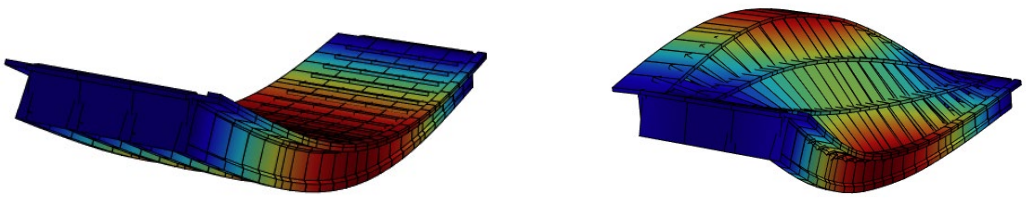

(a) *(b)*

Figure 101: First two vibration mode: Flexural (a) and Torsional (b) Mode.

Vibration frequencies were determined through the modal analysis conducted after each unloading step. The decrease of frequency for both vibration modes, caused by the progressive damage of the structure, was compared with results obtained from experimental observations. Specifically, Figure 102 (a) and (b) illustrates the frequency variations for the first and second vibration modes obtained adopting the uniaxial material (UM). Figure 103 presents the results of the model which adopts the modified damage-plastic model (MDPM).

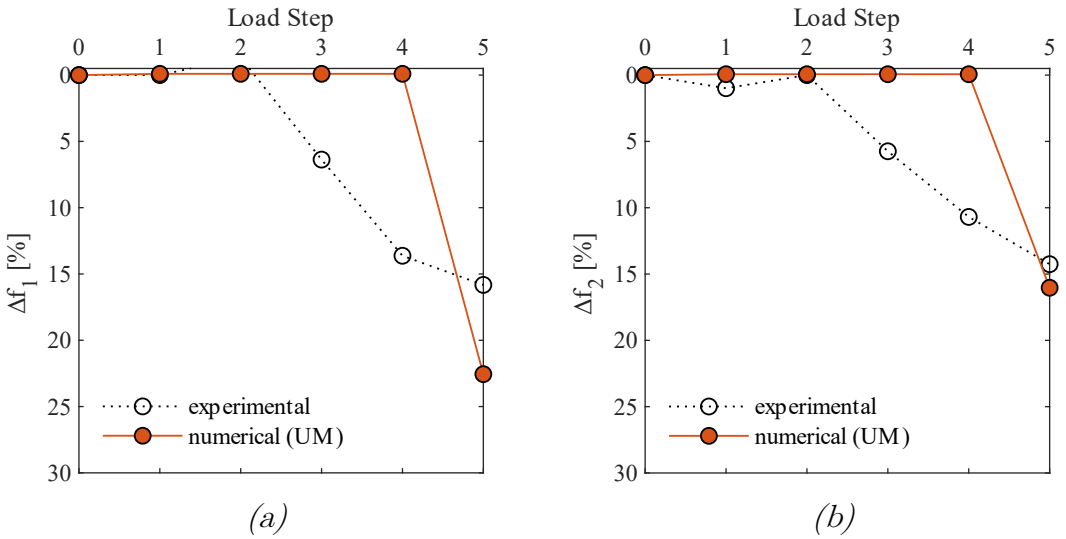

Figure 102: Frequency variation: UM model and experimental results.

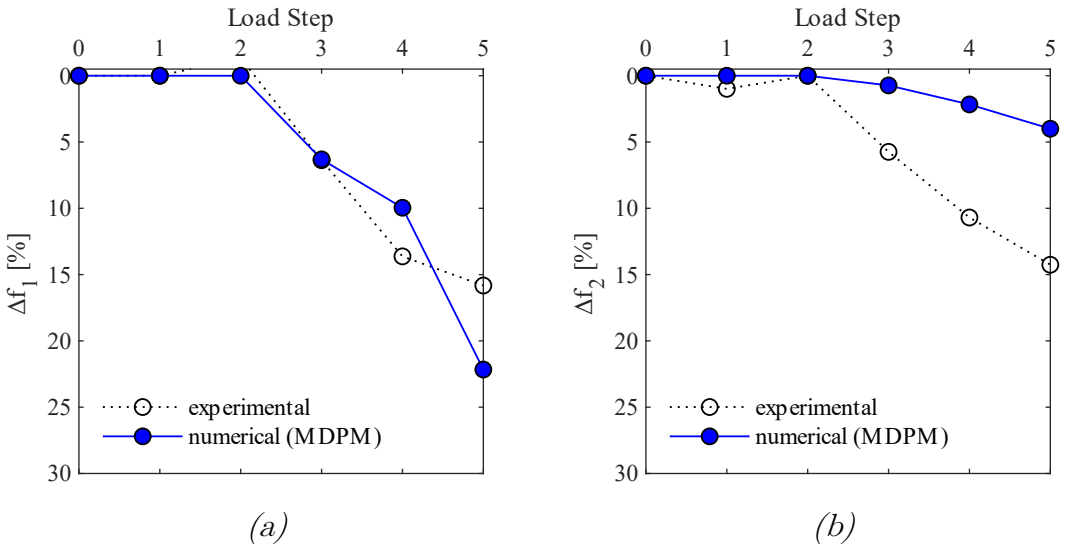

Figure 103: Frequency variation: Modified damage-plastic model and experimental results.

It can be observed that the UM model fails to capture the frequency reduction at loading steps 3 and 4, which represents the cracking phase of the girders. This observation highlights the limitation of UM model in simulating the structural behaviour under loading-unloading conditions. As discussed in Chapter 4, since the proposed MPDM considers the partial closure of cracks, it can predict the frequency value of cracked beams under unloading conditions. Figure 103 shows that for the first mode of vibration, the MPDM provides results that are more closely aligned with experimental results compared to the UM model. However, for the second mode of vibration (torsional mode), MPDM predictions underestimate the frequency variation. Further investigation is suggested to understand the factors which influence the frequency reduction in the second mode.

In conclusion, the MPDM provides a more suitable approach to modelling the structural behaviour, particularly in the unloading phase. Indeed, this includes a more accurate representation of the partial closure of cracks, ensuring that the decrease of natural frequencies is more precisely captured. This level of detail is crucial for monitoring and assessing the structural integrity of a bridge, allowing early detection of potential issues through changes in vibrational behaviour.

8 Conclusions

8.1 Summary and main contributions

This thesis proposed a computationally efficient approach to model nonlinear static and dynamic behaviour of prestressed concrete bridges in the field of Structural Health Monitoring (SHM). In this context, the integration of advanced computational models with recent advancements in artificial intelligence represents a promising approach to enhance the accuracy and efficiency of monitoring systems for detecting structural damage in infrastructures.

An advanced fiber beam element based on a damage-plastic constitutive model was implemented in *OpenSees* software framework, offering enhanced computational efficiency compared to 2D and 3D finite elements commonly used in professional practice for nonlinear analyses. A comparison between the displacement-based (DB) and force-based (FB) formulation was provided. As extensively demonstrated in literature, the force-based formulation is more efficient than the classical displacement-based approach, especially in case of nonlinear structural analysis. The adopted damage-plastic constitutive model for concrete material considers the unilateral effect of crack closure by introducing two distinct damage variables for tensile and compressive behaviour. Additionally, to accurately evaluate the frequency variation due to cracking of the structural elements, this research proposed a modification of the damage-plastic model to represent the partial closure of cracks. In this work, both 3D constitutive models, i.e. the damage-plastic and the modified damage-plastic model, have been implemented in *OpenSees.* Chapter 2 provided details on the formulation and computational aspects of the proposed advanced fiber beam model. Additionally, this chapter introduced the numerical issue of localization in case of brittle-material, by presenting and comparing various regularization methods for FB fiber beam elements.

The proposed computational approach was validated in Chapters 3, 4 and 7 by comparing the numerical results with those derived from experimental tests available in literature. Specifically, Chapter 3 focused on the nonlinear modelling techniques for prestressed concrete beams. A comparative study between the prestressed concrete fiber element model in *OpenSees* and the modelling approaches implemented in MIDAS software was presented. Additionally, this chapter illustrated a validation of the model by simulating an experimental failure test of the prestressed

concrete beam. This application demonstrated a good correlation between the numerical results and experimental measurements, confirming the model reliability in accurately representing the nonlinear structural behaviour. Chapter 4 introduced vibration-based methodologies in SHM and dynamic analysis for fiber beam elements. This chapter demonstrated the importance of adopting the modified damage-plastic model, which incorporates the partial closure of cracks, for precise evaluation of the reduction in vibration frequency due to tensile damage. The comparison between the numerical model and experimental results highlighted its efficacy in capturing not only the nonlinear behaviour but also the frequency variation. Finally, Chapter 7 presented the numerical model which simulates a full-scale experimental test of an existing prestressed reinforced concrete bridge. The results validated the proposed numerical approach also at the structural level.

In Chapter 5, this thesis also proposed a method for training an Artificial Neural Networks (ANNs) algorithm using the data generated from numerical applications. Especially, the procedure involved applying a white noise excitation to each damage scenario. Adopting an unsupervised learning approach, the neural network model was trained with data simulated in undamaged conditions. Two different numerical applications demonstrated that the prediction error of the ANNs algorithm can be considered a suitable measure for the definition of damage indicators. Additionally, the numerical simulations allowed for the evaluation of the trend of damage indicator and the determination of its alert threshold. Further research is required to improve the accuracy and applicability of the proposed procedure and better understand the relation between prediction errors and specific types of damage.

Finally, Chapter 6 explored the new advancements in the application of artificial intelligence in vision-based monitoring. A tool was developed to enable the use of the proposed fiber beam model for creating synthetic environments. The application discussed in this chapter demonstrated that the FB formulation is more efficient in determining the length of the damaged zone.

In conclusion, this thesis proposed and validated an advanced finite element to simulate the structural static and dynamic behaviour of bridges. Furthermore, it explored the applications of this numerical approach to enhance the performance of artificial intelligence in structural monitoring.

8.2 Recommendations for future works

Future works can further explore the integration of the proposed advanced numerical model in structural health monitoring. Future developments are listed here:

1. Enhance the proposed formulation including the modelling of shear failure and bond-slip effect.
2. Integrate the modelling of material degradation phenomena of existing bridges, as the steel corrosion and concrete deterioration. Especially, the corrosion can lead to the reduction of steel area and cause concrete cracking, potentially resulting in spalling of the cover.
3. Further applications of the proposed ANNs training procedures to enhance the accuracy of machine learning techniques in structural health monitoring. This study could focus on understanding the correlations between prediction error and different types of structural damage.
4. Validate the neural network algorithm trained with simulated data. This involves testing the algorithm on real bridges, including further investigation about the effect of environmental factors such as temperature and humidity variations.
5. Enhance the ANNs training procedure to include the capability of locating damage. One method could involve extracting the structural responses from different points located along the girder and observing if the damage indicator shows higher values for the results extracted in the damaged area.
6. Propose a hybrid procedure for calibrating the characteristic parameter of partial crack closure using real data measured by the monitoring system.
7. Develop a training procedure based on the supervised learning approach. In this case, the algorithm will be trained using data from both damaged and undamaged conditions.
8. Develop an automated tool for assigning specific textures to cracked and uncracked areas to obtain realistic images of damaged beams. Additionally, create a synthetic environment with a range of damage scenarios for training visual recognition algorithms.

Bibliography

[1] American Society of Civil Engineer (ASCE), "Report Card for America's Infrastructure," 2021.

[2] M. Zizi, P. Bencivenga, and G. De Matteis, "Handling policies for Italian existing bridges with a territorial approach: the case study of Caserta, Italy," *Structures*, vol. 48, pp. 1306–1321, Feb. 2023, doi: 10.1016/j.istruc.2022.12.114.

[3] G. Santarsiero, A. Masi, V. Picciano, and A. Digrisolo, "The Italian Guidelines on Risk Classification and Management of Bridges: Applications and Remarks on Large Scale Risk Assessments," *Infrastructures (Basel)*, vol. 6, no. 8, p. 111, Aug. 2021, doi: 10.3390/infrastructures6080111.

[4] K. Kauss, V. Alves, F. Barbosa, and A. Cury, "Semi-supervised structural damage assessment via autoregressive models and evolutionary optimization," *Structures*, vol. 59, p. 105762, Jan. 2024, doi: 10.1016/j.istruc.2023.105762.

[5] D. Fiandaca *et al.*, "An Integrated Approach for Structural Health Monitoring and Damage Detection of Bridges: An Experimental Assessment," *Applied Sciences*, vol. 12, no. 24, p. 13018, Dec. 2022, doi: 10.3390/app122413018.

[6] S. Arangio and F. Bontempi, "Design Knowledge Gain by Structural Health Monitoring," in *Maintenance and Safety of Aging Infrastructure*, CRC Press, 2014, pp. 95–120. doi: 10.1201/b17073-4.

[7] M. Mishra, P. B. Lourenço, and G. V. Ramana, "Structural health monitoring of civil engineering structures by using the internet of things: A review," *Journal of Building Engineering*, vol. 48, p. 103954, May 2022, doi: 10.1016/j.jobe.2021.103954.

[8] Wei Fan and Pizhong Qiao, "Vibration-based Damage Identification Methods: A Review and Comparative Study," *Struct Health Monit*, vol. 10, no. 1, pp. 83–111, Jan. 2011, doi: 10.1177/1475921710365419.

[9] E. P. Carden and P. Fanning, "Vibration Based Condition Monitoring: A Review," *Struct Health Monit*, vol. 3, no. 4, pp. 355–377, Dec. 2004, doi: 10.1177/1475921704047500.

[10] O. S. Salawu, "Detection of structural damage through changes in frequency: a review," *Eng Struct*, vol. 19, no. 9, pp. 718–723, Sep. 1997, doi: 10.1016/S0141-0296(96)00149-6.

[11] K. F. Tee, "Time Series Analysis for Vibration-Based Structural Health Monitoring: A Review," *Structural Durability & Health Monitoring*, vol. 12, no. 3, pp. 129–147, 2018, doi: 10.3970/SDHM.2018.04316.

[12] J. M. Ndambi, J. Vantomme, and K. Harri, "Damage assessment in reinforced concrete beams using eigenfrequencies and mode shape derivatives," *Eng Struct*, vol. 24, no. 4, pp. 501–515, Apr. 2002, doi: 10.1016/S0141-0296(01)00117-1.

[13] A. Teughels and G. De Roeck, "Structural damage identification of the highway bridge Z24 by FE model updating," *J Sound Vib*, vol. 278, no. 3, pp. 589–610, Dec. 2004, doi: 10.1016/j.jsv.2003.10.041.

[14] E. Figueiredo and A. Santos, "Machine Learning Algorithms for Damage Detection," in *Vibration-Based Techniques for Damage Detection and Localization in Engineering Structures*, 2018, pp. 1–39. doi: 10.1142/9781786344977_0001.

[15] H. Seon Park, J. Hwan An, Y. Jun Park, and B. Kwan Oh, "Convolutional neural network-based safety evaluation method for structures with dynamic responses," *Expert Syst Appl*, vol. 158, p. 113634, Nov. 2020, doi: 10.1016/j.eswa.2020.113634.

[16] C. C. Chang, T. Y. P. Chang, and Y. G. Xu, "Adaptive neural networks for model updating of structures," *Smart Mater Struct*, vol. 9, no. 1, p. 59, Feb. 2000, doi: 10.1088/0964-1726/9/1/306.

[17] S. V. Barai and P. C. Pandey, "Vibration Signature Analysis Using Artificial Neural Networks," *Journal of Computing in Civil Engineering*, vol. 9, no. 4, pp. 259–265, 1995, doi: 10.1061/(asce)0887-3801(1995)9:4(259).

[18] J. Shu, Z. Zhang, I. Gonzalez, and R. Karoumi, "The application of a damage detection method using Artificial Neural Network and train-induced vibrations on a simplified railway bridge model," *Eng Struct*, vol. 52, pp. 408–421, Jul. 2013, doi: 10.1016/j.engstruct.2013.02.031.

[19] R. Lippmann, "Book Review: 'Neural Networks, A Comprehensive Foundation', by Simon Haykin," *Int J Neural Syst*, vol. 05, no. 04, pp. 363–364, Dec. 1994, doi: 10.1142/S0129065794000372.

[20] T. W. S. Chow and C.-T. Leung, "Nonlinear autoregressive integrated neural network model for short-term load forecasting," *IEE Proceedings - Generation, Transmission and Distribution*, vol. 143, no. 5, pp. 500–506, 1996, doi: 10.1049/ip-gtd:19960600.

[21] N. Hallermann and G. Morgenthal, "Visual inspection strategies for large bridges using Unmanned Aerial Vehicles (UAV)," in *Bridge Maintenance, Safety, Management and Life Extension - Proceedings of the 7th International Conference of Bridge Maintenance, Safety and Management, IABMAS 2014*, 2014. doi: 10.1201/b17063-96.

[22] V. Hoskere, Y. Narazaki, and B. F. Spencer, "Physics-Based Graphics Models in 3D Synthetic Environments as Autonomous Vision-Based Inspection Testbeds," *Sensors*, vol. 22, no. 2, p. 532, Jan. 2022, doi: 10.3390/s22020532.

[23] B. F. Spencer, V. Hoskere, and Y. Narazaki, "Advances in Computer Vision-Based Civil Infrastructure Inspection and Monitoring," *Engineering*, vol. 5, no. 2, pp. 199–222, Apr. 2019, doi: 10.1016/j.eng.2018.11.030.

[24] Y. Narazaki, V. Hoskere, G. Chowdhary, and B. F. Spencer, "Vision-based navigation planning for autonomous post-earthquake inspection of reinforced concrete railway viaducts using unmanned aerial vehicles," *Autom Constr*, vol. 137, p. 104214, May 2022, doi: 10.1016/j.autcon.2022.104214.

[25] Y. Narazaki, V. Hoskere, K. Yoshida, B. F. Spencer, and Y. Fujino, "Synthetic environments for vision-based structural condition assessment of Japanese high-speed railway viaducts," *Mech Syst Signal Process*, vol. 160, p. 107850, Nov. 2021, doi: 10.1016/j.ymssp.2021.107850.

[26] Y. Zheng, Y. L. Xu, and Q. Gu, "Nonlinear model updating of a reinforced concrete pedestrian cable-stayed bridge," *Struct Control Health Monit*, vol. 27, no. 3, Mar. 2020, doi: 10.1002/stc.2487.

[27] O. C. Zienkiewicz and R. L. Taylor, *The finite element method. Volume 1: Basic formulation and linear problems*, vol. 3. 1994.

[28] E. Spacone, F. C. Filippou, and F. F. Taucer, "Fibre beam-column model for non-linear analysis of R/C frames: Part II. Applications," *Earthq Eng Struct Dyn*, vol. 25, no. 7, pp. 727–742, 1996, doi: 10.1002/(SICI)1096-9845(199607)25:7<727::AID-EQE577>3.0.CO;2-O.

[29] D. Addessi and V. Ciampi, "A regularized force-based beam element with a damage–plastic section constitutive law," *Int J Numer Methods Eng*, vol. 70, no. 5, pp. 610–629, Apr. 2007, doi: 10.1002/nme.1911.

[30] P. Di Re, "3D beam-column finite elements under tri-axial stress-strain states: non-uniform shear stress distribution and warping," PhD Thesis, Sapienza Università di Roma, 2016.

[31] D. Addessi, "Modelli di danno regolarizzati per materiali fragili," PhD Thesis, Sapienza Università di Roma, 2000.

[32] C. Gatta, D. Addessi, and F. Vestroni, "Static and dynamic nonlinear response of masonry walls," *Int J Solids Struct*, vol. 155, pp. 291–303, Dec. 2018, doi: 10.1016/j.ijsolstr.2018.07.028.

[33] P. Di Re, D. Addessi, and F. C. Filippou, "Mixed 3D Beam Element with Damage Plasticity for the Analysis of RC Members under Warping Torsion," *Journal of Structural Engineering*, vol. 144, no. 6, Jun. 2018, doi: 10.1061/(ASCE)ST.1943-541X.0002039.

[34] S. A. Neild, M. S. Williams, and P. D. McFadden, "Non-linear behaviour of reinforced concrete beams under low-amplitude cyclic and vibration loads," *Eng Struct*, vol. 24, no. 6, pp. 707–718, Jun. 2002, doi: 10.1016/S0141-0296(01)00134-1.

[35] N. Pešić, S. Živanović, J. Dennis, and J. Hargreaves, "Experimental and finite element dynamic analysis of incrementally loaded reinforced concrete

structures," *Eng Struct*, vol. 103, pp. 15–27, Nov. 2015, doi: 10.1016/j.engstruct.2015.07.037.

[36] A. Pranno, F. Greco, P. Lonetti, R. Luciano, and U. De Maio, "An improved fracture approach to investigate the degradation of vibration characteristics for reinforced concrete beams under progressive damage," *Int J Fatigue*, vol. 163, p. 107032, Oct. 2022, doi: 10.1016/j.ijfatigue.2022.107032.

[37] B. Pantò, D. Rapicavoli, S. Caddemi, and I. Caliò, "A smart displacement based (SDB) beam element with distributed plasticity," *Appl Math Model*, vol. 44, pp. 336–356, Apr. 2017, doi: 10.1016/j.apm.2017.01.018.

[38] B. Pantò, D. Rapicavoli, S. Caddemi, and I. Caliò, "A Fibre Smart Displacement Based (FSDB) beam element for the nonlinear analysis of reinforced concrete members," *Int J Non Linear Mech*, vol. 117, p. 103222, Dec. 2019, doi: 10.1016/j.ijnonlinmec.2019.07.007.

[39] D. Tarquini, J. P. Almeida, and K. Beyer, "Axially equilibrated displacement-based beam element for simulating the cyclic inelastic behaviour of RC members," *Earthq Eng Struct Dyn*, vol. 46, no. 9, pp. 1471–1492, Jul. 2017, doi: 10.1002/eqe.2865.

[40] F. F. Taucer, E. Spacone, and F. C. Filippou, "A Fiber Beam-Column Element for Seismic Response Analysis of Reinforced Concrete Structures," *Report No Ucb/Eerc-91/17, Earthquake Engineering Research Center*, 1991.

[41] E. Spacone, F. C. Filippou, and F. F. Taucer, "Fibre beam-column model for non-linear analysis of R/C frames: Part I. Formulation," *Earthq Eng Struct Dyn*, vol. 25, no. 7, pp. 711–725, 1996, doi: 10.1002/(SICI)1096-9845(199607)25:7<711::AID-EQE576>3.0.CO;2-9.

[42] E. Spacone, V. Ciampi, and F. C. Filippou, "Mixed formulation of nonlinear beam finite element," *Comput Struct*, vol. 58, no. 1, pp. 71–83, 1996, doi: 10.1016/0045-7949(95)00103-N.

[43] M. Petrangeli and V. Ciampi, "Equilibrium based iterative solutions for the non-linear beam problem," *Int J Numer Methods Eng*, vol. 40, no. 3, pp. 423–437, 1997, doi: 10.1002/(SICI)1097-0207(19970215)40:3<423::AID-NME72>3.0.CO;2-H.

[44] B. N. Alemdar and D. W. White, "Displacement, Flexibility, and Mixed Beam–Column Finite Element Formulations for Distributed Plasticity Analysis," *Journal of Structural Engineering*, vol. 131, no. 12, pp. 1811–1819, 2005, doi: 10.1061/(asce)0733-9445(2005)131:12(1811).

[45] S. M. Kostic and F. C. Filippou, "Section Discretization of Fiber Beam-Column Elements for Cyclic Inelastic Response," *Journal of Structural Engineering*, vol. 138, no. 5, pp. 592–601, 2012, doi: 10.1061/(asce)st.1943-541x.0000501.

[46] A. Neuenhofer and F. C. Filippou, "Evaluation of Nonlinear Frame Finite-Element Models," *Journal of Structural Engineering*, vol. 123, no. 7, pp. 958–966, 1997, doi: 10.1061/(asce)0733-9445(1997)123:7(958).

[47] A. Neuenhofer and F. C. Filippou, "Geometrically Nonlinear Flexibility-Based Frame Finite Element," *Journal of Structural Engineering*, vol. 124, no. 6, pp. 704–711, 1998, doi: 10.1061/(asce)0733-9445(1998)124:6(704).

[48] R. L. Taylor, F. C. Filippou, A. Saritas, and F. Auricchio, "A mixed finite element method for beam and frame problems," *Comput Mech*, vol. 31, no. 1–2, pp. 192–203, 2003, doi: 10.1007/s00466-003-0410-y.

[49] A. Ayoub and F. C. Filippou, "Mixed Formulation of Bond-Slip Problems under Cyclic Loads," *Journal of Structural Engineering*, vol. 125, no. 6, pp. 661–671, 1999, doi: 10.1061/(asce)0733-9445(1999)125:6(661).

[50] A. Ayoub and F. C. Filippou, "Finite-Element Model for Pretensioned Prestressed Concrete Girders," *Journal of Structural Engineering*, vol. 136, no. 4, pp. 401–409, 2010, doi: 10.1061/(asce)st.1943-541x.0000132.

[51] Wenjun Zhu, "Effect of corrosion on the mechanical properties of the corroded reinforcement and the residual structural performance of the corroded beams.," INSA de Toulouse, 2014.

[52] S. B. Singh, P. Munjal, and N. Thammishetti, "Role of water/cement ratio on strength development of cement mortar," *Journal of Building Engineering*, vol. 4, pp. 94–100, Dec. 2015, doi: 10.1016/j.jobe.2015.09.003.

[53] J. C. Simo and T. J. R. Hughes, *Interdisciplinary Applied Mathematics, Volume 7. Computational Inelasticity*, vol. 7, no. 3. 2006.

[54] D. C. Drucker and W. Prager, "Soil mechanics and plastic analysis or limit design," *Q Appl Math*, vol. 10, no. 2, 1952, doi: 10.1090/qam/48291.

[55] M. Rezaiee-Pajand, M. Sharifian, and M. Sharifian, "Accurate and approximate integrations of Drucker-Prager plasticity with linear isotropic and kinematic hardening," *European Journal of Mechanics, A/Solids*, vol. 30, no. 3, pp. 345–361, 2011, doi: 10.1016/j.euromechsol.2010.12.001.

[56] E. Öztekin, S. Pul, and M. Hüsem, "Experimental determination of Drucker-Prager yield criterion parameters for normal and high strength concretes under triaxial compression," *Constr Build Mater*, vol. 112, pp. 725–732, Jun. 2016, doi: 10.1016/j.conbuildmat.2016.02.127.

[57] R. Faria, J. Oliver, and M. Cervera, "Modeling Material Failure in Concrete Structures under Cyclic Actions," *Journal of Structural Engineering*, vol. 130, no. 12, pp. 1921–1930, 2004, doi: 10.1061/(asce)0733-9445(2004)130:12(1997).

[58] J. Mazars, F. Hamon, and S. Grange, "A new 3D damage model for concrete under monotonic, cyclic and dynamic loadings," *Materials and Structures/Materiaux et Constructions*, vol. 48, no. 11, pp. 3779–3793, 2015, doi: 10.1617/s11527-014-0439-8.

[59] J. Mazars, "A description of micro- and macroscale damage of concrete structures," *Eng Fract Mech*, vol. 25, no. 5–6, pp. 729–737, 1986, doi: 10.1016/0013-7944(86)90036-6.

[60] J. Lee and G. L. Fenves, "Plastic-Damage Model for Cyclic Loading of Concrete Structures," *J Eng Mech*, vol. 124, no. 8, pp. 892–900, 1998, doi: 10.1061/(asce)0733-9399(1998)124:8(892).

[61] D. Addessi, S. Marfia, and E. Sacco, "A plastic nonlocal damage model," *Comput Methods Appl Mech Eng*, vol. 191, no. 13–14, pp. 1291–1310, Jan. 2002, doi: 10.1016/S0045-7825(01)00325-5.

[62] F. Légeron, P. Paultre, and J. Mazars, "Damage Mechanics Modeling of Nonlinear Seismic Behavior of Concrete Structures," *Journal of Structural Engineering*, vol. 131, no. 6, pp. 946–955, Jun. 2005, doi: 10.1061/(ASCE)0733-9445(2005)131:6(946).

[63] O. Nouailletas, C. La Borderie, C. Perlot, P. Rivard, and G. Ballivy, "Experimental Study of Crack Closure on Heterogeneous Quasi-Brittle Material," *J Eng Mech*, vol. 141, no. 11, Nov. 2015, doi: 10.1061/(ASCE)EM.1943-7889.0000928.

[64] S. Ramtani, Y. Berthaud, and J. Mazars, "Orthotropic behavior of concrete with directional aspects: modelling and experiments," *Nuclear Engineering and Design*, vol. 133, no. 1, pp. 97–111, 1992, doi: 10.1016/0029-5493(92)90094-C.

[65] J. F. Sima, P. Roca, and C. Molins, "Cyclic constitutive model for concrete," *Eng Struct*, vol. 30, no. 3, pp. 695–706, 2008, doi: 10.1016/j.engstruct.2007.05.005.

[66] H. W. Reinhardt, "Fracture Mechanics of an Elastic Softening Material like Concrete," *Heron*, vol. 29, no. 2, 1984.

[67] Z. P. Bažant, T. B. Belytschko, and T. Chang, "Continuum Theory for Strain-Softening," *J Eng Mech*, vol. 110, no. 12, pp. 1666–1692, Dec. 1984, doi: 10.1061/(ASCE)0733-9399(1984)110:12(1666).

[68] Z. P. Bažant, J. Pan, and G. Pijaudier-Cabot, "Softening in Reinforced Concrete Beams and Frames," *Journal of Structural Engineering*, vol. 113, no. 12, pp. 2333–2347, Dec. 1987, doi: 10.1061/(ASCE)0733-9445(1987)113:12(2333).

[69] M. H. Scott and G. L. Fenves, "Plastic Hinge Integration Methods for Force-Based Beam–Column Elements," *Journal of Structural Engineering*, vol. 132, no. 2, pp. 244–252, Feb. 2006, doi: 10.1061/(ASCE)0733-9445(2006)132:2(244).

[70] Tanaka Hitoshi, "Effect of lateral confining reinforcement on the ductile behaviour of reinforced concrete columns," PhD Thesis, University of Canterbury, 1990. doi: 10.26021/3137.

[71] Z. P. Bažant and F. Lin, "Nonlocal Smeared Cracking Model for Concrete Fracture," *Journal of Structural Engineering*, vol. 114, no. 11, pp. 2493–2510, Nov. 1988, doi: 10.1061/(ASCE)0733-9445(1988)114:11(2493).

[72] Z. P. Bažant and B. H. Oh, "Crack band theory for fracture of concrete," *Matériaux et Constructions*, vol. 16, no. 3, pp. 155–177, May 1983, doi: 10.1007/BF02486267.

[73] Z. P. Bažant and M. Jirásek, "Nonlocal Integral Formulations of Plasticity and Damage: Survey of Progress," *J Eng Mech*, vol. 128, no. 11, pp. 1119–1149, Nov. 2002, doi: 10.1061/(ASCE)0733-9399(2002)128:11(1119).

[74] G. Pijaudier-Cabot and Z. P. Bažant, "Nonlocal Damage Theory," *J Eng Mech*, vol. 113, no. 10, pp. 1512–1533, Oct. 1987, doi: 10.1061/(ASCE)0733-9399(1987)113:10(1512).

[75] R. H. J. Peerlings, M. G. D. Geers, R. de Borst, and W. A. M. Brekelmans, "A critical comparison of nonlocal and gradient-enhanced softening continua," *Int J Solids Struct*, vol. 38, no. 44–45, pp. 7723–7746, Nov. 2001, doi: 10.1016/S0020-7683(01)00087-7.

[76] M. Kenawy, S. Kunnath, S. Kolwankar, and A. Kanvinde, "Fiber-Based Nonlocal Formulation for Simulating Softening in Reinforced Concrete Beam-Columns," *Journal of Structural Engineering*, vol. 144, no. 12, Dec. 2018, doi: 10.1061/(ASCE)ST.1943-541X.0002218.

[77] J. Coleman and E. Spacone, "Localization Issues in Force-Based Frame Elements," *Journal of Structural Engineering*, vol. 127, no. 11, pp. 1257–1265, Nov. 2001, doi: 10.1061/(ASCE)0733-9445(2001)127:11(1257).

[78] M. H. Scott and K. L. Ryan, "Moment-Rotation Behavior of Force-Based Plastic Hinge Elements," *Earthquake Spectra*, vol. 29, no. 2, pp. 597–607, May 2013, doi: 10.1193/1.4000136.

[79] M. H. Scott and O. M. Hamutçuoğlu, "Numerically consistent regularization of force-based frame elements," *Int J Numer Methods Eng*, vol. 76, no. 10, pp. 1612–1631, Dec. 2008, doi: 10.1002/nme.2386.

[80] V. Ciampi and L. Carlesimo, "A nonlinear beam element for seismic analysis of structures," in *Proceedings of the Eighth European Conferenceon Earthquake Engineering*, Lisbon, 1986.

[81] L. Parente, D. Addessi, and E. Spacone, "A fiber beam element based on plastic and damage models for prestressed concrete structures," *Eng Struct*, vol. 292, p. 116501, Oct. 2023, doi: 10.1016/j.engstruct.2023.116501.

[82] F. McKenna, G. Fenves, and M. Scott, "Open system for earthquake engineering simulation," *Pacific Earthquake Engineering Research Center*, 2000.

[83] F. McKenna and G. L. Fenves, "An Object-Oriented Software Design for Parallel Structural Analysis," in *Advanced Technology in Structural Engineering*, Reston, VA: American Society of Civil Engineers, Apr. 2000, pp. 1–8. doi: 10.1061/40492(2000)30.

[84] F. McKenna, M. H. Scott, and G. L. Fenves, "Nonlinear Finite-Element Analysis Software Architecture Using Object Composition," *Journal of Computing in Civil Engineering*, vol. 24, no. 1, pp. 95–107, Jan. 2010, doi: 10.1061/(ASCE)CP.1943-5487.0000002.

[85] M. H. Scott, G. L. Fenves, F. McKenna, and F. C. Filippou, "Software Patterns for Nonlinear Beam-Column Models," *Journal of Structural Engineering*, vol. 134, no. 4, pp. 562–571, Apr. 2008, doi: 10.1061/(ASCE)0733-9445(2008)134:4(562).

[86] F. McKenna, "Object-oriented finite element programming: Frameworks for analysis, algorithms, and parallel computing," PhD Thesis, University of California, California, 1997.

[87] F. McKenna, "OpenSees: A framework for earthquake engineering simulation," *Comput Sci Eng*, vol. 13, no. 4, pp. 58–66, 2011, doi: 10.1109/MCSE.2011.66.

[88] G. L. Fenves, "Object-oriented programming for engineering software development," *Eng Comput*, vol. 6, no. 1, pp. 1–15, 1990, doi: 10.1007/BF01200200.

[89] S. Mazzoni, F. McKenna, H. M. Scott, and L. G. Fenves, "OpenSees Command Language Manual," *Pacific Earthquake Engineering Research (PEER) Center*, vol. 246 (1), 2006.

[90] ASDEA SRL, "The Scientific ToolKit for OpenSees, STKO, a GUI for OpenSees."

[91] Petracca Massimo, Candeloro F, and Camata Guido, *STKO User Manual*. ASDEA Software: Pescara, Italy, 2017.

[92] F. Leonhardt, *C.a. & C.a.p.: calcolo di progetto & tecniche costruttive*, vol. 6. Edizioni di scienza e tecnica, 1979.

[93] C. Menn, *Prestressed Concrete Bridges*. Birkhäuser Basel, 1990. doi: 10.1007/978-3-0348-9131-8.

[94] N. Hewson, *Prestressed Concrete Bridges*. ICE Publishing, 2012. doi: 10.1680/pcb.41134.

[95] W. Lin and T. Yoda, "Reinforced and Prestressed Concrete Bridges," in *Bridge Engineering*, Elsevier, 2017, pp. 97–110. doi: 10.1016/B978-0-12-804432-2.00006-2.

[96] MIDAS Information Technology Co., "Precast Concrete Bridge," https://resource.midasuser.com/en/solution/precast-concrete-bridges.

[97] B. O. Aalami, "Structural Modeling of Posttensioned Members," *Journal of Structural Engineering*, vol. 126, no. 2, pp. 157–162, Feb. 2000, doi: 10.1061/(ASCE)0733-9445(2000)126:2(157).

[98] P. Roca and A. R. Marí, "Numerical treatment of prestressing tendons in the nonlinear analysis of prestressed concrete structures," *Comput Struct*, vol. 46, no. 5, pp. 905–916, Mar. 1993, doi: 10.1016/0045-7949(93)90152-4.

[99] P. J. S. Cruz, A. R. Marí, and P. Roca, "Nonlinear Time-Dependent Analysis of Segmentally Constructed Structures," *Journal of Structural Engineering*, vol. 124, no. 3, pp. 278–287, Mar. 1998, doi: 10.1061/(ASCE)0733-9445(1998)124:3(278).

[100] H. A. Doty, "A Module for Finite Element Analysis of Prestressed Concrete Bridges," M.S. Thesis, University of Colorado, 2001.

[101] W. Choi, "Flexural behaviour of prestressed girder with high-strength concrete," PhD Thesis, North Carolina State University, 2006.

[102] MIDAS GEN, "Analysis manual for MIDAS/GEN," Seoul, Korea, 2012.

[103] MIDAS Information Technology Co., "MIDAS GEN software."

[104] MIDAS Information Technology Co., "MIDAS FEA NX software."

[105] W. Choi, S. Rizkalla, P. Zia, and A. Mirmiran, "Behavior and design of high-strength prestressed concrete girders," *PCI Journal*, vol. 53, no. 5, pp. 54–69, Sep. 2008, doi: 10.15554/pcij.09012008.54.69.

[106] A. de la Fuente, A. Aguado, C. Molins, and J. Armengou, "Numerical model for the analysis up to failure of precast concrete sections," *Comput Struct*, vol. 106–107, pp. 105–114, Sep. 2012, doi: 10.1016/j.compstruc.2012.04.007.

[107] M. Crognale, M. De Iuliis, C. Rinaldi, and V. Gattulli, "Damage detection with image processing: a comparative study," *Earthquake Engineering and Engineering Vibration*, vol. 22, no. 2, pp. 333–345, Apr. 2023, doi: 10.1007/s11803-023-2172-1.

[108] F. N. Catbas and A. E. Aktan, "Condition and Damage Assessment: Issues and Some Promising Indices," *Journal of Structural Engineering*, vol. 128, no. 8, pp. 1026–1036, Aug. 2002, doi: 10.1061/(ASCE)0733-9445(2002)128:8(1026).

[109] S. U. Rehman, M. Usman, M. H. Y. Toor, and Q. A. Hussaini, "Advancing structural health monitoring: A vibration-based IoT approach for remote real-time systems," *Sens Actuators A Phys*, vol. 365, p. 114863, Jan. 2024, doi: 10.1016/j.sna.2023.114863.

[110] M. Gul and F. N. Catbas, "Structural health monitoring and damage assessment using a novel time series analysis methodology with sensor clustering," *J Sound Vib*, vol. 330, no. 6, pp. 1196–1210, Mar. 2011, doi: 10.1016/j.jsv.2010.09.024.

[111] O. S. Salawu, "Detection of structural damage through changes in frequency: a review," *Eng Struct*, vol. 19, no. 9, pp. 718–723, Sep. 1997, doi: 10.1016/S0141-0296(96)00149-6.

[112] S. Keßler *et al.*, *fib Bulletin 109. Existing concrete structures life management, testing and structural health monitoring*. fib. The International Federation for Structural Concrete, 2023. doi: 10.35789/fib.BULL.0109.

[113] M. Crognale, "Una procedura per l'identificazione del danno in strutture reticolari in acciaio," PhD Thesis, Sapienza Università di Roma, 2021.

[114] E. García-Macías *et al.*, "P3P: a software suite for autonomous SHM of bridge networks," *J Civ Struct Health Monit*, vol. 13, no. 8, pp. 1577–1594, Dec. 2023, doi: 10.1007/s13349-022-00653-6.

[115] B. Kostić and M. Gül, "Vibration-Based Damage Detection of Bridges under Varying Temperature Effects Using Time-Series Analysis and Artificial Neural Networks," *Journal of Bridge Engineering*, vol. 22, no. 10, Oct. 2017, doi: 10.1061/(ASCE)BE.1943-5592.0001085.

[116] M. N. Cerri and F. Vestroni, "Use of Frequency Change for Damage Identification in Reinforced Concrete Beams," *Journal of Vibration and Control*, vol. 9, no. 3–4, pp. 475–491, Mar. 2003, doi: 10.1177/107754603030787.

[117] D. Balageas, C. P. Fritzen, and A. Güemes, *Structural health monitoring*. ISTE, 2006.

[118] A. Rytter, "Vibration based inspection of civil engineering structures," PhD Thesis, Aalborg University, 1993.

[119] Y. J. Yan, L. Cheng, Z. Y. Wu, and L. H. Yam, "Development in vibration-based structural damage detection technique," *Mech Syst Signal Process*, vol. 21, no. 5, pp. 2198–2211, Jul. 2007, doi: 10.1016/j.ymssp.2006.10.002.

[120] A. D. Dimarogonas, "Vibration of cracked structures: A state of the art review," *Eng Fract Mech*, vol. 55, no. 5, pp. 831–857, Nov. 1996, doi: 10.1016/0013-7944(94)00175-8.

[121] M. Kato and S. Shimada, "Vibration of PC Bridge during Failure Process," *Journal of Structural Engineering*, vol. 112, no. 7, pp. 1692–1703, Jul. 1986, doi: 10.1061/(ASCE)0733-9445(1986)112:7(1692).

[122] P. Di Re, D. Addessi, and A. Paolone, "Mixed beam formulation with cross-section warping for dynamic analysis of thin-walled structures," *Thin-Walled Structures*, vol. 141, pp. 554–575, Aug. 2019, doi: 10.1016/j.tws.2019.04.014.

[123] Y. Shen, X. Chen, W. Jiang, and X. Luo, "Spatial force-based non-prismatic beam element for static and dynamic analyses of circular flexure hinges in compliant mechanisms," *Precis Eng*, vol. 38, no. 2, pp. 311–320, Apr. 2014, doi: 10.1016/j.precisioneng.2013.11.001.

[124] R. M. de Souza, F. C. Filippou, A. M. B. Pereira, and G. Y. Aranha Jr, "Force formulation of a non-prismatic Timoshenko beam finite element for dynamic analysis of frames," in *XXIV Iberian Latin-American Congress in Computational Methods in Engineering.*, Ouro Preto, Brazil, 2003, pp. 789–813.

[125] C. Molins, P. Roca, and A. H. Barbat, "Flexibility-based linear dynamic analysis of complex structures with curved-3D members," *Earthq Eng Struct Dyn*, vol. 27, no. 7, pp. 731–747, 1998, doi: 10.1002/(SICI)1096-9845(199807)27:7<731::AID-EQE754>3.0.CO;2-1.

[126] K. Worden and G. Manson, "The application of machine learning to structural health monitoring," *Philosophical Transactions of the Royal Society A: Mathematical, Physical and Engineering Sciences*, vol. 365, no. 1851, pp. 515–537, 2007, doi: 10.1098/rsta.2006.1938.

[127] C. R. Farrar and K. Worden, *Structural Health Monitoring: A Machine Learning Perspective*. John Wiley & Sons, Ltd, 2012. doi: 10.1002/9781118443118.

[128] E. Figueiredo, G. Park, C. R. Farrar, K. Worden, and J. Figueiras, "Machine learning algorithms for damage detection under operational and environmental variability," *Struct Health Monit*, vol. 10, no. 6, pp. 559–572, 2011, doi: 10.1177/1475921710388971.

[129] J. Shu, Z. Zhang, I. Gonzalez, and R. Karoumi, "The application of a damage detection method using Artificial Neural Network and train-induced vibrations on a simplified railway bridge model," *Eng Struct*, vol. 52, pp. 408–421, Jul. 2013, doi: 10.1016/j.engstruct.2013.02.031.

[130] J. P. de Oliveira Dias Prudente dos Santos, C. Crémona, A. P. C. da Silveira, and L. C. de Oliveira Martins, "Real-time damage detection based on pattern recognition," *Structural Concrete*, vol. 17, no. 3, pp. 338–354, 2016, doi: 10.1002/suco.201500092.

[131] H. Yu and B. M. Wilamowski, "Levenberg–Marquardt Training," in *Intelligent Systems*, CRC Press, 2018, pp. 12–1. doi: 10.1201/9781315218427-12.

[132] A. C. Neves, I. González, J. Leander, and R. Karoumi, "Structural health monitoring of bridges: a model-free ANN-based approach to damage

detection," *J Civ Struct Health Monit*, vol. 7, no. 5, pp. 689–702, Nov. 2017, doi: 10.1007/s13349-017-0252-5.

[133] M. Crognale, M. De Iuliis, C. Rinaldi, and V. Gattulli, "Damage detection with image processing: a comparative study," *Earthquake Engineering and Engineering Vibration*, vol. 22, no. 2, pp. 333–345, Apr. 2023, doi: 10.1007/s11803-023-2172-1.

[134] J. Bauer, N. Sünderhauf, and P. Protzel, "Comparing several implementations of two recently published feature detectors," *IFAC Proceedings Volumes*, vol. 40, no. 15, pp. 143–148, 2007, doi: 10.3182/20070903-3-fr-2921.00027.

[135] G. W. Housner *et al.*, "Structural Control: Past, Present, and Future," *J Eng Mech*, vol. 123, no. 9, 1997, doi: 10.1061/(asce)0733-9399(1997)123:9(897).

[136] Y.-J. Cha, W. Choi, and O. Büyüköztürk, "Deep Learning-Based Crack Damage Detection Using Convolutional Neural Networks," *Computer-Aided Civil and Infrastructure Engineering*, vol. 32, no. 5, pp. 361–378, May 2017, doi: 10.1111/mice.12263.

[137] W. R. L. da Silva and D. S. de Lucena, "Concrete Cracks Detection Based on Deep Learning Image Classification," *Proceedings*, vol. 2, no. 8, 2018, doi: 10.3390/icem18-05387.

[138] T. Yamane and P. J. Chun, "Crack detection from a concrete surface image based on semantic segmentation using deep learning," *Journal of Advanced Concrete Technology*, vol. 18, no. 9, pp. 493–504, 2020, doi: 10.3151/jact.18.493.

[139] S. Grosman, Q. Fang, L. Macorini, and B. A. Izzuddin, "Computational strategy for the design of monitoring for masonry arch bridges using DIC procedures," in *Life-Cycle of Structures and Infrastructure Systems - Proceedings of the 8th International Symposium on Life-Cycle Civil Engineering, IALCCE 2023*, London: CRC Press, 2023, pp. 1530–1537. doi: 10.1201/9781003323020-188.

[140] N. Bagge, C. Popescu, and L. Elfgren, "Failure tests on concrete bridges: Have we learnt the lessons?," *Structure and Infrastructure Engineering*, vol. 14, no. 3, pp. 292–319, Mar. 2018, doi: 10.1080/15732479.2017.1350985.

[141] D. Tonelli, F. Rossi, F. Brighenti, A. Verzobio, A. Bonelli, and D. Zonta, "Prestressed concrete bridge tested to failure: the Alveo Vecchio viaduct case study," *J Civ Struct Health Monit*, vol. 13, no. 4–5, pp. 873–899, Jun. 2023, doi: 10.1007/s13349-022-00633-w.

[142] D. Tonelli, M. Luchetta, F. Rossi, P. Migliorino, and D. Zonta, "Structural Health Monitoring Based on Acoustic Emissions: Validation on a Prestressed Concrete Bridge Tested to Failure," *Sensors*, vol. 20, no. 24, p. 7272, Dec. 2020, doi: 10.3390/s20247272.